Study of superconducting fault current limiters in power systems

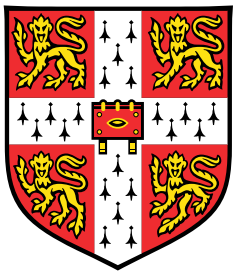

Qihuan Dong

Department of Engineering
University of Cambridge

This dissertation is submitted for the degree of
Doctor of Philosophy

Newnham College

January 2019

I would like to dedicate this thesis to my loving parents ...

Declaration

I hereby declare that except where specific reference is made to the work of others, the contents of this dissertation are original and have not been submitted in whole or in part for consideration for any other degree or qualification in this, or any other university. This dissertation is my own work and contains nothing which is the outcome of work done in collaboration with others, except as specified in the text and Acknowledgements. This dissertation contains fewer than 65,000 words including appendices, bibliography, footnotes, tables and equations and has fewer than 150 figures.

Qihuan Dong
January 2019

Acknowledgements

The four-year PhD study at the University of Cambridge has been an arduous but fruitful journey. It would have been impossible for me to accomplish the work without the numerous help I received from many people and for that I will always bear them in mind. I want to take this opportunity to express my deepest gratitude to all of you here, even if you are not personally mentioned.

First and foremost, I gratefully acknowledge my supervisor Dr. Timothy A. Coombs for admitting me to this world-class research group and leading me to the fascinating world of applied superconductivity. Dr. Tim Coombs and his wife not only help me with academic research but also support me in every aspect of life.

I would like to extend my sincerest thanks to my advisor Prof. Tim Wilkinson for his encouragement and patience in advising me. His scientific knowledge and life experiences are important in my journey.

I am especially thankful to Prof. Mathias Noe and Dr. Wescley Tiago Batista de Souse who supervised me during my exchange period at Karlsruhe Institute of Technology, Germany. They were extremely patient, teaching me a lot regarding Matlab, LaTex, Originlab, Inkscape and Thermal-Electrical Analog Methods for modelling Superconducting Fault Current Limiters.

I would also like to thank Prof. Zhiyong Hong and the staff of Shanghai Superconductors Ltd. for enabling me to observe their daily operations. I am also very grateful to Mr Jiamin Zhu for his generous gift of time and help in conducting experiments on YBCO tapes.

I greatly appreciate the support received from Dr. Sohrab Mirsaeidi, Dr. Teng Feng, Haozong Wang, Binshu Chen, Tianqi Jia and Beier Zhu at Tsinghua University. Their expertise in power systems was most helpful as I researched SFCLs and Commutation Failure in Chapter 6.

My sincere gratitude goes to Prof. Bin Li and Dr. Yizhe Ou at Tianjin University for their guidance in PSCAD programming during the first year of my PhD. Their thoughtful discussions and collaboration on mathematical analysis of Incremental Power Frequency Relay are essential to the work in Chapter 7.

I would like to thank all the staff at Newnham College, especially my tutor Dr. Kate Fleet, for their full assistance, and most of my colleagues at the University of Cambridge for their friendship. I feel extremely lucky to have gained so many friends and mentors at this astoundingly extraordinary campus.

Last but not least, heartfelt thankfulness goes to my dearest parents. Thank you for making me who I am today.

Abstract

Power systems have increased both in scale and complexity as a result of rapid growth in the demand for power.

The most common causes of failures in power systems are short-circuit faults. Short-circuit currents can grow thousands of times larger than normal system operating currents, i.e., within milliseconds. This places enormous thermal and mechanical stress on existing transmission infrastructure and may even cause blackouts.

With the expansion and modernisation of power systems, fault current levels have also increased. The contributing factors include: the installation of new transmission facilities, transformers and generators, the upgrading of existing generators, and the integration of renewable energy sources. Conventional protection devices are unable to handle high fault current levels. Therefore a novel approach is required to limit the fault current level and to improve the resilience and reliability of power systems.

The superconducting fault current limiter (SFCL) is one of the most significant and useful applications for high-temperature superconductors. It has many unique features which limit fault currents in power systems. Using the electrical characteristics of superconductors for current limitation is not a new idea. SFCL was first proposed in 1966 and has since been further developed. However, there is still much research needed on the SFCL device itself and its coordination with the traditional power grid.

This thesis provides comprehensive and in-depth research on SFCLs and there are four new findings in this work.

Firstly, we use four-probe methods to identify the best hierarchical structure for the 2G HTS YBCO tapes used for SFCL device in order to improve the fault current limiting effect. Three commercially available YBCO tapes are compared and the characteristics of one of the tapes have never been previously published. The work forms the foundation for the proper selection of YBCO tapes for SFCL devices, to support varying development and operational engineering requirements.

Secondly, the study of SFCL integrated with a real AC power distribution network in Germany is accomplished using Finite Element Modeling (FEM) on Matlab Simulink. It provides the complete research procedures of SFCL integrated with a grid network and the

underlying impact of this integration is thoroughly analyzed. The real data and sophisticated models employed here assure the simulation results are reliable and instructive for practical operation.

Thirdly, we use PSCAD to simulate the SFCL installed in a Direct Current (DC) grid, and the SFCL has proved to be effective in preventing commutation failure in DC grid. Prior research done on the influence of SFCL on commutation failure has shown that it can mitigate commutation failure to some extent, but here we demonstrate R-SFCLs with correct resistance values can entirely solve the problem of commutation failures. It also shows that the SFCL has unsurpassed advantages compared to traditional mitigation methods.

Fourthly, the coordination of SFCL with the Incremental Power Frequency Relay (IPFR) are studied by using PSCAD. The influence of SFCLs on grid protection is a critical area for SFCL engineering applications. The work examines the influences of R-SFCLs on IPFR of transmission lines, and proposes corresponding compensation methods. The theoretical analysis is innovative, and valuable for engineering applications.

Table of contents

List of figures

List of tables

Chapter 1

Introduction

High-T_c superconductors are superior to low-T_c superconductors in terms of critical temperature and critical current density. Second Generation (2G) coated conductor YBCO tapes are especially engineering-favourable for power applications, because of their ideal engineering critical current density, mechanical strength and thermal stability.

Among the biggest challenges in the development of modern power systems are rapidly increasing fault current levels. These faults are hazardous to power system equipment, harmful in the safe operation of the overall system, and extremely dangerous to humans. Superconducting Fault Current Limiters (SFCLs) are promising devices to limit fault current levels, because they present negligible impedance during normal operation and considerable impedance when faults occur. Amongst all types of SFCLs, resistive SFCLs (R-SFCLs) are the most popular due to their simple and compact structure.

R-SFCLs are promising devices for power systems, but much research and development is required before they are ready for practical use. This includes the deeper study of R-SFCLs themselves, and their influence on power systems. Our research effort investigates the influence of R-SFCLs developed with 2G coated conductors on power systems. First, 2G coated conductors are characterized under pulsed over-current conditions, to obtain an indicative and conclusive result for R-SFCLs design. Next, we investigate the influence of R-SFCLs on Alternating Current (AC) power systems, on Incremental Power-Frequency Relays (IPFR), and on Direct Current (DC) power systems. The structure of the thesis is as follows:

- Chapter 2 presents a brief introduction to superconductivity and its basic theories. It begins with the definition of superconductivity, i.e. zero-resistivity and perfect diamagnetism. It then presents the methods to classify superconductors: to classify them as high-Tc super-conductors or low-Tc superconductors according to their critical

temperature; or to classify them as type-I superconductors or type-II superconductors according to their reaction to external magnetic fields. Microscopic electro-magnetic properties of type-II superconductors such as vortices, flux pinning, and critical current density were then introduced. Lastly, macroscopic characteristics of type-II superconductors, such as the critical state models, E-J power law, and AC loss are introduced.

- Chapter 3 presents a brief review of SFCLs. It begins with introducing tremendous high fault current problems in modern power systems, and proposes SFCLs as a preferred solution. Then it give a comprehensive review on the existing SFCLs; including R-SFCLs, saturated iron core SFCLs, inductive SFCLs, bridge type SFCLs. Working principles, advantages and disadvantages, and existing projects of these devices are introduced.

- Chapter 4 presents the experimental investigation of 2G YBCO tapes for constructing R-SFCLs. First, pulsed over-current experiment on different types YBCO tapes are conducted. The experimental data results, indicate that three key parameters are essential for the performance of different tapes as R-SFCLs, including: critical current of the superconductor, room temperature resistance of the tapes, and the mass of the tapes. Using these preliminary results, influence of these parameters on the performance of limiting pulsed over-current is comprehensively analyzed.

- In Chapter 5, the study of SFCL integrated with a real AC power distribution network in Germany is studied using Finite Element Modeling (FEM) on Matlab Simulink. This chapter provides the complete research procedures of SFCL integrated with a grid network. These procedures include: locating the best place for SFCL installation, designing the structure of an SFCL, building a practical model of an SFCL, and comparing the system with and without the SFCL. Simulation results show that the R-SFCL is useful for significantly decreasing the fault current level, mitigating voltage sag, and eliminating high-frequency voltage oscillation for the AC power distribution system.

- Chapter 6 attempts to use R-SFCL to solve the problem of commutation failure in direct current (DC) systems. Prior research done on the influence of SFCL on commutation failure has shown that it can mitigate commutation failure to some extent, but the performance of R-SFCLs with different resistance values under different fault resistance values and fault initiation times in a DC system has not previously been investigated. Simulation results show that the SFCL has unsurpassed advantages for suppressing commutation failure compared to traditional mitigation methods.

- The influence of SFCLs on grid protection is a critical area for SFCL engineering applications. Chapter 7 examines the influences of R-SFCLs on Incremental Power Frequency Relay of transmission lines, and proposes corresponding compensation methods. One of the proposed compensation methods produces very desirable results: the protection distance of IPFRs nearly reaches their setting values for all four types of short-circuited fault.
- Chapter 8 summarizes the thesis research, and proposes related study areas for further research.

Chapter 2

Introduction to superconductivity

Superconductivity is a remarkable characteristic of a combination of electric and magnetic properties which appear in certain materials when they are cooled to extremely low temperatures [16].

2.1 Fundamental physics of superconductivity

2.1.1 Perfect conductivity

In 1911, Dutch physicist Heike Kamerlingh Onnes first discovered the phenomenon of superconductivity at the University of Leiden when he measured the electrical resistance of pure mercury. He observed that the resistance decreased dramatically when temperature of the mercury sample was reduced to around 4.2 K. Below this temperature, resistance approached zero, as shown in Fig. 2.1. Professor Onnes recognised that mercury passed into a new state below 4 K, and its electrical properties in this state were quite different from that those exhibited at normal temperatures.

This new state is called the “superconducting state”, and a material which shows superconductivity if cooled is called superconductor. The temperature below which superconductors transit into the superconducting state is called critical temperature T_c.

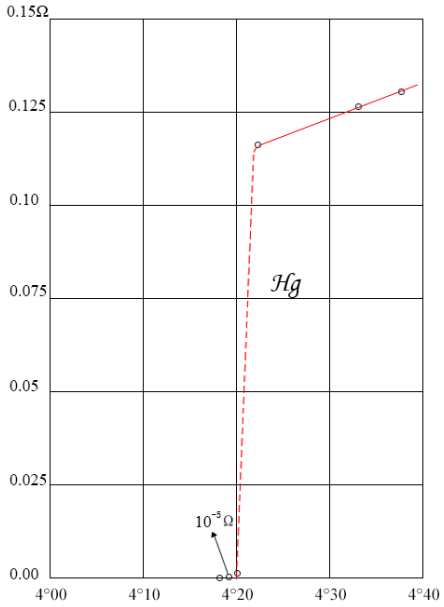

Fig. 2.1 The resistance (Ohms) versus temperature (Kelvin) curve of mercury measured by H. K. Onnes in 1911 shows the superconducting transition at 4.2 K (adapted from [1]).

2.1.2 Perfect diamagnetism

Later in 1933, German physicists Walther Meissner and Robert Ochsenfeld observed the complete expulsion of magnetic flux from superconducting tin and lead samples in an external field. This reveals that superconductors are perfectly diamagnets. The difference between an ideal conductor and a superconductor is shown in Fig. 2.2.

Under field cooling condition, the magnetic field is applied before the material is cooled down to become either superconducting or perfectly conductive. For a perfect conductor, during this transition, the magnetic flux inside is conservative. This means the flux that links the material remains unchanged,

$$\frac{d\phi}{dt} = 0 \tag{2.1.1}$$

as illustrated by Fig. 2.2(a). In contrast, for a superconductor, the magnetic field inside is always zero,

$$B = \mu_0(H+M) = 0 \tag{2.1.2}$$

This indicates that during the phase transition from normal to superconducting, all the applied flux is expelled from the superconductor, as shown in Fig. 2.2(b). When transitioning to the superconducting state, the material becomes perfectly diamagnetic, and the magnetic susceptibility χ equals -1. (This is only true when the applied field is low, which will be discussed in detail later.)

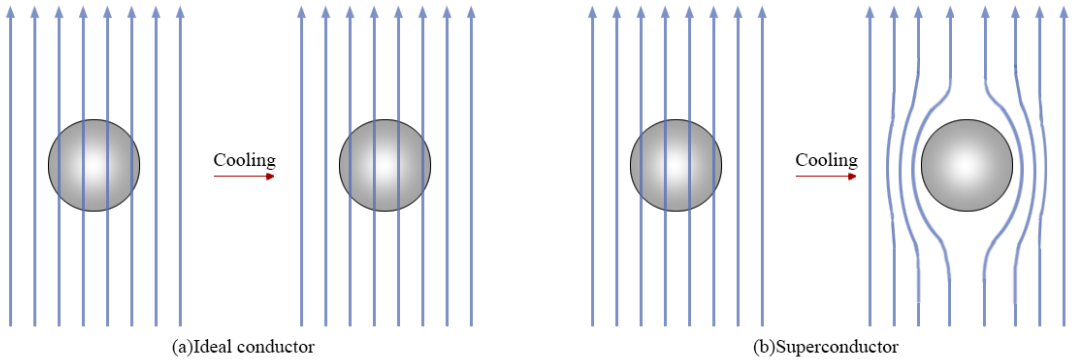

Fig. 2.2 Illustration of the difference between a perfect conductor and a superconductor under field cooling conditions.

Under zero field cooling conditions (i.e. the material is cooled down before the magnetic field is applied) a superconductor and an ideal conductor react to the applied field in the same way: both of them expel all the applied flux.

In contrast to perfect conductors, a defining characteristic of superconductors is that they exhibit both attributes: zero resistivity and perfect diamagnetism.

2.2 Classification of superconductors

As illustrated in Fig. 2.3 [2], since Professor Onnes first discovered mercury's superconducting critical temperature in 1911, many superconductors have been found. They can be classified as low-T_c superconductors and high-T_c superconductors according to their critical temperature, and can be classified as type-I superconductors and type-II superconductors according to their magnetization characteristics.

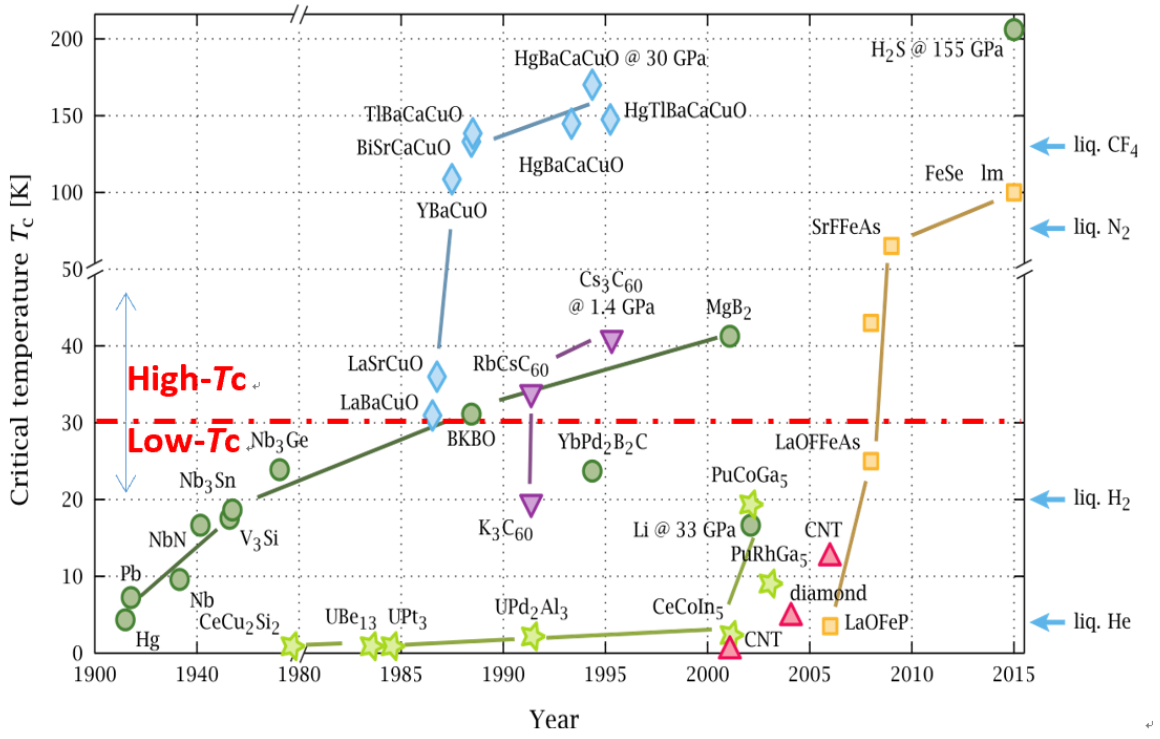

Fig. 2.3 Time-line of superconducting materials (adapted from [2]).

2.2.1 Low-T_c and high-T_c superconductors

At 4.2 K, mercury's critical temperature is too low for practical industrial use, so in the last century researchers have sought superconductor materials having higher critical temperatures. Prior to 1986, the critical temperatures of superconducting materials were too low to enable mass application for superconductors. A. Muller et al. discovered superconductivity in Lanthanum-barium-copper oxide ceramic ($LaBaCuO_4$) [17], whose critical current can reach 30 K. This temperature soon became a classification benchmark: below 30 K, superconductors are classified as low-T_c; above 30 K, they are classified as high-T_c superconductors.

Low-T_c superconductors can be metal elements, alloys, and compounds, among which Nb_3Sn and NbTi are the most common. Liquid helium is normally used as the cryogen for low-T_c superconductors, but is rare and expensive. In 1987, C. W. Chu et al. [18] observed superconductivity in $Yba_2Cu_3O_7$ (YBCO) of which the critical temperature is 93 K. One year later, Hiroshi Maeda et al. [19] discovered 2228 (BSCCO) as a superconductor with T_c just below 105 K. The critical temperatures of both YBCO and BSCCO are above the boiling point (77 K) of liquid nitrogen (LN_2) at ambient pressure. Easy availability and low cost of liquid nitrogen make engineering applications of YBCO and BSCCO possible.

YBCO and BSCCO have higher critical temperatures and also much higher upper critical magnetic fields than low-Tc superconductors, as shown in Fig. 2.4. This characteristic makes high-T_c superconductors very promising for field applications.

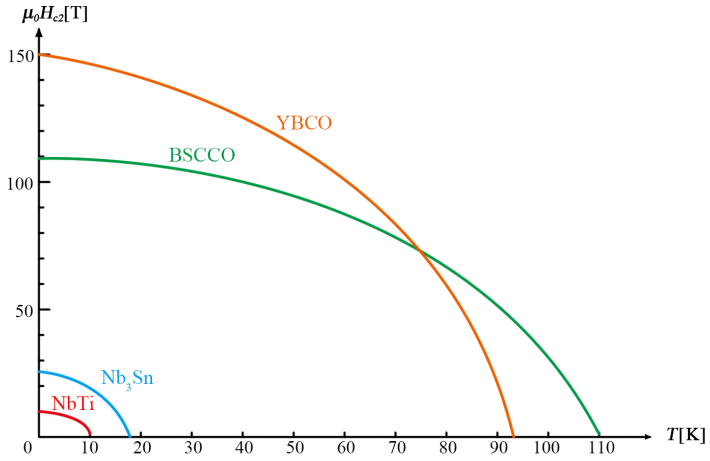

Fig. 2.4 The temperature versus upper-critical field relationship of some typical low-Tc superconductors and high-Tc superconductors (adapted from [3]).

2.2.2 Type-I and type-II Superconductors

As noted previously, superconductive materials have zero resistivity and perfect diamagnetism. However, increasing the external magnetic field causes the Meissner state to break down.

Different superconductors react differently to external fields. Some superconductors directly enter the normal state. These are classified as type-I superconductors, as shown in Fig. 2.5 (a). The magnetic field value above which type-I superconductors transition from the superconducting state to the normal state is defined as the critical magnetic field H_c.

In contrast, before entering the normal state, some superconductors come to the mixed state after the Meissner state breaks down. In the mixed state, superconductors lose perfect diamagnetism and flux can penetrate, but resistivity of the material is still zero. Further increase in the external field will drive a superconductor from the mixed state into a normal state. These superconductors are Type-II and they have two critical field values: a lower critical field H_{c1} between the Meissner state and mixed state, and an upper critical field H_{c2} between the mixed state and normal state; as shown in in Fig. 2.5(b).

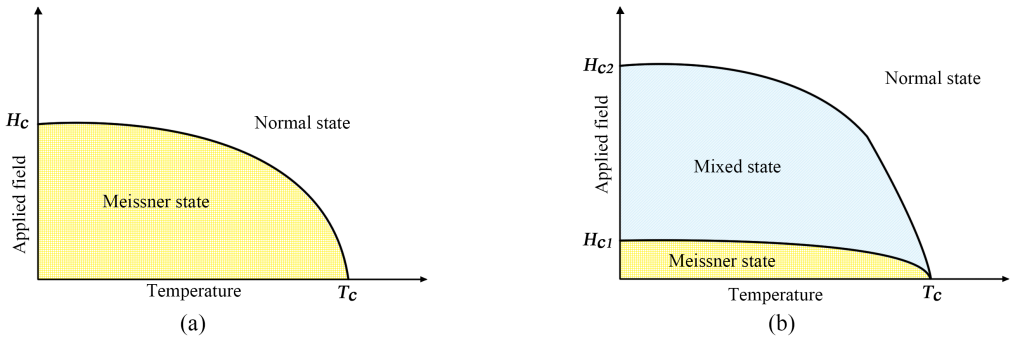

Fig. 2.5 Temperature vesus magnetic field diagram of type-I and type-II superconductors. (a) A type-I superconductors only have one critical field H_c, below which the material is in the Meissner state, otherwise it is in the normal state. (b) A type-II superconductor has two critical fields: a lower critical field H_{c1} and an upper critical field H_{c2}. Below H_{c1} the material is in the Meissner state; between H_{c1} and H_{c2} the material is in a mixed state; above H_{c2} the material is in normal state.

Type-I superconductors are mainly metals and alloys, such as Hg and Sn, whereas Type-II superconductors are normally alloys and compounds, such as MgB_2, NbTi, and YBCO, etc. The critical fields of type-I superconductors and the lower critical field of type-II superconductors are normally very low, i.e. <10 mT. Therefore type-I superconductors are not practically useful for power and magnetic applications. In contrast, the upper critical fields of type-II superconductors are much higher (27 T for Nb_3Sn, >100 T for YBCO and BSCCO) [3], making them ideal candidates for engineering applications.

The magnetization diagram of a type-I superconductor and a type-II superconductor is shown in Fig. 2.6. Type-I superconductor are perfectly diamagnetic below the critical field B_c=$\mu_0 H_c$ (the term "field" refers to both H and B in this thesis, unless elsewhere specified), i.e. the $-\mu_0 M$ equals to $\mu_0 H$, the susceptibility $\chi = M/H = -1$, and therefore the magnetic field inside the superconductor $B = \mu_0 H - \mu_0 M = 0$.

When the external field exceeds the critical field B_c the magnetization suddenly drops to zero, the magnetic field inside the superconductor is equal to the external applied field, indicating that the superconductor becomes totally normal.

The magnetization diagrams of a type-II superconductor are shown in Fig. 2.6 (b). Type-II superconductor has the same reaction to external magnetic field as type-I superconductors do when the field magnitude is below the lower critical field B_{c1}. When the external field exceeds this value, flux will penetrate into the superconductor.

In this case the magnetization $-\mu_0 M$ is lower than $-\mu_0 H$, and the susceptibility $-1 < \chi < 0$. The susceptibility gradually increases with the increase of the external field, and more

flux penetrates into the superconductor. After the external field reaches the upper critical field Bc_2 ($\mu_0 H_{c2}$), the magnetization drops to zero, the susceptibility becomes 1, and the superconductor enters a normal state.

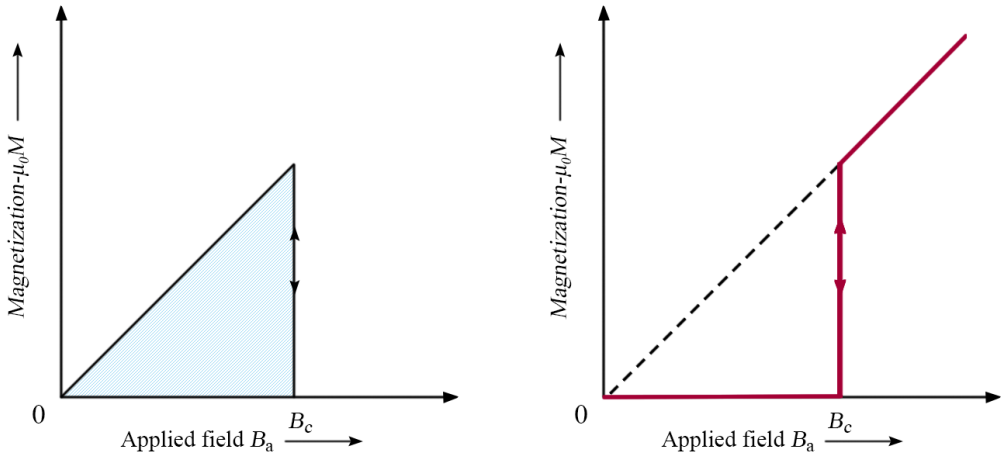

(a) Type I superconductors

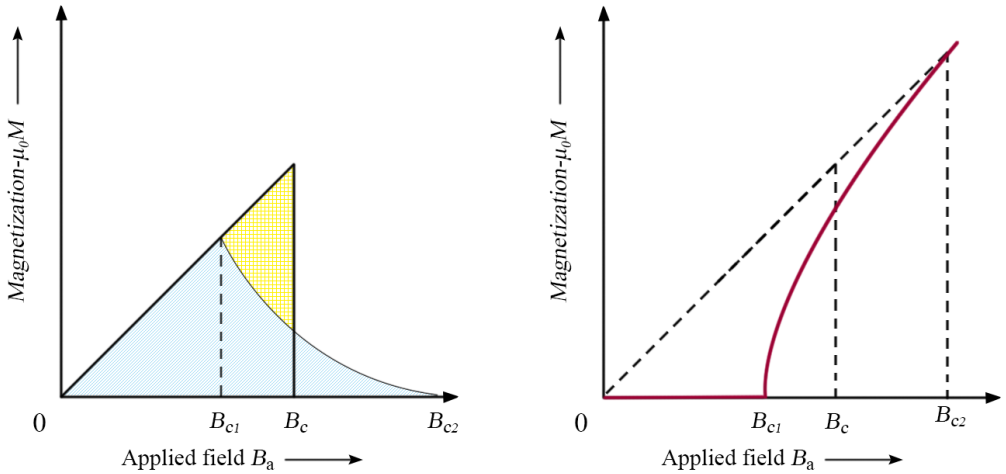

(a) Type II superconductors

Fig. 2.6 The magnetization diagrams of a type-I superconductor and a type-II superconductor (adapted from [4]).

Although the underlying physics of type-II superconductors is still unclear, it is widely accepted that the 1950 Ginzburg-Landau theory [20] can well explain the substantial difference between type-I superconductors and type-II superconductors. Two Ginzburg-Landau equations [20] describe the behaviour of superconductors, with two crucial length scales: penetration depth λ and coherence length ξ. Penetration depth (or London penetration depth) describes the length scale within which external magnetic field B decays exponentially to zero inside a superconductor, as shown in Fig. 2.7 .

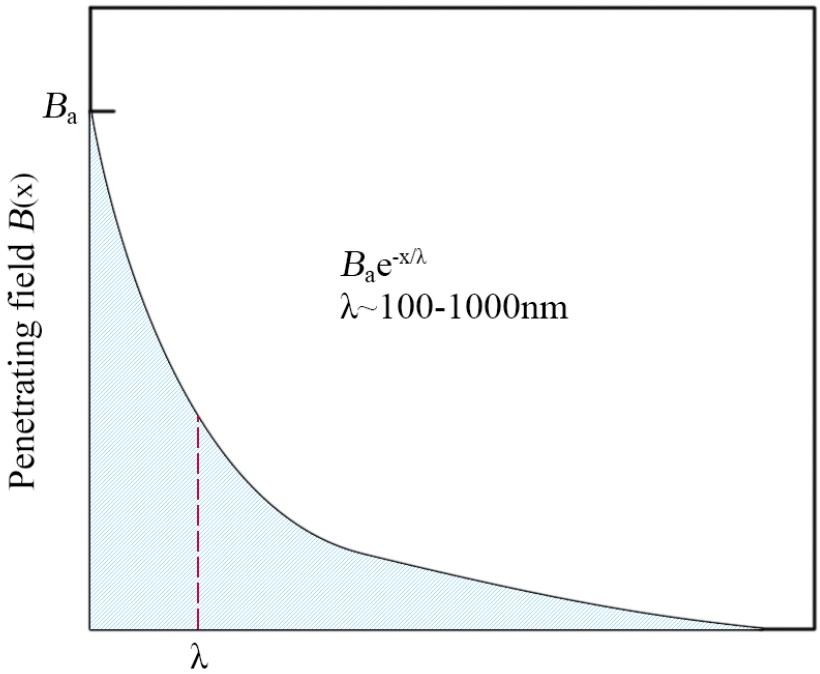

Fig. 2.7 London penetration depth. Due to Meissner Effect the external magnetic field decays exponentially to zero at the rate of penetration depth λ (adapted from [4]).

Coherence length describes the distance near the boundary of a superconductor and a normal material, in which the super electrons' (Cooper pairs [21]) density decays from a constant value in the superconductor to zero in the normal material, as shown in Fig. 2.8

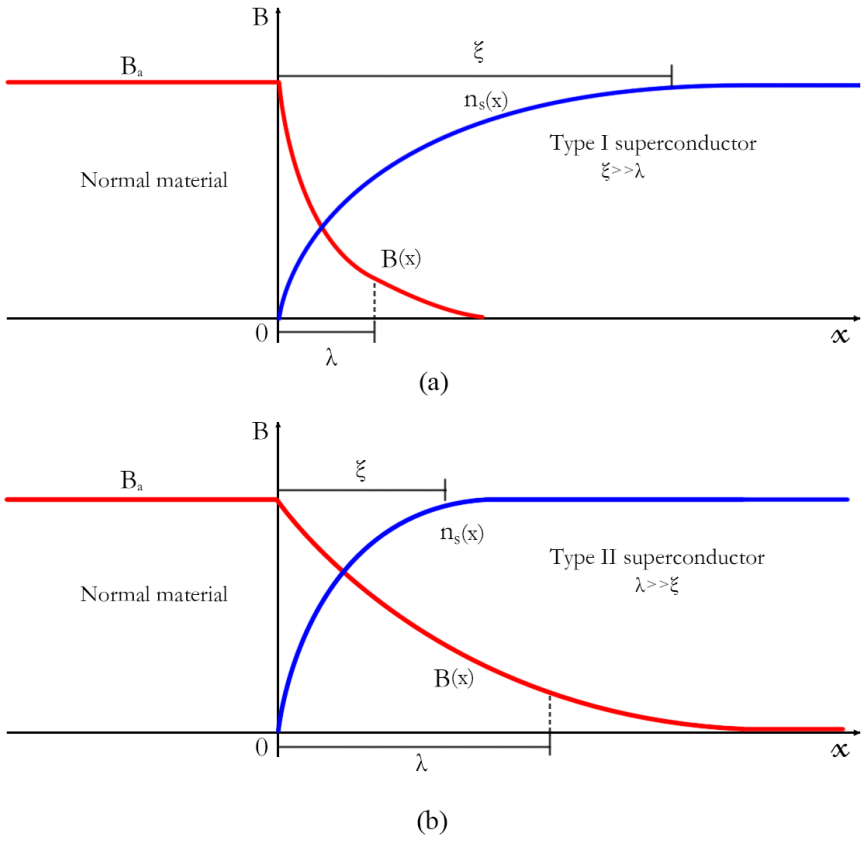

Fig. 2.8 Increase in the number of super electrons n_s and decay of the magnetic field B_a with distance x from the surface of the superconductor [5]. The coherence length and penetration depth are shown. (a) Type-I superconductor, with $\lambda \ll \xi$; (b) Type-II superconductor, with $\lambda \gg \xi$.

2.3 Microscopic characteristics of type-II superconductors: flux pinning and critical current density

When a type-II superconductor is in mixed state, magnetic flux penetrates into the superconductor. The form of flux in the superconductor is kind of like tubes, named vortices by Abrikosov [22]. According to Ginzburg-Landau theory, each vortex has a core area containing a flux quantum Φ_0, and screening currents flow around the core, as shown in Fig. 2.9 .

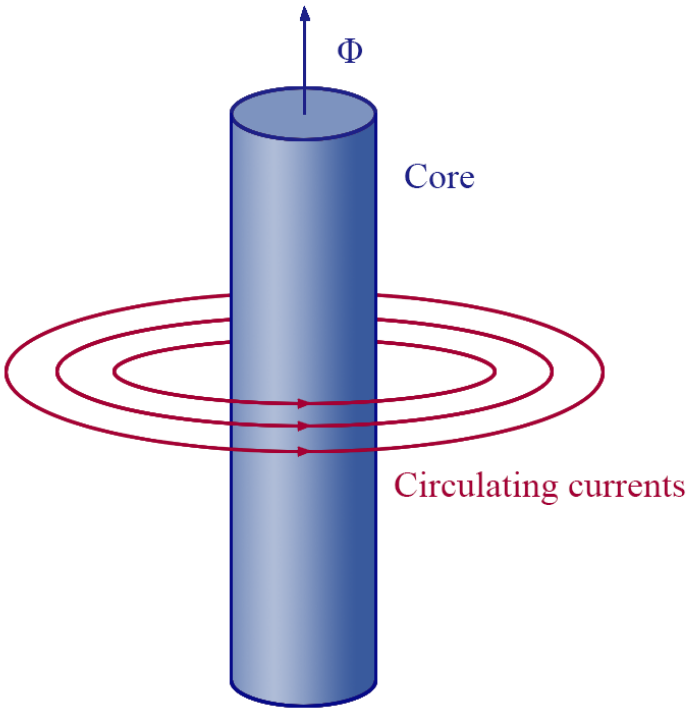

Fig. 2.9 Sketch of shielding currents circulating around a vortex core (adapted from [6]).

The core region has a radius of ξ which is the coherence length, where the super electrons' density is low and can be considered as non-superconducting. The radius of the screening current equals to the penetration depth λ within which the super current decays exponentially.

If there are two vortices close to each other, there will be a repulsive Lorentz force between the screening current of one vortex and the magnetic core of the other vortex. The Lorentz force per unit length is:

$$f_{12} = \mathbf{J_1} \times \mathbf{\Phi_0} \tag{2.3.1}$$

Where $\boldsymbol{J}_1$ is the current density of vortex 1 at the core of vortex 2, as shown in Fig. 2.10. When the superconductor does not have a transport current, there is only repulsive force between vortices. This force will keep the vortices furthest apart, with a uniform distribution to minimize the free energy. This arrange is known as the Abrikosov flux line lattice [23], as shown in Fig. 2.11 .

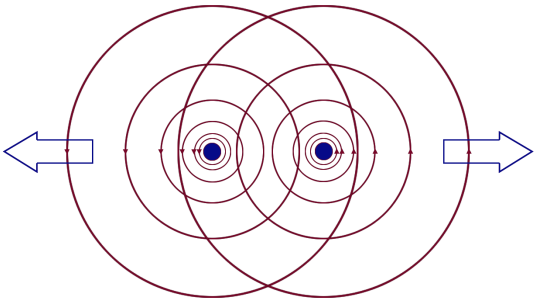

Fig. 2.10 Sketch of repulsive forces between two adjacent vortices (adapted from [7]).

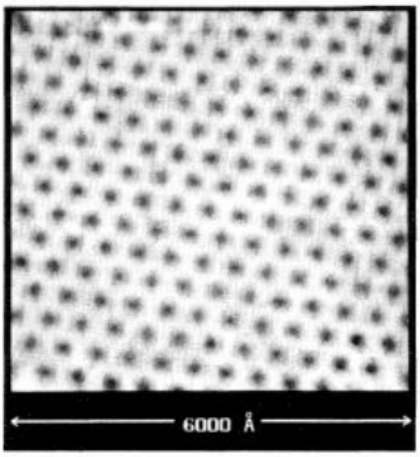

Fig. 2.11 Image of an Abrikosov flux line lattice of $NbSe_2$ at 1.8 K under a 1 T magnetic field. The figure was experimentally observed using a scanning tunnelling microscope [8].

In a pure type-II superconductor, if it is transporting a macroscopic current, there will be an average Lorentz force between the transport current and vortices:

$$F_L = \mathbf{J} \times \boldsymbol{B} \tag{2.3.2}$$

This force will redistribute the Abrikosov flux line lattice, generating an electric field which has the same direction as the transport current. Therefore ideal type-II superconductors could not transport an arbitrarily small current without a loss.

In order for the superconductors to be engineering useful, they have to be able to transport a large critical current density with little loss. This is achieved by flux pinning [24–26, 9], which prevents free motion of vortices in the superconductors. Flux pinning can be achieved

by simply making crystal defects or adding impurities into the superconductor, as shown in Fig. 2.12.

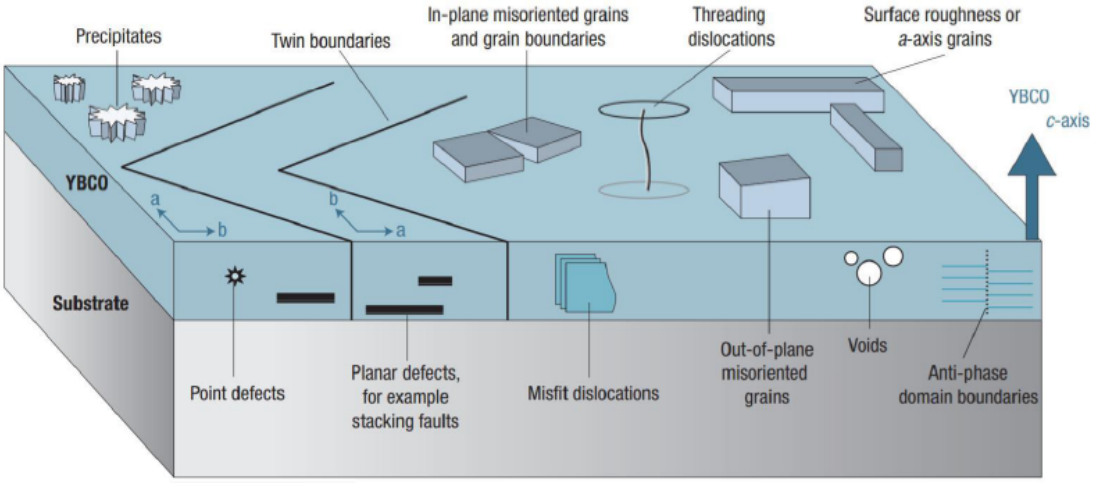

Fig. 2.12 Illustration of flux pinning in YBCO thin films [9].

The flux pinning effect can be explained by energy. The energy required by the formation of a vortex in a superconductor is proportional to its length. The energy per unit length is denoted by e_0. If a flux line has a path which includes a non-superconducting portion, the total length within the superconducting part is reduced, and thus the energy is reduced.

As shown in Fig. 2.13 the flux line at position a encounters a defect which has a length of l. The total energy forming the flux line at position a is lower than that at position b by $e_0 \star l$. Therefore to move flux line from a to b, the same amount of energy is required. So flux is pinned at position a in terms of energy.

Due to the existence of mutual repulsive forces among vortices, all vortices can be pinned in the superconductor by only a limited amount of pinning centres. Therefore, there is an averaged pinning force F_p counteracting the Lorentz force F_L. If the pinning force is larger than the Lorentz force, vortices are stably pinned, so that current can flow without dissipation. The macroscopic critical current in the superconductor can be considered as the value at which the Lorentz force is equal to the pinning force:

$$F_P = F_L = \mathbf{J_c} \times \mathbf{B} \tag{2.3.3}$$

If the pinning force is strong, the critical current density is high, and it is defined as a hard superconductor, otherwise it is defined as a soft superconductor.

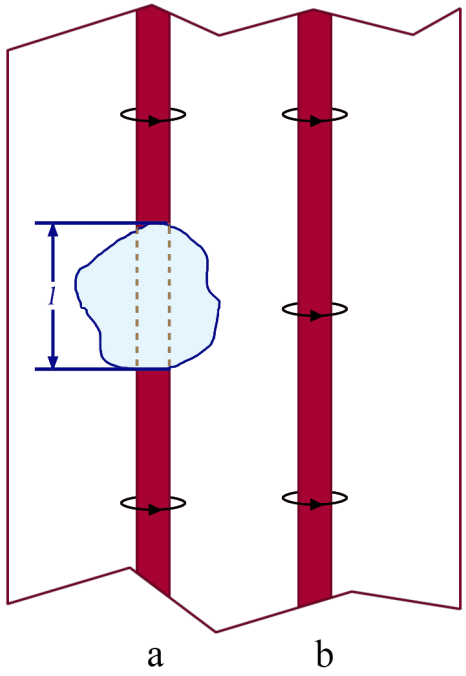

Fig. 2.13 Explanation of flux pinning effect in terms of energy [10]. The energy to form a flux line is proportional to the length of the line in the superconductor. Therefore, if there is a non-superconducting defect, the flux line has less energy, making it "pinned" at the position of the defect.

2.4 Macroscopic characteristics of type-II superconductors

2.4.1 Critical state models of type-II superconductors

In Meissner state, the magnetization is reversible. When the applied field is removed the induced screening current dies away. In a type II superconductor, the lower critical field B_{c1} is normally so small as to be negligible. Therefore in the analysis of magnetization, only mixed state is considered and Meissner state is ignored.

Critical state models are powerful tools to understand macroscopic magnetization behaviour inside a type II superconductor. These models assume that a type-II superconductor is always in a critical state, where the current density J in the superconductor is either zero or its critical current density $\pm J_c$, and the electric field E has the same direction as J if it is not zero. When there is an oscillation in the applied field, screening current with the critical density always changes sign in the outer part of the superconductor first; leaving the magnetic

field and current unchanged in the center of the superconductor. Depending on different assumptions on critical current density, there are two most widely used critical state models: Bean model and Kim-Anderson model.

(a) Bean model

The Bean model [27] was proposed by C. P. Bean in 1962. Although it is a simple empirical model which is based on experimental observations, it is a powerful tool to understand the magnetization of type II superconductors, including current and magnetic field distributions, under both field cooling and zero field cooling conditions. In Bean model, the basic assumption is that inside a hard superconductor, the current density only has three possible values: $\pm J_c$ and 0.

Current density is zero where there has never been a current flow. In this case the magnetic field is always zero. If there is magnetic flux penetration, current density takes the value of J_c or $-J_c$, and the sign is the same as the sign of the electric field induced by the changing magnetic flux. Once current density has a non-zero value, the value can only be J_c or $-J_c$, and it can never go back to zero.

The following provides a detailed description of the magnetization process of field cooling and zero-field cooling under Bean's assumption. To simplify analysis, only a simple one dimensional geometry is presented. Assuming a slab-shape type II superconductor has an infinite length in both y direction and z direction, whereas its length in x direction has a finite value of $2a$. The magnetic field is applied in z direction. This geometry is shown in Fig. 2.14.

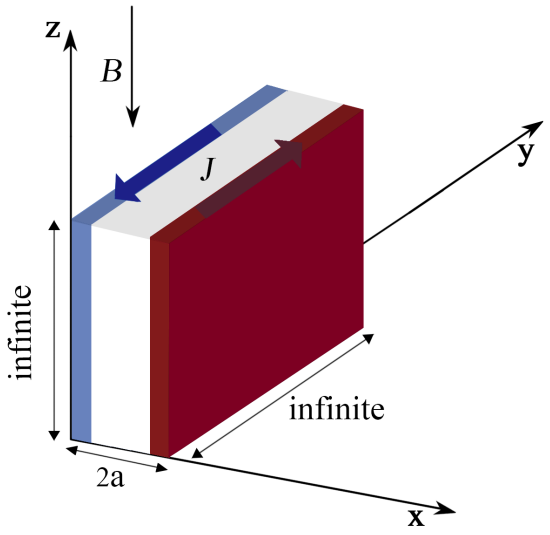

Fig. 2.14 Current distribution of an infinitely long type-II superconducting slab subjected to a homogeneous external field under the Bean model.

Considering Ampere's Law, we have:

$$\nabla \times \mathbf{H} = \mathbf{J_c} \tag{2.4.1}$$

In 3 dimensional geometry it writes:

$$\begin{bmatrix} \partial H_z/\partial y - \partial H_y/\partial z \\ \partial H_x/\partial z - \partial H_z/\partial x \\ \partial H_y/\partial x - \partial H_x/\partial y \end{bmatrix} = \begin{bmatrix} J_x \\ J_y \\ J_z \end{bmatrix} \tag{2.4.2}$$

As for the above mentioned simple one dimensional geometry, considering the Bean model, the above Equation can be simplified as:

$$\frac{dB}{dx} = -\mu_0 J_c \tag{2.4.3}$$

According to equation 2.4.1, we can see that the magnetic field gradient inside a superconductor is constant depending on the current density direction, and the penetration depth is proportional to the intensity of the externally applied magnetic field.

The magnetization process of superconductor of the above-described geometry under zero-field cooling condition is shown in Fig. 2.15. The applied magnetic field H_a increases from zero. In the beginning, the field magnitude is low, magnetic flux penetrates into the superconductor from both edges, as shown in Fig. 2.15(a). the flux penetration depth is H_a/J_c.

With the increase of the applied field, the superconductor is further penetrated until $H_a = H_p = aJ_c$, and H_p is defined as the fully penetration field. As shown in Fig. 2.15(b), at this point the flux has reached the center of the superconductor, as does the current.

Further increase in the applied field does not change the current profile, and the magnetic field everywhere inside the superconductor increases with the same rate as the applied field increase, as shown in Fig. 2.15(c).

Assuming that the magnetic field begins to decrease after reaching a maximum value of H_m which is over $2H_p$, then, the current density of the superconductor changes signs from the edges and the current density and the magnetic field of the inner part of the superconductor are "frozen", as shown in Fig. 2.15(d).

The current in the superconductor totally inversed when the applied field is decreased by H_p from the maximum value of H_m, as shown in Fig. 2.15(e).

After that point, further decrease of the applied field does not change the sign of the current, but the magnetic field everywhere inside the superconductor decreases simultaneously with the applied field. When the applied field returns to zero, as shown in Fig. 2.15(f), some magnetic field is trapped in the superconductor. The magnetic field in the center is the highest and it reduces linearly to zero in the boundaries. The maximum field the superconductor could trap is $H_p = aJ_c$, on condition that the maximum applied field H_m is over $2H_p$.

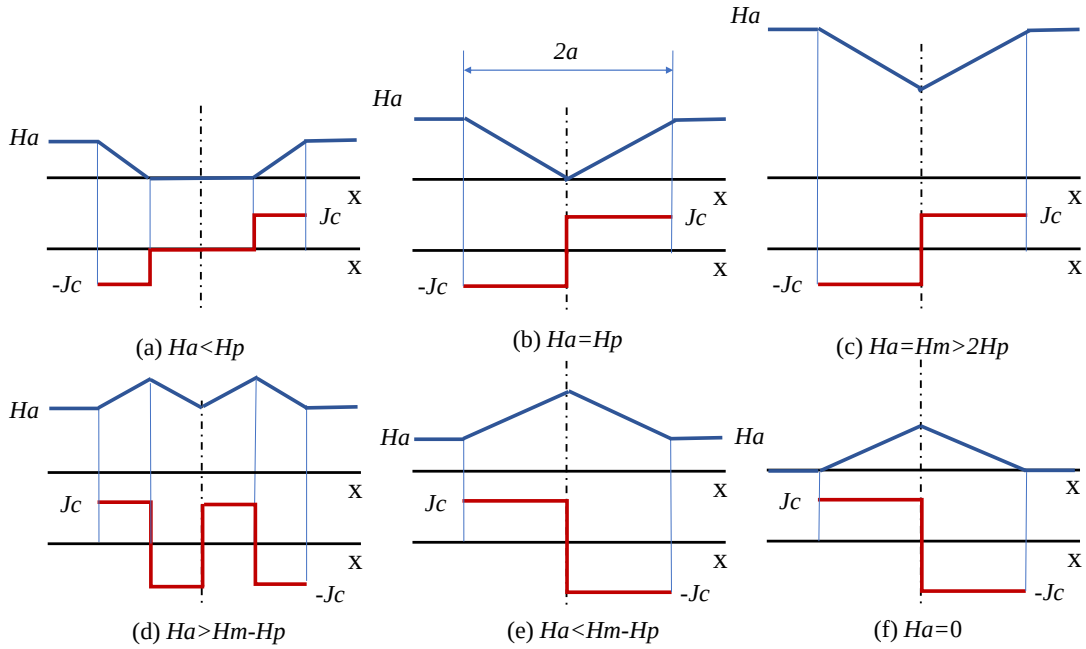

Fig. 2.15 Magnetization process of a type-II superconductor under zero-field cooling for the Bean model. The applied field H_a increases monotonously from zero to over $2H_p$, and then decreases monotonously to zero.

In contrast, Fig. 2.16 shows field cooling process. The magnetic field is applied before the superconductor is cooled below the critical temperature. After the superconductor is cooled down, the magnetic field in the whole area of the superconductor is equal to the applied field H_a (assuming $H_a \geq H_p$). But it should be noted that at this moment no current flows in the superconductor. This status is shown in Fig.2.16 (a).

When the applied field starts to decrease, the field decreases in the outer part of the superconductor, and screening current is induced to shield the change of the applied field, leaving the field in the inner part of the superconductor constant. After the applied field is reduced by H_p, the superconductor is fully occupied by screening current. This process is shown in Fig. 2.16 (b).

Further decrease of the applied field results in the field decrease everywhere inside the superconductor at the same rate. After the applied field returns to zero, as depicted in

Fig.2.16(c), a magnetic field is trapped inside the superconductor which has the same profile as the zero-field cooling case.

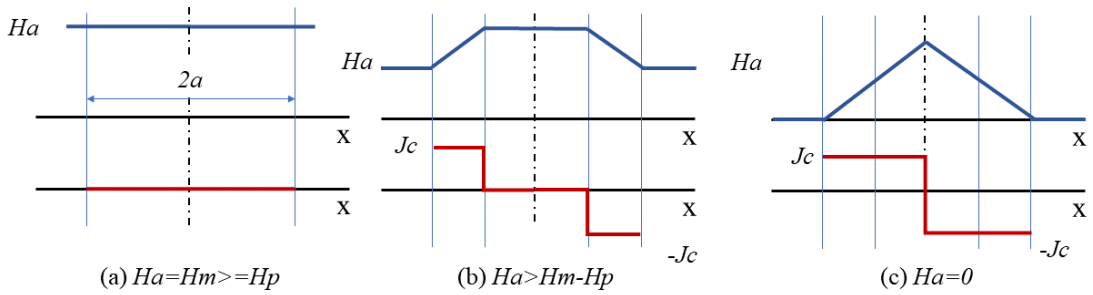

Fig. 2.16 Magnetization process of the type-II superconductor under field cooling for the Bean model. The initial applied field is H_a, and reduces monotonously to zero.

(b) Kim-Anderson Model

The Bean model describes the most ideal case where the pinning force is strong and the critical current density of the superconductor is constant irrespective of the external magnetic. Bur for practical purposes, critical current density of most superconductors is largely affected by the flux density inside the superconductor. There are various formula used to describe this characteristic, amongst them the Kim-Anderson model [28–30] is commonly used, which is written as:

$$J_c(B) = \frac{J_{c_0}}{1 + B/B_0} \tag{2.4.4}$$

Where J_{c_0} is the critical current density with no applied field, and B_0 is a constant. Equation 2.4.4 shows that the critical current density is negatively related to the flux density inside the superconductor. If the value B_0 is small, the critical current density is strongly affected by the flux density; in contrast if the value B_0 is infinitely large, the Kim-Anderson is equal to Bean model.

2.4.2 Flux creep, flux flow, and the E-J power law

In the critical state model, flux pining in superconductors is assumed ideal, where flux lines cannot move if the critical current density is not exceeded. But for practical purposes, flux pinning is affected by thermal activation for temperatures above 0 Kelvin. Even if $J \leq J_c$, vertices may still escape from pinning centers, and move in the superconductor at an insignificant rate. This process is known as “flux creep” [31–33].

For $J > J_c$, the Lorentz force imposed on the vortices in superconductors exceeds the pinning force, forcing them to move at a much more significant rate. This process is known as

flux flow [34]. Both flux creep and flux flow will induce an electric field in the superconductor and can be considered as an ohmic loss, which can be depicted as nonlinear E-J curve, as shown in Fig. 2.17.

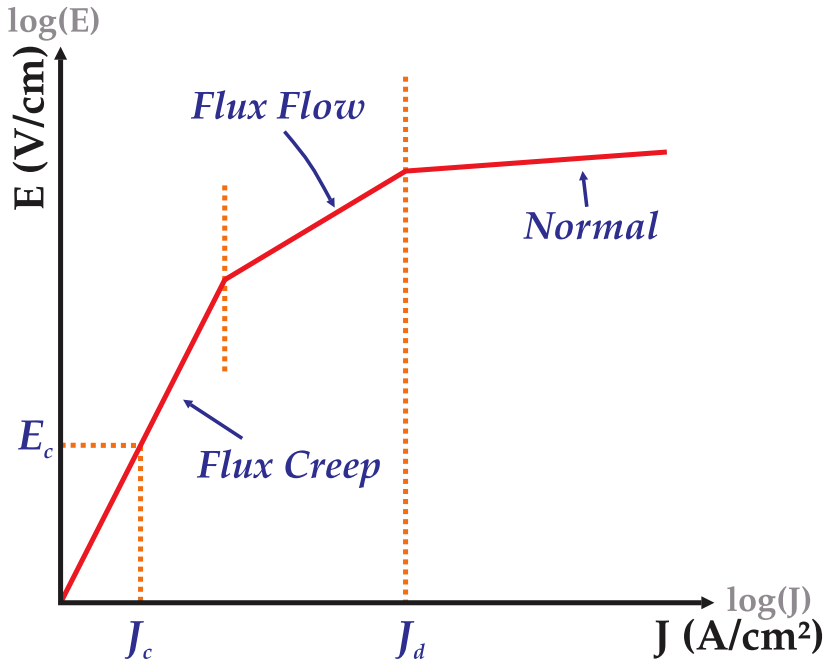

Fig. 2.17 Typical voltage-current curve of a type-II superconductor, including flux creep regime, flux flow regime, and normal state.

The E-J curve can be well fitted by an empirical exponential equation, which is known as the E-J power law [35]:

$$E = E_0(\frac{J}{J_{c_0}(B,T)})^n \tag{2.4.5}$$

Where E_0 is a constant, which is usually set as 10^{-4} V/m to experimentally determine critical current density of superconductors. $J_{c_0}(B,T)$ is defined as the critical current density, which is the current density when E equals to E_0. The n-value in equation 2.4.5 varies with material as well as temperature. Fig.2.18 illustrates the E-J curve under different n-values. Note that the critical state model is actually an ideal case of equation 2.4.5 where the n-value is equal to ∞.

2.4.3 AC loss in type-II superconductors

When a type II superconductor is transporting direct current below the critical value or is under a direct magnetic field lower than the upper critical magnetic field, disregarding flux creep effect, it is free from loss. But this is untrue under AC conditions. When the

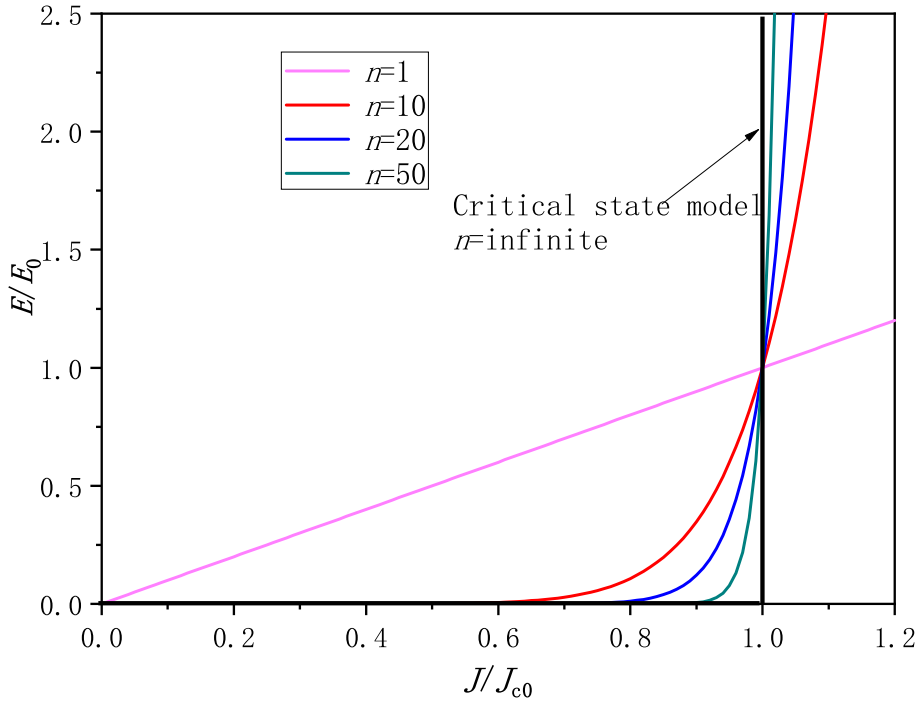

Fig. 2.18 E-J power law with different n-values. The critical state model is a specific case where $n = \infty$.

superconductor is either transporting an alternating current or is subjected to an AC field, there is hysteresis loss which is called AC loss. From electric point of view, when there is a changing magnetic field or transport current in the superconductor, there is flux motion in the corresponding position. According to Faraday's law, the moving magnetic flux induces an electric field. Considering Critical State Model, the value of current density in the superconductor can only be $\pm J_c$ or zero. At any point where there is an electric field, the current density is in the same direction as the electric field; this means that where there is electric field, there is always power loss. Considering that the alternating signal is periodical, the AC loss can be calculated as:

$$Q_{per\_cycle} = \int_T \int_V EJ d_v dt \tag{2.4.6}$$

Where Q_{per_cycle} is the total energy loss in the superconductor, per AC cycle, measured in Joule. V denotes the whole superconducting domain, and T is an arbitrary period of the AC cycle. The real average power loss P is

$$P = \frac{1}{T} Q_{per\_cycle} = \frac{1}{T} \int_T \int_V E J d_v dt \tag{2.4.7}$$

P is proportional to the frequency of the AC signal, and its unit is Watt. From a magnetization perspective, the magnetization process in the superconductor is hysteretic; this means there is a loss which is similar to the loss in the transformer iron core. The amount of loss per cycle is determined by the area of the magnetization curve, which is independent of frequency.

AC loss can be further classified as transport loss which is caused by transporting an alternating current, and magnetization loss which is a result of the external AC magnetic field. These types of AC loss may occur simultaneously when the superconductor is carrying alternating current and at the same time is subjected to an external AC field.

2.5 Conclusion

This chapter briefly introduced the fundamentals of superconductivity. Superconductors are defined as materials which have zero resistivity and perfect diamagnetism. Superconductors can be classified into low-Tc superconductors and high-Tc superconductors depending on whether their critical temperature is below or above 30 K. They can also be classified as type-I superconductors and type-II superconductors depending on whether they have a mixed state between Meissner state and normal state. Microscopic characteristics of type-II superconductors such as vortex and flux pining were briefly introduced. Because this thesis mainly focuses on the power applications of superconductors, macroscopic behaviour of superconductors such as critical state models, E-J power law, and AC loss were explained in detail.

Chapter 3

Introduction to Superconducting Fault Current Limiters (SFCL) in power systems

3.1 Superconducting fault current limiters: a promising device in power systems

With the development of economy, the demand for electricity continues to increase. More and more power plants have been connected to the power systems to cope with the increasing load. Renewable energy sources such as solar and wind farms continue to connect to the power systems as Distributed Generators (DG). In the power transmission aspect, more and more parallel transmission lines are being built to enhance the system stability as well as to deliver the increasing electricity to the loads.

One substantial challenge the above changes in the power systems brought is that the system impedance continues to drop, and the short-circuit capacity continues to rise. Therefore, the short-circuit current level has reached a tremendous level. For example, in some substations in the China Southern Power Grid, the short-circuit current level has reached 87 kA in 2010, and 105 kA in 2015 [36]. High fault current generates considerable heat as well as huge electromagnetic force which may damage power system equipment. Failure of clearing a fault may also affect the stability of the power systems. In the worst case it may cause cascade operation of relays and result in blackout.

Although circuit breakers are mature devices used to isolate short circuit faults in power systems, most commercialized circuit breakers can only isolate an AC current lower than 63 kA [37]. Over this value, the circuit breakers are technologically challenging and eco-

nomically unaffordable. Moreover, to break a fault in DC power transmission lines is more challenging, because unlike AC faults, DC faults do not have current zero-crossings.

There are various techniques to reduce the fault current level [14]. For example, adding extra impedances into the system can limit the fault current level, including using high impedance transformers, connecting serial inductors, or grounding reactors. The other way is to split the existing system to reduce the possible fault current level. But neither of these methods comes without a cost. Adding extra impedances in the power systems will incur voltage drop during normal operation. The extra impedance may also cause instability in the power systems. Extra equipment adds up the cost as well. Splitting the existing network may also be detrimental to the stability and efficiency of the system.

Superconducting Fault Current Limiters (SFCLs) are promising devices to reduce the short circuit current level, which mitigates the hazards of short circuits on the power systems equipment and reduce the demand for high capacity circuit breakers. Compared to other fault current limiting devices, SFCLs have the following indispensable advantages [38]:

1) In most types of SFCLs, the systems are intrinsically safe. The change from zero resistance to nonzero resistance is self triggering. The fault current itself activates the SFCL, being independent of the external communications of triggers.

2) The impedance is negligible under normal operation conditions.

3) The current flow is not interrupted so that the detection of the short circuit location is not hampered.

4) In some SFCLs, the limited current level can be easily adjusted.

5) SFCLs can automatically recover after fault, normally within one minute, which is much more convenient than using a fuse that must be replaced.

SFCLs can not only be used for limiting the fault current during a short circuit, they also have other potentially important functions in the power systems.

One example is to limit the transformer inrush current [39]. Inrush current normally occurs when a transformer which connects a low load is switched into the power systems. It results from the saturation of the transformer iron core. The phenomenon is very hazardous, because it may damage transformers, cause the mal-operation of the relay protection, and induce heavy harmonics into the power systems. Superconducting fault current limiters can be a simple and effective way to limit the inrush current when the transformer is switched on as well as limiting the fault current when the feeders have a short circuit.

SFCL can also be used to improve the fault ride-through capability of Double Fed Induction Generator (DFIG) based wind turbines [40]. When a short circuit fault occurs in wind farm connected with DFIG base wind turbines, the stator current of the wind turbine increases and a voltage drop will appear at the generator terminals. This will also incur a severe over-current in the rotor due to magnetic coupling. The converter at the rotor side will be blocked and the wind turbine may be tripped. In severe cases this may incur cascade tripping in the wind farm. Therefore it is very much desired to maintain the wind turbines connected to the system during a fault, which is called fault ride-through capability. SFCLs can be an ideal solution to this problem because they can not only limit the fault current level but also mitigate the voltage drop across the terminations of the wind turbines.

Furthermore, SFCL can coordinate with the energy storage systems, providing an efficient way to limit the fault current as well as to improve the power qualities such as compensating for voltage sags and reducing momentary outages [41].

SFCL may also be a potential solution for reducing the high start-up current of high power induction motors [42].

The following section will provide a brief review of SFCLs, including mechanisms, structures, performance evaluation, and introduction of existing projects.

3.2 A brief review of fault current limiters

3.2.1 Resistive SFCLs

Basic mechanisms

Resistive type SFCLs (R-SFCLs) are simple but promising devices to limit the fault current in the power grids. The basic principle of R-SFCLs is the nonlinear resistivity and temperature-phase transition of superconductors, as shown in Fig. 2.17 and Fig. 3.1. During normal operation, the current flowing through the superconductor is lower than its critical value. Despite some negligible AC loss, the total loss is very low and the equivalent resistance seen by the power systems is very small. During a short-circuit fault, the grid current exceeds the critical current of the superconductor, and a non-negligible resistance appears to limit the current. Depending on the status of the superconductor during fault, R-SFCLs can be divided into two types: the flux flow type and the quench type.

Flux flow type R-SFCLs use flux flow resistance to limit fault current [43]. During fault occurrence, the superconductor works in the flux flow region of the E-J curve, as shown in Fig. 2.17. Because the temperature rise is insignificant, the superconductor is not quenched. An obvious advantage of this type of R-SFCL is that the superconductor returns to the

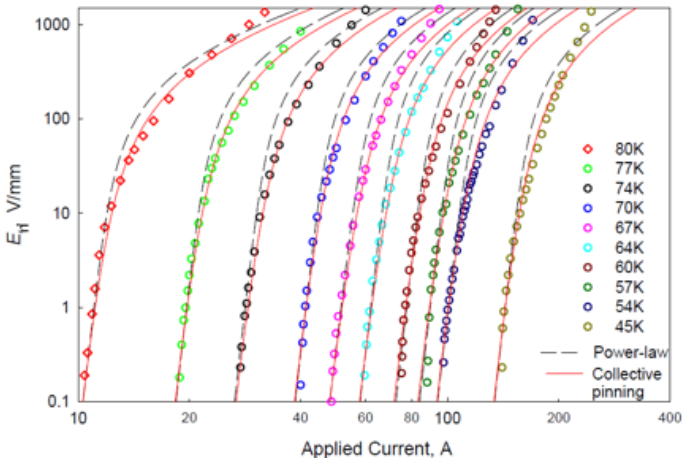

Fig. 3.1 V-I curves of a YBCO coated conductor under different temperatures [11].

superconducting state as soon as the current reduces to under the critical value. Therefore the recovery time is much shorter compared to typical R-SFCLs, ensuring continuous operation of the power systems. However, due to the fact that flux flow resistance is normally much lower than the normal resistance after quenching the superconductor, a much longer length of superconducting material has to be used to provide enough resistance, and therefore the cost is much higher. Furthermore, the flux flow resistivity depends on the instantaneous value of the transport current. Under AC conduction, it is difficult to ensure that the fault current is within the range of the flux flow region.

In quench type R-SFCLs, the critical current of the superconductor is set much lower than the fault current level. During a fault the grid current greatly exceeds the critical current of the superconductor. The generated ohmic loss heats up the superconductor to above its critical temperature. The superconductor suddenly quenches and presents a significant normal resistance to limit the fault current. Quench type R-SFCLs present much higher resistance than the flux flow type R-SFCLs per unit length of superconductor. Therefore less superconductor is needed, and the cost is lower. One drawback of quench type R-SFCLs is that the recovery time is longer, several seconds for thin film superconductors and up to minutes for bulk superconductors [15]. The longer recovery time imposes difficulties on the coordination of relay protections such as circuit breaker re-closure.

In both flux flow type and quench type R-SFCLs, rather long lengths of superconductor have to be used. In long length superconductors, it is practically impossible to keep I_c uniform. Therefore, in the inception of a short circuit, the over-current only exceeds the critical current of individual parts rather than the whole length of the superconductor in the fault current limiters. Due to the low Normal Zone Propagation Velocity (NZPV) of the superconductor [44] (especially for the widely used commercial coated conductors), massive

heat will dissipate at these local zones, and quench the superconductor instantaneously. This phenomenon is called hot-spots. The hot-spots are totally unfavourable because they overheat the superconductor and may cause permanent damage or even destruction of the superconductor. To mitigate the hazard of hot-spots, a shunt resistor R_p is used to parallel the superconductor.

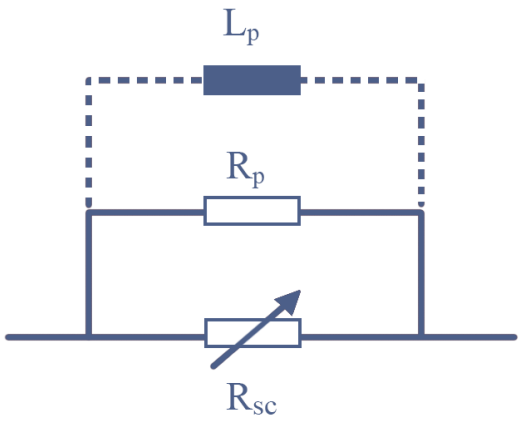

Fig. 3.2 Schematic drawing of a resistive type SFCL, where R_{SC} represents the resistance of the superconductor, R_p is a shunt resistor to mitigate hot-spots in the superconductor, and L_p is a shunt inductor.

During a fault, some current bypasses the local normal zones of the superconductor and flows through R_p, reducing the local heat accumulation. To ensure a satisfactory bypass performance, R_p should be in contact with the superconductor over its whole length, which is normally achieved by adding stabilizing layers and coating layers in the coated conductors.

Active quench of R-SFCLs

To further deal with the problem of non-uniform quench caused by hot-spots and low normal zone propagation velocity, several active quenching strategies using external magnetic fields have been proposed.

The first strategy uses a normal conducting coil connected in parallel to the superconductor [45], as shown in Fig. 3.3. The normal conducting coil is coaxially with the superconducting tube in space. During normal operation, most current tends to flow in the superconductor, so that the normal conducting coil is bypassed. During over-current, however, some current flows through the normal conducting coil generating a magnetic field which is applied to the superconducting tube. The magnetic field reduces the critical current of the superconductor, thus accelerating the quench and mitigating the hot-spot problem.

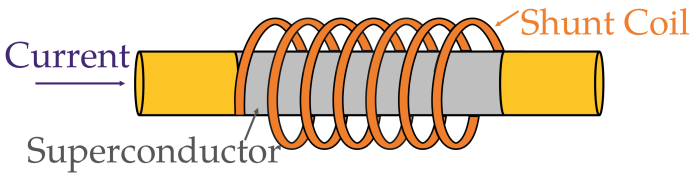

Fig. 3.3 Schematic arrangement of a magnetic field assisted R-SFCL [12]. The shunt coil connects in parallel with the superconductor, and they are arranged concentrically. During a fault some current will flow through the shunt coil, thus generating a magnetic field which reduces the critical current of the superconductor.

The second technique is for thin film R-SFCL. A thin copper coil is co-wound with the superconducting film [13], as shown in Fig. 3.4. After the fault is initiated, a radio frequency current is applied to the copper coil, which generates a radio frequency field to the superconducting film. The field generates a loss in the superconductor which can quench the superconductor uniformly along its length and cross section. This technique can not only solve the problem of hot-spots, but can also accelerate the quench at lower level of over-current. The third technique is similar to the second one in terms of structure, however a kilo-Hz field rather than a radio frequency field is used [46]. The underlying physics is the phenomenon of dynamic resistance which occurs when a superconductor transporting a DC is subjected to an AC field. This technique is less demanding on the power supplies which drive the field coil.

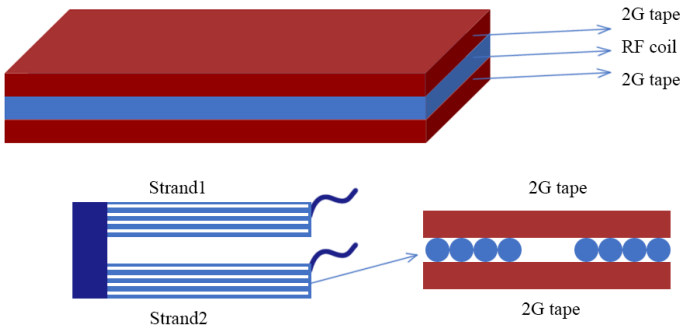

Fig. 3.4 Schematic arrangement of a radio frequency magnetic field assisted R-SFCL [13]. The RF coil is co-wound with the superconductor. During a fault an RF magnetic field will be applied to the superconductor. The RF field can help quench the superconductor swiftly and uniformly, eliminating hot-spots.

Materials and structures

In an early stage LTS materials such as NbTi were used in the R-SFCLs [47], yet HTS materials such as YBCO, BSCCO, and MgB2 [48] have since dominated. The materials can

be manufactured in the form of bulk tubes or wires. Recently, the second generation (2G) YBCO coated conductors have become the most popular material for R-SFCLs, owing to their outstanding electrical and mechanical properties. In terms of shape, R-SFCLs can be built in the form of meander [49], multifilar pancakes [50], braid solenoid [51], non-intersecting solenoid [51], etc.

Advantages and disadvantages:

The advantages of R-SFCLs include: simple design; compact with low volume and weight; negligible impedance under normal operation.

The disadvantages of R-SFCLs including:

1) The superconductors are directly connected into the power systems. For high voltage transmission systems the electric insulation for the superconductors may be complicated. Considering power system reliability, R-SFCLs are normally developed for low voltage and medium voltage power systems rather than high voltage transmission systems.

2) Thick current leads which go from room temperature to cryogenic temperature have to be used, which generates considerable heat load in cryogenic systems, even without a transport current. The heat load per current lead is estimated to be 40-50 W/kA at low temperature. [15]

Current projects

R-SFCL is the most popular type of SFCL amongst all its counterparts. During the past two decades, quite a few R-SFCLs have been developed and tested in the USA, Japan, UK, EU, and China. Table 3.1 lists some major projects [12].

Table 3.1 Main resistive SFCL projects in the world

Country/Company	Specifications	Material	Year/ ref
Germany/Siemens	765 V/ 135 A	YBCO	1999[52]
EU/Superpoli project	20 kV/ 2 kA	2G HTS	2003[53]
Germany/ACCEL-Nexans	6.9 kV/ 600 A	Bi2212	2003[54]
Japan/Mitsubishi	200 V/ 1 kA	YBCO	2004[55]
USA/DOE-EPRI	8.6 kV/ 800 A	Bi2212	2005[56]
Italy/ CESI	500 V/ 80 A	Bi2223	2005[57]
UK-Germany/ASL-Nexans	12 kV/ 800 A	Bi2212	2009[58]
Japan/Toshiba	6.6 kV/ 600 A	2G HTS	2009[59]
USA/IGC-Superpower	138 kV/ 1.2 kA	2G HTS	2009[60]
UK/ASL	11 kV/ 400 A	Bi2212	2012[61]
Korea/KEPRI	22.9 kV/ 630 A	2G HTS	2012[62]
China/SJTU	10 kV/ 200 A	2G HTS	2012[63]
Germany/Ensystrob project	12 kV/ 533 A	2G HTS	2012[64]
EU/Eccoflow project	24 kV/ 1 kA	2G HTS	2013[65]

3.2.2 Saturated iron core fault current limiters

The fundamental concept of the saturated iron core type SFCL (SISFCL) was first proposed by B. P. Raju in 1982 [66]. The configuration of a single-phase SISFCL is shown in Fig. 3.5.

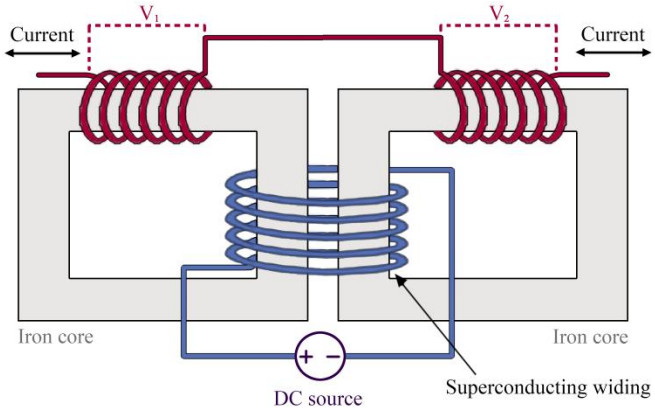

Fig. 3.5 Structure of a saturated iron core SFCL [14]. It consists of two series connected AC windings, a DC winding, and a pair of closed iron cores.

It consists of two AC windings, a DC winding, and a pair of iron cores. Each AC winding is warped around one of the iron cores, and the DC winding is wrapped around both of the iron cores. The two AC windings are connected in series and connected into the power systems. The DC winding is powered by a DC current source. It can be formed either by normal conductors or by superconductors, yet normally superconductors are used to minimize the normal operation loss. Ideally, the DC winding experiences zero flux generated by the two AC windings because they cancel each other. Therefore, there are few electromotive forces generated in the DC winding. The B-H curve of the iron cores is shown in Fig. 3.6.

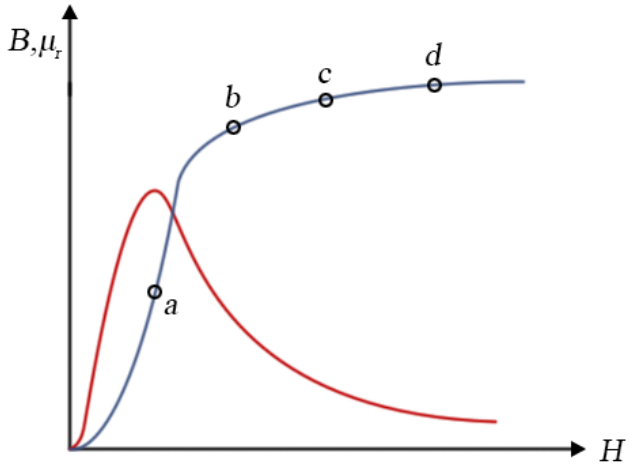

Fig. 3.6 BH curve and the relative permeability of a typical silicon steel core.

Working principle:

During normal operation, both of the iron cores are driven into the deep saturation zone by the DC winding. It is designed so that during normal operation the relatively small power system current is unable to de-saturate the iron core. The power system voltage drop across the AC windings can be written as:

$$V = \frac{d\Phi}{dt} = nS\frac{dB}{dt} = K\mu_r\mu_0\frac{dH}{dt} \tag{3.2.1}$$

where Φ is the total flux linking the AC windings, n is the total number of windings, S is the area of the windings, K is a constant determined by n and the length and cross section of the iron cores, and μ_r is the relative permeability. Due to the fact that the iron core is deep saturated during normal operation, the relative permeability μ_r is very close to one. This can be considered as H oscillates between point b and point c in Fig. 3.6.

During the fault condition, the current in the AC windings increases substantially, so that each iron core may be de-saturated during the corresponding half-cycle of the AC current. As shown in Fig. 3.6, H oscillates between point a and point d, and at around point a, one core is de-saturated and presents high impedance. Because the two cores are saturated in opposite directions, they will alternatively be de-saturated during each AC cycle, thus limiting both the positive and negative fault current.

Advantages and disadvantages:

The advantages of SISFCL include:

1) SISFCL is a non-quench type,meaning that during fault occurrence, the device can limit the fault current immediately since there is no quench happening in the superconductor. Therefore, the recovery time can also be very short.

2) The superconducting coil is operating in the DC mode, rather than in AC mode, and hence the power loss is negligibly small.

3) Unlike resistive type SFCLs, which are normally designed for low voltage grids or medium voltage grids, SISFCL can be used in high voltage power systems.

4) The fault current limiting level is controllable by adjusting the DC coil current, making the device more flexible.

The advantages of SISFCL include:

1) The SISFCL needs to use a considerable amount of steel, resulting in large volume and heavy weight.

2) During fault, after the iron-core is de-saturated, there is a high inductive voltage in the DC winding which may damage the DC power supply.

3) There may be large harmonic components in the voltages and currents during a fault due to the non-linear B-H curve of the iron core. To solve the problem of induced hazardous high AC voltage, an active type SISFCL is proposed [14]. The main ideal of the active type SISFCL is to open the DC power source after detecting a fault in the power systems. This depends on the detection of a fault within miliseconds of the time of the fault occurrence, and High Voltage Insulated Gate Bipolar Transistors (HVIGBT) are used to break the circuit.

Main application projects:

Due to the above mentioned advantages of the SISFCL, quite a few projects have been conducted in different voltage level power systems, and the field tests have shown the effectiveness of the devices. In 2008, a 35 kV/ 90MVA saturated iron core SFCL was developed, tested, and installed in the China Southern Power Grid. In 2009, a 15 kV/ 1.2 kA SFCL was developed in the USA by Zenergy [67]. In 2012, a 11 kV/ 1.25 kA SFCL was developed in the UK [61]. In the same year a 220 kV/ 300 MVA SFCL was developed and installed in Tianjin, China [68]. Based on the successful experience of the 220 kV SFCL, researchers are building a 500 kV SFCL in China [69].

3.2.3 Inductive type SFCLs

The first type of inductive SFCLs to be introduced is called shielded iron core SFCL [70]. The structure and equivalent circuit are shown in Fig. 3.7. The device consists of a primary winding and a secondary winding which are co-wound around a closed iron core. The primary winding is made of copper and is connected to the power grid. The secondary winding is formed by a closed superconducting loop.

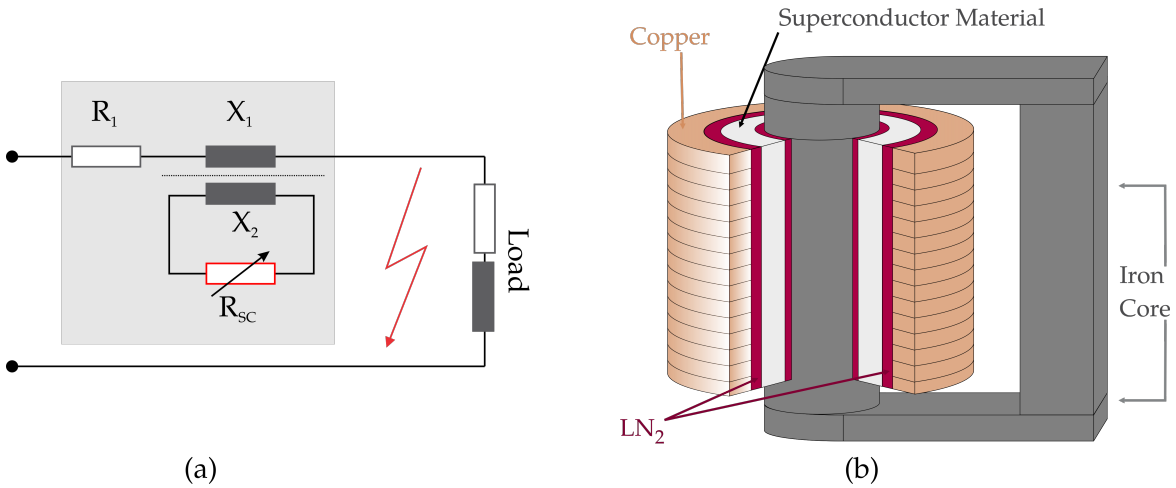

Fig. 3.7 Iron core inductive fault current limiter (adapted from [12]). (a) Equivalent circuit, (b) Structure.

During normal operation, the current in the primary winding tends to induce a shielding current in the closed secondary winding. The shielding current is less than the critical current of the secondary superconductor. The shielding current therefore expels most of the flux lines in the iron core generated by the primary winding. The impedance of the device seen by the grid is the resistance of the primary winding R_1 and the leakage inductance X_1 (neglecting the AC loss in the secondary). Due to the close coupling of the two windings the leakage inductance is very small. Therefore during normal operation the device presents a very

low impedance to the power grid. It works just like a transformer with perfectly shorted secondary. During a short-circuit fault, the primary current rises substantially, which may drive the secondary shielding current above the critical current of the superconductor. The secondary winding becomes resistive, indicating that flux is able to penetrate into the iron core. The device then presents a non-negligible impedance to limit the fault current below a certain level. It works as a transformer with a resistive load connected in the secondary.

One evident advantage of the device is that the superconductor is electrically isolated from the power grid, so it is more reliable. The superconductor works in a closed cryogenic system without the need for current leads which generate considerable heat loss. The disadvantage is that the device consists of an iron core, so that the size and weight is much larger than a resistive type FCL with the same power rating.

To deal with the problem of size and weight of the shielded iron core SFCL, researchers from KIT proposed an air coil SFCL, as shown in Fig. 3.8.

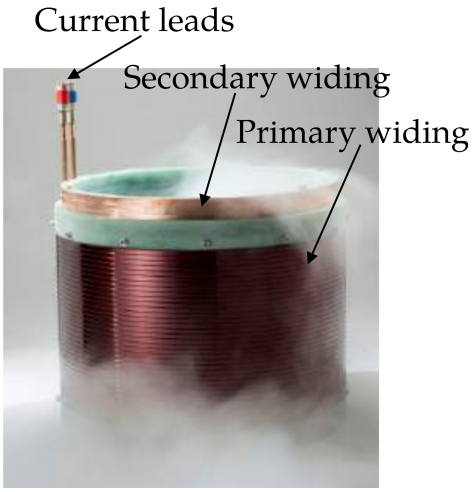

Fig. 3.8 Air core inductive fault current limiter [12].

The working principle of this device is the same as a shielded iron core SFCL. The difference is that in this device the primary winding and the secondary winding are coupled by air rather than an iron core. One advantage of this design is that it is much more compact and less heavy compared to the iron core SFCL. Moreover, compared to R-SFCLs it does not need the current leads therefore the loss is much lower. One possible drawback of this device is that the coupling between the primary winding and the secondary winding is not as good as that of the iron core SFCL, therefore the impedance of the device during normal operation could be higher than the iron core one and the impedance during a fault could be lower.

In 1996, a 10.5 kV/70 A inductive SFCL prototype using BSCCO cylinders was developed by ABB and installed in a Swiss hydropower plant [71]. In 1997 a 6.6 kV/400 A prototype was developed in Japan, which was also based on BSCCO cylinders [72].

3.2.4 Bridge type SFCLs

The circuit topology of a bridge type SFCL is shown in Fig. 3.9[73]. Each phase of the SFCL consists of a full-bridge rectifier made of 4 diodes $D_1 - D_4$, a DC power supply, and a superconducting inductor. During normal operation, the DC power supply charges the superconducting inductor to over the peak value of the normal operating AC current. The four diodes are conductive with low resistance. The AC current bypasses the inductor hence the device presents a low impedance. During a fault, the AC current from the grid rises sharply and the peak values exceeds the DC current, and it will alternatively block diodes D_1, D_2, and D_3, D_4. The current is forced to flow through the inductor. Specifically, with the current direction defined in Fig. 3.9, when the positive peak AC current is over the DC current, the diodes D_3 and D_4 are blocked and the current commutates to the inductor via the diodes D_1 and D_2; alternatively when the negative peak AC current exceeds the DC current, the diodes D_1 and D_2 are blocked and the current flows through the inductor through diodes D_3 and D_4. The peak AC current is thus limited by the inductor. Practically it may also possible to use a normal inductor rather than a superconducting inductor, but in this case the size of the inductor is much larger and the DC voltage has to be higher.

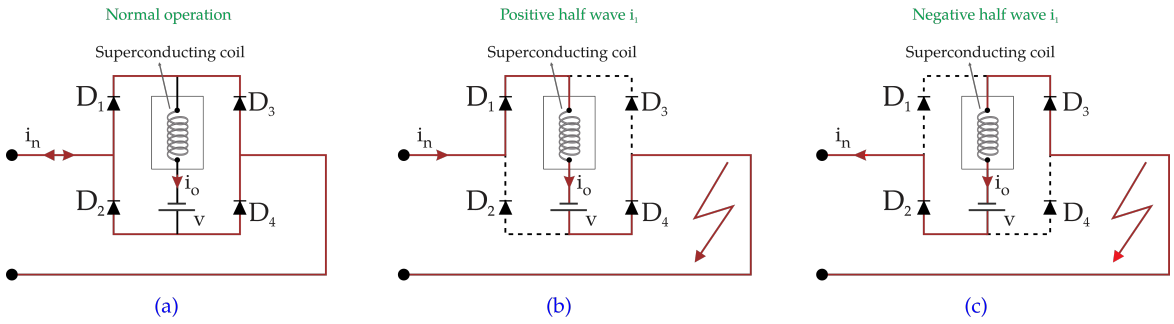

Fig. 3.9 Circuit of a diode bridge type SFCL [15].

There are several advantages of the bridge type SFCLs:

1) The device can limit a fault as soon as the current is over the threshold value, so there is no time delays;

2) The fault current limiting threshold is flexibly adjustable by setting the DC current;

3) No quench occurs during faults, therefore the recovery time is very short;

4) During normal operation, the AC current does not flow through the superconductor, therefore the AC loss is very low.

There are several advantages of the bridge type SFCLs:

1) The device is not fault-safe, meaning that if any of the diodes fail the result will be the failure of limiting the fault current;

2) The total loss on the diodes is not negligible during normal operation;

3) The device requires fast trip of the circuit breaker since the diodes cannot withstand a high fault current for a long time.

Several bridge type SFCLs have been developed and tested for low voltage power grids, including a 10.5 kV/1.5 kV prototype in China [74], a 6.6 kV/ 36 A prototype in Japan [75], and a 6.6 kV/200 A prototype in Korea [76].

3.2.5 Other types of FCLs

Apart from the four types of fault current limiters introduced above, there are various other types of FCLs, including flux lock type SFCL [77], flux-coupling type SFCL [78], composite type SFCL [79], hybrid type SFCL [80], etc. As they are not as popular as the above mentioned FCLs, the relevant description will not be elaborated in detail in this work.

3.3 Summary

This chapter introduces Superconducting Fault Current Limiters (SFCLs) in power systems.

Modern power systems have encountered the problems intolerably high short-circuit current. SFCLs are promising devices for limiting the increasing fault current level. They have little impedance during normal operation but considerable impedance during faults, making them superior to other fault current limiting devices.

The second section gives a brief review of superconducting fault current limiters. Several types of SFCLs are introduced, including resistive type SFCLs, saturated iron core type SFCLs, inductive type SFCLs, and bridge type SFCLs. Their working mechanisms are analyzed, their advantages and disadvantages are compared, and existing projects are introduced.

The following chapters are intended to investigate some of the influences the SFCLs may bring to the power systems.

Chapter 4

YBCO tapes optimization for SFCL device

4.1 High temperature superconductor materials for SFCL

Ever since the discovery of high temperature superconductors materials in 1987, HTS wires and tapes have been intensively researched and fabricated. Although a large number of HTS materials have been discovered, only three of them have been developed for practical applications: first generation Bi-based (Bi-2212, Bi2223) superconductors and second generation (RE)BCO tape (rare earth barium copper oxide elements). 2G tapes enjoy higher critical current, improved in-field performance, and stronger mechanical configuration, as well as a better performance-price ratio.

There are many parameters that determine the required properties of an HTS tape: the size or power level and the correlated operation temperature of the device and the nature of the current, DC or AC, and, in particular, the AC frequency [81].

4.1.1 2G high temperature superconductor tape structure

The structure of a typical commercially available 2G HTS YBCO tapes is usually composed of stabiliser, superconducting layer, buffer, and substrate.

Substrate layer

It is paramount to choose a suitable substrate to grow a high-quality YBCO superconducting layer. Lattice size, crystal structure, coefficient of thermal expansion, mechanical properties, chemical compatibility and price should be considered when selecting a substrate. Theoret-

ically, Pt, Pd, Ag, Ni, Cu can all be employed as the substrate for HTS tape. However, Pt and Pd are too expensive while Ag and Cu suffered from the poor mechanical properties. Therefore, Ni and its alloys are good candidates for the substrate. A commonly used substrate, Hastelloy, is such a type of Ni-based alloy, which has high resistivity and thus low AC loss. It is worth noting that one effective way to increase the J_e of the tape is to use a thinner substrate because J_e is inversely proportional to the total thickness of the wire [17].

Buffer layer

Because superconductors easily react to metallic elements, a buffer layer is used to segregate the superconducting layer and substrate and thus to prevent chemical reaction between them. Buffer layer materials should meet four requirements: (1) good mechanical properties; (2) adhesive quality to the substrate; (3) lattice and heat coefficient compatible with the superconducting layer and substrate; and (4) successive, dense, even-textured and low in defects. $Y_2O_3, CeO_2, MgO, SrTiO_3$, YSZ, Gd_2O_3, and Eu_2O_3 are viable materials for the buffer layer. To get a desirable block effect, a multiple-layer construction is adopted by many HTS companies such as AMSC, and Shanghai Superconductor. A typical hierarchical structure of a buffer consists of a cap layer, barrier layer, and seed layer. As the first layer of a buffer, the seed layer grows directly on the substrate, and therefore its heat coefficient and lattice structure should match with those of the substrate material. The barrier layer prevents mutual diffusion of particles between the substrate and superconductors. The cap layer provides a continuous, smooth, compact, and seamless growth template for the superconducting layer's epitaxial growth.

Superconducting layer

Yttrium barium copper oxide (YBCO) is the most developed 2G HTS material and is a family of crystalline chemical compounds, many of which have the general formula $YBa_2Cu_3O_7 - \delta$ (also known as Y123). The structure of the materials depends on the oxygen content that is denoted by δ in the chemical formula. When $\delta = 1$, the structure is tetragonal and the tetragonal form of YBCO does not super-conduct. Increasing the oxygen content changes the structure to orthorhombic, with lattice parameters of a = 3.82, b = 3.89, and c = 11.68. Optimum superconducting properties occur when x = 0.07 [4]. Conduction in the copper planes confines conductivity to the a-b planes. Along the c axis, normal conductivity is 10 times smaller than in the a-b plane. Furthermore, the superconducting length scales show similar anisotropy, in both penetration depth ($\lambda_{ab} \approx 150$ nm, $\lambda_{c} \approx 800$ nm) and coherence length, ($\lambda_{ab} \approx 2$ nm, $\xi_{c} \approx 0.4$ nm nm). Although the coherence length in the a-b plane is 5

times greater than that along the c axis, it is quite small compared to classic superconductors such as niobium (where $\lambda \approx 40$ nm). Fig. 4.1 is a diagram for the atomic structure of three common HTS materials including YBCO.

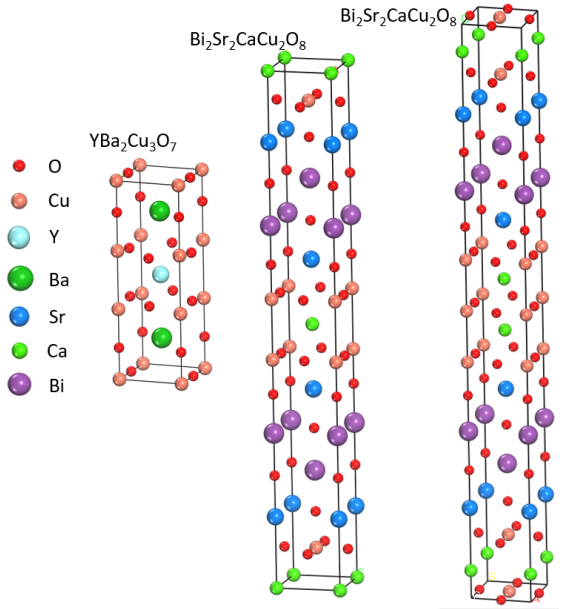

Fig. 4.1 Atomic structure of three common HTS materials.

Stabilizer

The stabilizer layer consists of a thin silver layer and a thicker copper layer. Once a superconducting film is deposited, it needs to be over-coated with metallic layers for electrical contacts. Nearly all metals react strongly with the superconductor apart from silver and gold. Compared to gold, silver is cheaper and thus is always used as an over-layer on top of the superconducting film. Sputtering and evaporation have been employed to coat silver. In addition to a 2 um-thick silver over-layer, a thicker copper layer also needs to be applied to the conductor to provide stabilisation in case of over-currents.

YBCO tapes for SFCL

Fig. 4.2 shows a typical 2G YBCO tape for SFCL. The superconducting layer is sandwiched between copper layers and stainless steel layers. The copper layer provides the superconducting layer with over-current protection when the steady-state current exceeds the critical current of the superconductor. Specifically, for a tape whose critical current is 250 A, if the transport current is below 250 A, all current will flow through the YBCO layer, and the superconductor is in the superconducting state. However, if the transport current is above 250

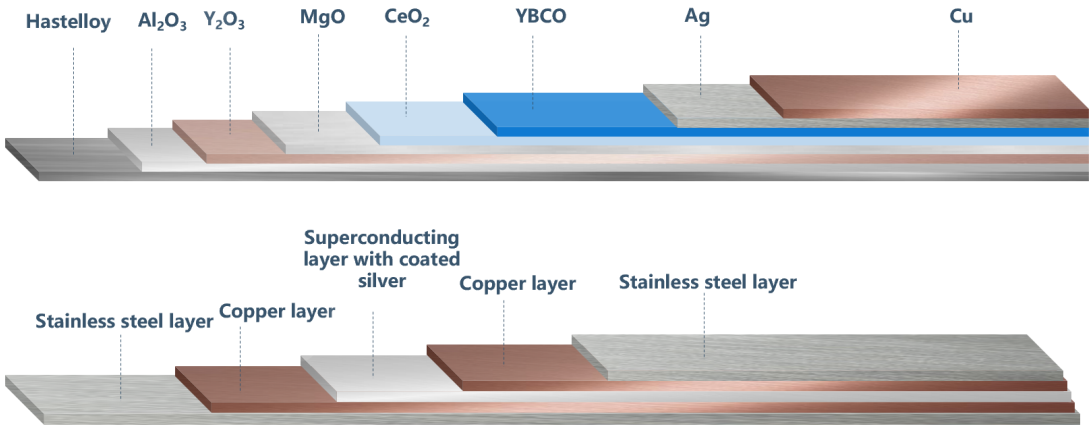

Fig. 4.2 YBCO Hierarchical structure of the 2G YBCO tapes employed in the resistive SFCL. Structure refers to the tapes from Shanghai Superconductors Technology Co Ltd.

A, for instance 280 A, in this case, 250 A current will go through the superconducting layer, and the remaining 30 A current will go through the copper layers with 15 A passing through each layer. Therefore, the steady-state 15 A passing through over-current ability of this 2G YBCO tape depends on the thickness of the copper layer. Stainless steel encapsulation is specially used for SFCL because of its strong mechanical properties. It can also help share some extra current and help reduce temperature rise.

Here we propose the design of two YBCO tapes with different mass (23 g and 28 g). It is assumed that both tapes have the same resistance under room temperature. According to

$$R = \rho \frac{L}{S} \tag{4.1.1}$$

and the Parallel Resistance Formula

$$\frac{1}{R} = \frac{1}{R_1} + \frac{1}{R_2} + \frac{1}{R_3} + \ldots + \frac{1}{R_n} \tag{4.1.2}$$

the sizes of different materials can be calculated. The details of the multiple-layer structure are listed in Table 4.1 and Table 4.2. In the following section, we will use these two types of tapes to conduct a series of experiments.

Table 4.1 Specifications of SSTC 28g YBCO tape for SFCL

material	length (m)	width (mm)	thickness (um)	cross-sectional area (mm2)	volume (mm3)
copper	1	10	2.3	0.0230	0.20
silver	1	10	2.11	0.0211	0.22
YBCO	1	10	1	0.01	0.10
hastelloy	1	10	50	0.5	4.45
stainless steel	1	12	160	2.64	21.07

Table 4.2 Specifications of SSTC 23g YBCO tape for SFCL

material	length (m)	width (mm)	thickness (um)	cross-sectional area (mm2)	volume (mm3)
copper	1	10	3.9	0.0390	0.35
silver	1	10	2.11	0.0211	0.22
YBCO	1	10	1	0.10	0.01
hastelloy	1	10	50	0.5	4.45
stainless steel	1	12	220	0.35	15.32

4.2 Experimental study

4.2.1 Experimental system

An experimental system was set up to investigate the response of different coated conductors to pulsed over-current. As shown in Fig. 4.3, the system consists of a YOKOGAMA FG 120 Function Generator FG, which generates a 50 Hz signal of only 5 continuous cycles in 100 ms time. This signal was amplified by a high current source to produce a high current of hundreds of Amperes. We applied the current to the coated conductor samples. A YOKOGAWA DL850 oscilloscope was used to measure and record the voltage across the coated conductors. The sampling rate was 50 Ks/s.

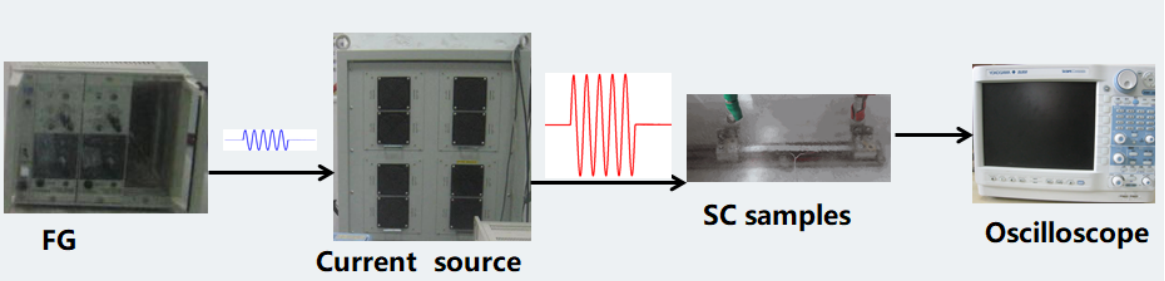

Fig. 4.3 Schematic drawing of the pulsed-current test system. A Function Generator (FG) generates a 50 Hz signal which has 5 continuous cycles. A high current source amplifies this signal and outputs a pulsed current of hundreds of Amperes applying to coated conductor samples. An oscilloscope is used to measure the voltage response of the coated conductors to the pulsed current.

It was expected that during all the tests, the pulsed current waveform and magnitude would remain the same. However, practically it is very difficult to control the current source to output exactly the same current. To rule out the influence of the difference in the pulsed current, the author designed a series sample connector, as shown in Fig. 4.4. During each test, two coated conductor samples were connected in series, to ensures that the currents applied to them were identical. Two pairs of voltage taps were used to measure the voltage of the coated conductors. In each pair, the two ends of the voltage tap were separated by 4 cm. Each pair of the voltage taps was closely twisted to minimize any possible induction noise which may affect the measurement accuracy.

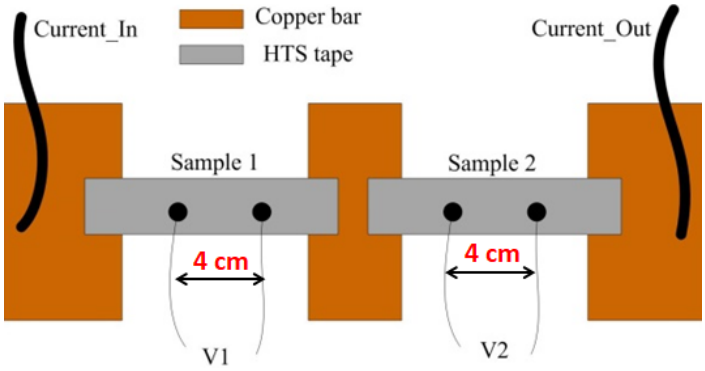

Fig. 4.4 Schematic drawing of the connection of the sample tapes with the pulse current.

Three types of HTS coated conductors were used in the study, including two manufactured by Shanghai Superconductor Technology Co. Ltd (SSTC), and one manufactured by American Superconductors (AMSC) (as shown in Fig. 4.6). The SSTC tapes have a mass of 23 g/m and 28 g/m respectively, and they are denoted as SSTC 23 g tape and SSTC 28 g tape, respectively. The AMSC tape has a mass of 23 g/m and it is denoted as AMSC 23 g tape.

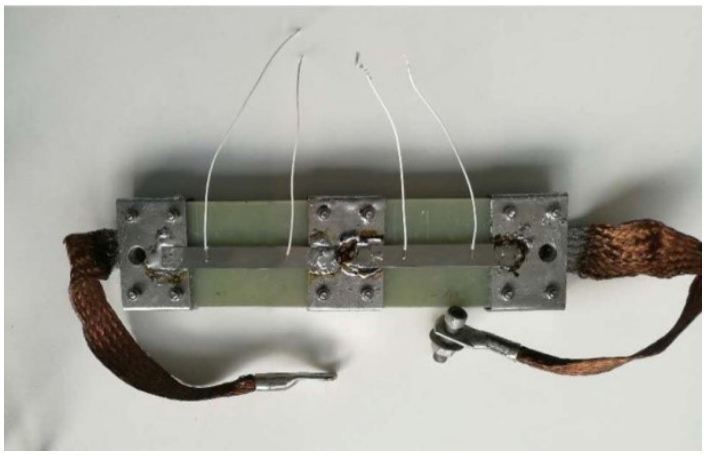

Fig. 4.5 Picture of the connection of the sample tapes with the pulse current. In each measurement the two samples are connected in series so that the currents flowing through the tapes are identical. The voltage of each tape was measured by a pair of voltage taps which were separated by 4 cm.

Fig. 4.6 Photo of the three types of superconducting coated conductors used in the experiment. (a) SSTC 23 g tape, (b) SSTC 28 g tape, (c) AMSC 23 g tape.

In the following experiment, all the critical current values were acquired in LN at 77 K unless otherwise specified.

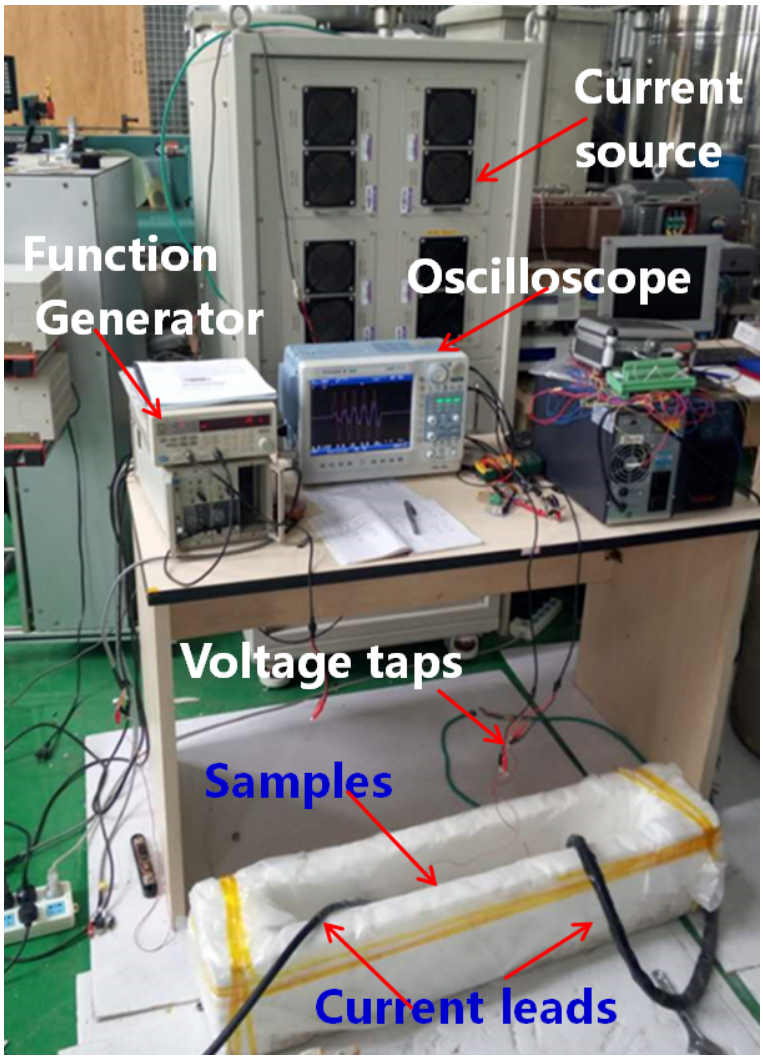

Fig. 4.7 A photo of the experimental system.

4.2.2 Experiment and result

In the following experiments, the peak value of the 5 cycles of pulsed current was about 750 A, as shown in Fig. 4.8. This value may have changed marginally from one test to another, but in each text, the two samples experienced identical current. Each test was conducted for at least 3 times to rule out randomness, and the trends in the 3 trials were consistent, therefore one set of results from each test is presented.

Comparison between 23 g tapes and 28 g tapes

In the first test, we used two pieces of SSTC tapes for comparison. One was SSTC 23 g tape with a critical current of 243 A, and the other was SSTC 28 g tape which has a critical

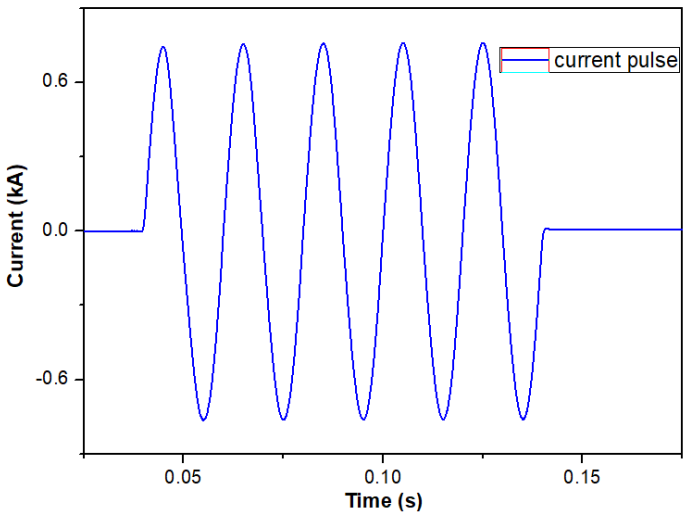

Fig. 4.8 Waveform of the current pulse applied to the superconducting samples.

current of 244 A. Because the critical current values of the two samples were very close to each other, the main differences between them were the thickness of the silver layer, copper layer and laminated stainless steel layer.

Fig. 4.9(a) shows the current and tape voltage waveforms. The results show that although the current peak value was constant, the voltage of both tapes continuously increased over successive cycles. The voltage of the SSTC 23 g tape remained higher than the voltage of the SSTC 28 g tape over time, and their difference varied. In the first half cycle, the voltage of the SSTC 23 g tape was close to that of the SSTC 28 g tape. However, the gap becames larger and larger over time.

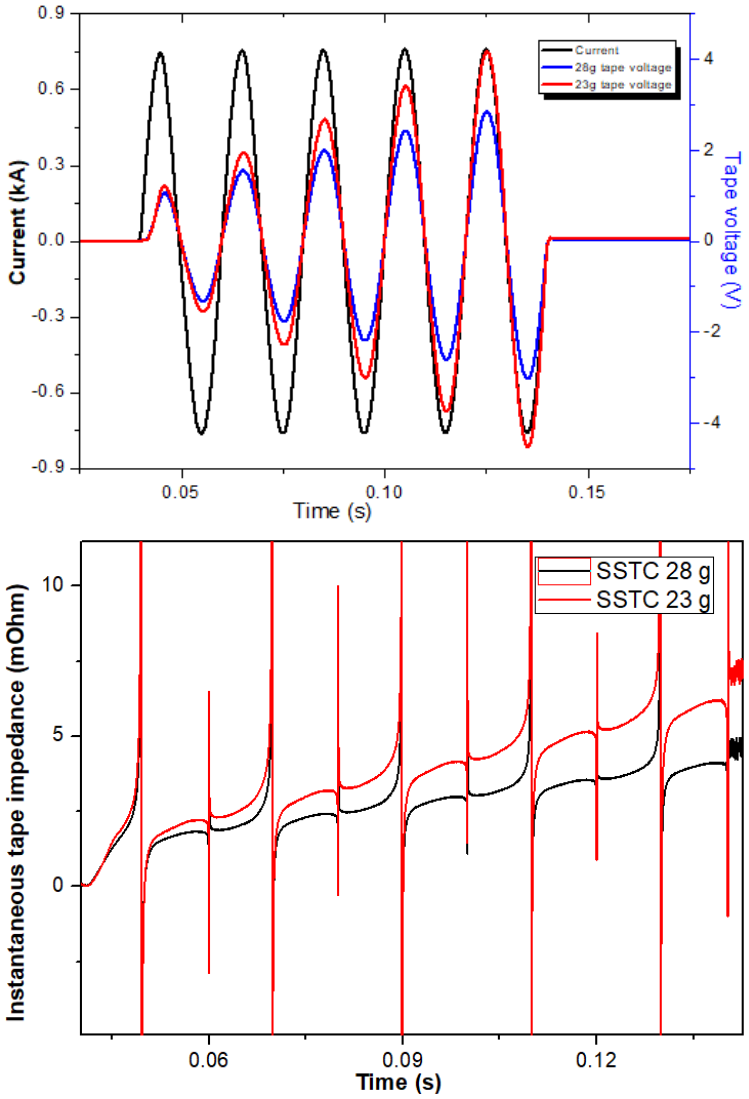

Fig. 4.9 Test result of the SSTC 23 g tape and SSTC 28 g tape with similar critical currents. (a) Voltage and current curves. (b) Instantaneous tape impedance value.

The increase in the voltages indicates that the tape resistance was increasing. The impedance of each tape is calculated by dividing the instantaneous tape voltage by the instantaneous current value, which is shown in Fig. 4.9(b). It should be noted that due to the existence of the tape inductance, there was a slight phase difference between the current and the tape voltage. Therefore, at the time of current zero crossings, the instantaneous impedance values reached a very high level. If we neglect these bits, we can clearly see that the tape impedance (or simply consider it as the resistance) kept increasing, and the resistance of the SSTC 23 g tape increased faster than that of the SSTC 28 g tape.

In the second test, the characteristics of AMSC 23 g tape and SSTC 28 g tapes were compared. The piece of AMSC 23 g tape has a critical current of 290 A, whereas the piece of SSTC 28 g tape has a critical current of 266A. The voltage curves and the instantaneous resistance values are plotted in Fig. 4.10. The results show that although the critical current of the AMSC 23 g tape is 24 A higher than the critical current of the SSTC 28 g tape, the resistance of the AMSC 23 g still increased faster than the 28 g tape.

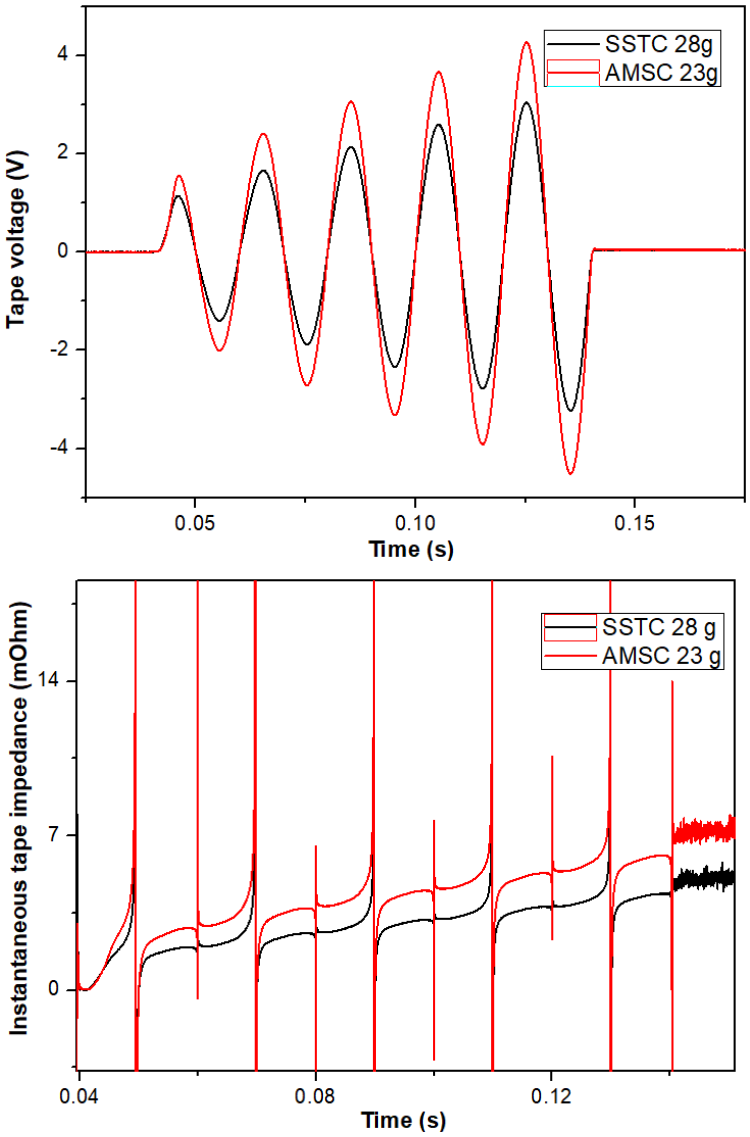

Fig. 4.10 Test result of the AMSC 23 g tape and SSTC 28 g tape. The piece of AMSC 23 g tape has a critical current of 290 A whereas SSTC 28 g tape has a critical current of 266 A. (a) Voltage and current curves. (b) Instantaneous tape impedance value.

Comparison between tapes with different critical current values

Here we aim to investigate the influence of the tape critical current on the pulsed current response. Therefore two pieces of SSTC 28 g tapes were deliberately chosen as the sample. The two tapes were identical in terms of structure, room temperature resistance, etc., except that one has a critical current of 274 A and the other has a critical current of 245 A. The test result is shown in Fig. 4.11.

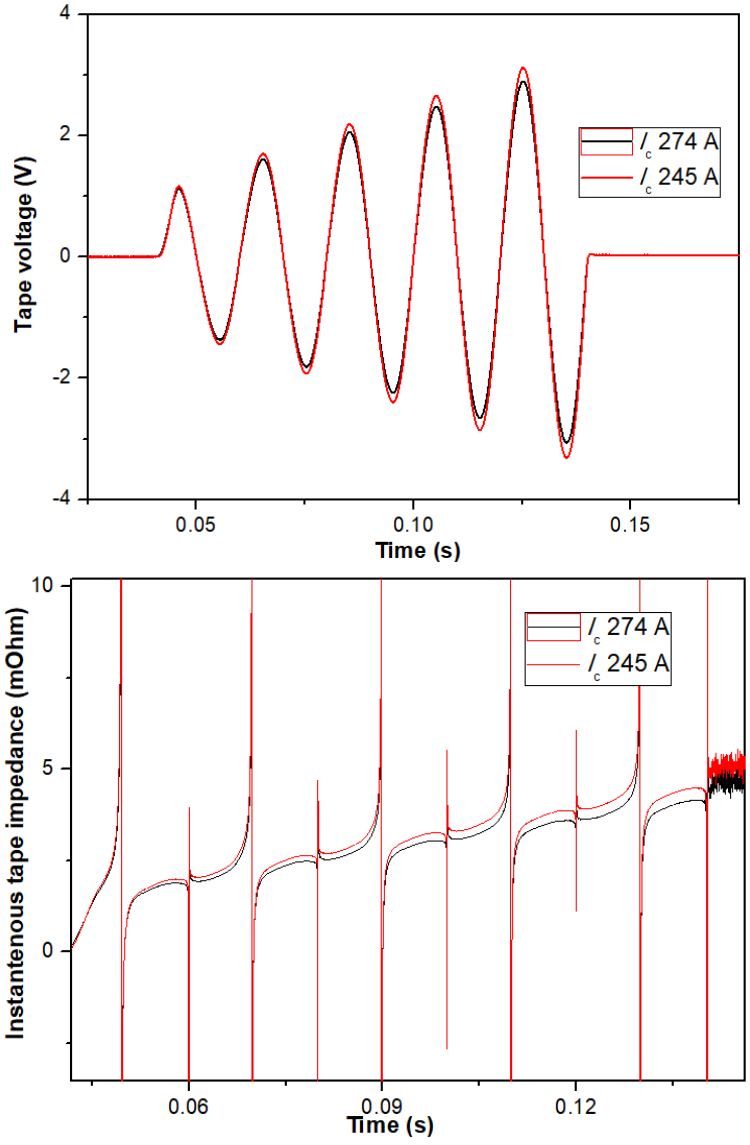

Fig. 4.11 Test result of the two SSTC 28 g tapes with different critical current values of 245 A and 274 A. (a) Voltage and current curves. (b) Instantaneous tape impedance value.

It is clear from the curves that the voltage and impedance are negatively related to the critical current of the tape. Although there is a critical current difference of about 30 A between the two tapes, the differences in the responses, however, were very much close. This may be because the pulsed current magnitude was much higher than the critical current of the tapes so that the difference of the critical currents is negligible. This result is very indicative of future fault current limiter design because it shows that the critical current homogeneity is not so significant for constructing long superconducting tapes.

Comparison between AMSC 23 g tape and SSTC 23 g tape

This test examined the voltage response to pulsed over-current of two types of 23 g tapes, i. e. the AMSC 23 g tape and the SSTC 23 g tape. The critical current of the SSTC 23 g tape is 240 A, whereas the critical current of the AMSC tape is 290 A. Their room temperature resistances are also different, 125 $m\Omega/m$ for the SSTC 23 g tape, and 120 $m\Omega/m$ for the AMSC 23 g tape. The results are shown below in Fig. 4.12.

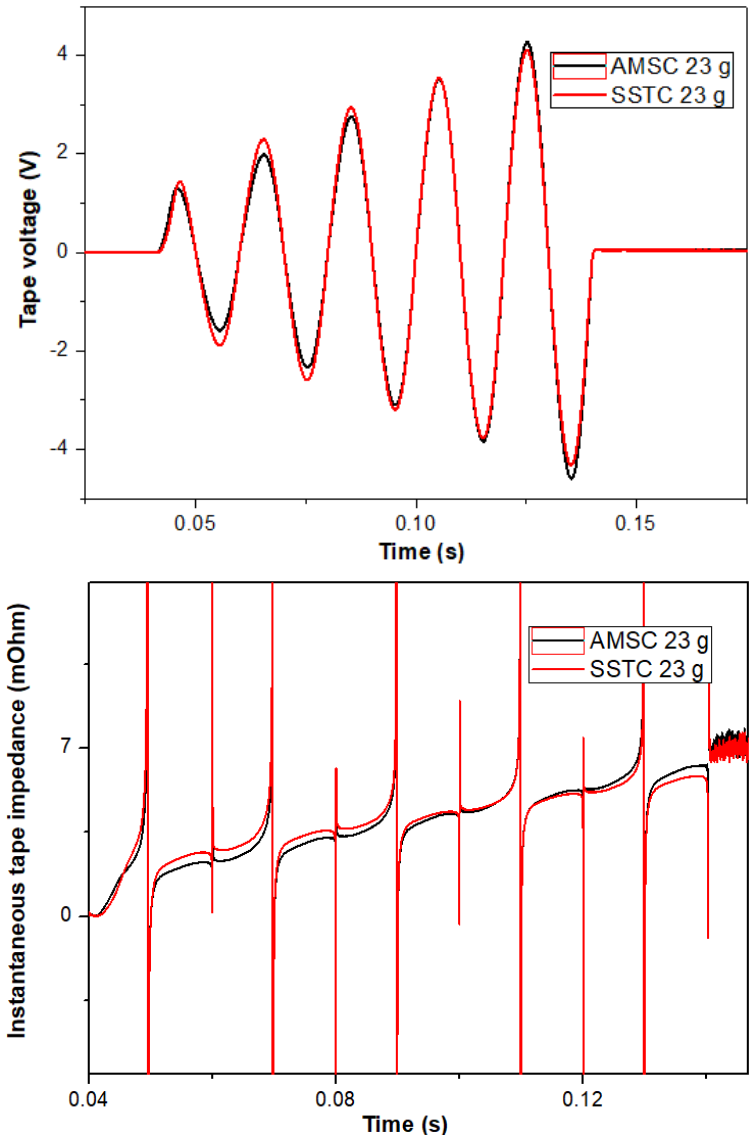

Fig. 4.12 Test result of SSTC 23 g tape with critical current of 240 A and AMSC 23 g tape with critical current of 290 A. (a) Voltage and current curves. (b) Instantaneous tape impedance value.

The results seem to be irregular. In the first three cycles the SSTC 23 g tape had a higher voltage whereas in the 5th cycle the voltage of the AMSC tape became larger. The result will be explained in the following session.

4.2.3 Qualitative analysis and discussion

During the current pulse, when the instantaneous transport current exceeded the critical current of the superconductor, the extra amount of current flowed in the shunt layers, as shown in Fig. 4.13. The equivalent electric circuit is shown in Fig. 4.14, with the resistance of the superconductor (denoted by R_{ybco}) and the resistance of the shunt layers (denoted by R_{shunt}). Under a certain over-current level, the current distribution between R_{ybco} and R_{shunt} and the voltage across the tape are all depending on the V-I curve of R_{ybco} and R_{shunt}.

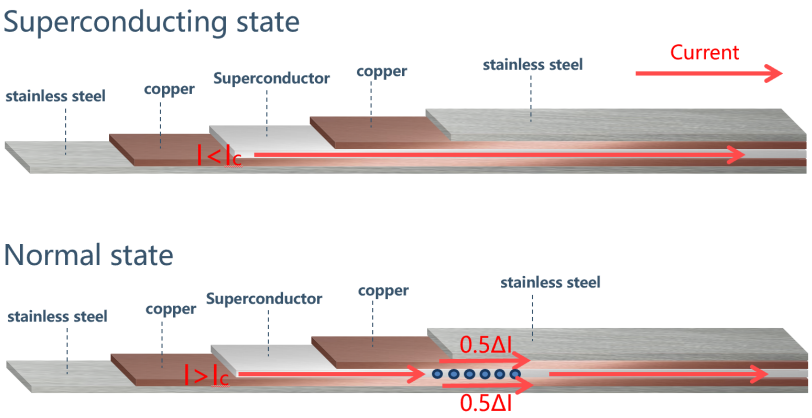

Fig. 4.13 Schematic drawing of 2G coated conductor in the superconducting state and in the normal state.

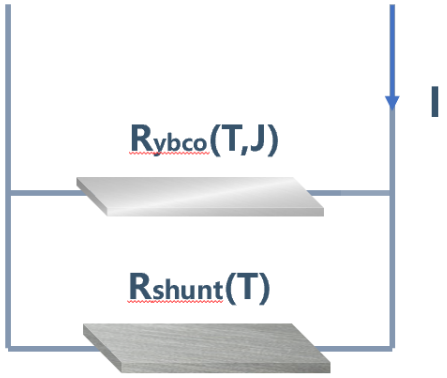

Fig. 4.14 Equivalent electrical circuit of the coated conductor, where R_{ybco} is the resistance of the superconducting layer, and R_{shunt} is the equivalent resistance of the shunt layers.

Without considering the temperature rise, the V-I curve of the superconductor follows the E-J power law, and the V-I curve of the shunt layers is independent of the current. However, the actual V-I curve of the superconductor is shifted by temperature, and the resistivity of the metals in the shunt is positively related to temperature, as shown in Fig. 4.15.

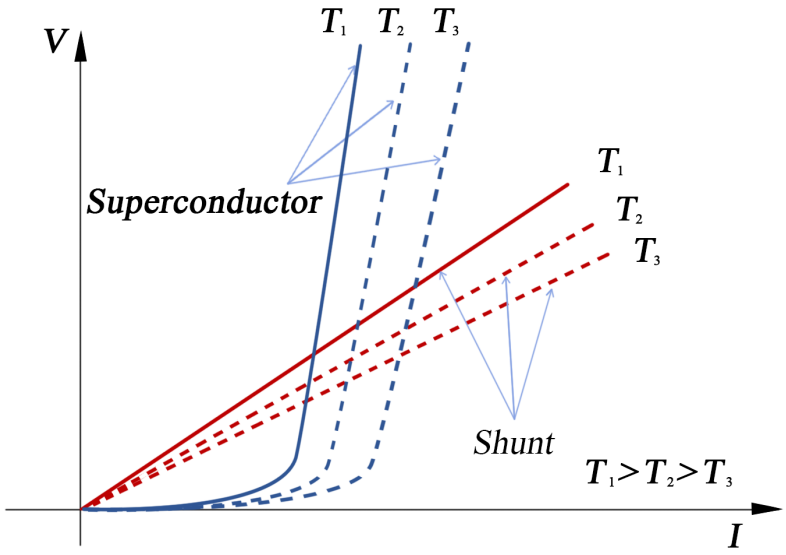

Fig. 4.15 Schematic drawing of the V-I curve of the YBCO layer and shunt layers.

There are three main parameters to determine the response of the tapes to the pulse over-current: critical current, room temperature, resistance, and mass. The following will give a qualitative analysis of the influence of these three parameters on the previous experimental result, by combining the electrical circuit, and thermodynamics.

According to the first law of thermodynamics, the energy generated within the tape plus the net rate of heat flow into the tape volume should be equal to the thermal energy increase in the tape:

$$i^2R - \nabla \cdot (k\nabla T) = \rho C_p \frac{\partial T}{\alpha t} \tag{4.2.1}$$

where i^2R is the power generation in the tape, R represents the total resistance of the tape considering the superconducting layer and parallel layers, T is the temperature of the tape, k is the thermal conductivity, ρ is the mass density of the tape, and C_p is the heat capacity of the tape.

To simplify the analysis, the following assumptions are made:

1) The temperature inside the coated conductor is homogeneous, and there is no temperature gradient between different layers.

2) The tape is in good contact with the LN, and boiling of LN is neglected, so that the ambient temperature is assumed to be 77 K.

3) Heat only transfers to LN from the wide surfaces of the coated conductor, so that the difference in the thickness of the coated conductors does not affect heat transfer.

4) Superconductors that have the same critical current at 77 K also have the same V-I curve under all temperatures.

Analysis for the result in 4.2.2.1

In the first experiment, the SSTC 23g tape and 28 g tape had the same critical current, and the R_{shunt} of 23g tape was higher than that of the 28 g tape (at the same temperature). Under the same pulsed over-current, initially the total resistance R_{shunt} //R_{ybco} of the 23 g was higher than the total resistance of the 28 g tape. Therefore the voltage of the 23g tape was higher than that of the 28 g tape. During the same time duration, more Joule heat was generated in the 23 g tape. Considering the thermal resistance of the two tapes was the same, and the mass of the 28 g tape was higher than that of the 23 g tape, the temperature rise of the 23 g tape was higher than that of the 28 g tape, according to Eq. 4.2.1. The temperature rise further increased the resistance of the R_{shunt} and shifted the V-I curve of the superconductor, resulted in a higher increased in the impedance of the 23 g tape.

In the second experiment, although the AMSC 23 g tape had a higher critical current than the SSTC 28 g tape, the difference was too small to compensate for the effect of the higher R_{shunt} and lower mass of the 23 g tape. Therefore the result was similar to the first experiment.

Analysis for the result in 4.2.2.2

In the experiment, SSTC 28g tapes with different critical currents were tested. With the same pulsed over-current value, initially the R_{shunt} //R_{ybco} of the lower I_c tape was higher, simply because R_{ybco} is higher. The higher total resistance generated more Joule heat, and therefore the temperature rise was higher. The greater temperature rise in turn results in higher tape resistance and higher tape voltage.

Analysis for the result in 4.2.2.3

In the test, the critical current of the SSTC 23 g tape was 240 A, which was 50 A less than that of the AMSC 23 g tape. The room temperature resistance of the SSTC 23 g tape was 125 $m\Omega/m$, whereas the resistance of the ASMC tape was 120 $m\Omega/m$. At the beginning of the

pulsed over-current, the voltage of the SSTC 23 g tape was slightly higher than the voltage of the AMSC 23 g tape, which may be mainly attributed to the fact that the critical current of the SSTC 23 g tape was lower. The voltage increase of the AMSC 23 g tape was faster than the 23 g tape, therefore when approaching the end of the pulse, the voltage of the AMSC 23 g tape became even higher. The phenomenon is peculiar, but it could be influenced by heat capacity and the resistance vs temperature of the shunt ($R_{shunt}(T)$). The heat capacity of the shunt layers of the AMSC tape may be lower than that of the SSTC tape, so the temperature increase was faster. At the same time, although the room temperature resistance of the AMSC tape was lower, it is possible that at other temperatures the AMSC tape might have higher resistance. Therefore, the $R_{shunt}(T)$ curve would be a more accurate parameter to predict the behaviour of the pulse over-current response than the room temperature resistance. However, due to the limitation of our equipment, we were unable to measure the $R_{shunt}(T)$ curve, and this could be done in the future.

Chapter 5

Influences of SFCL on AC grid

5.1 SFCL for AC distribution lines

Modern electric power systems have increased in complexity as a result of rapid growth in the demand for power. The increasing scale of the transmission and distribution network places huge mechanical and thermal stresses on the network equipment (lines, transformers, circuit breakers, generators, etc). Additionally, power systems are designed to be more interconnected in order to improve the reliability and resilience. These all result in the increasing fault current levels. Traditional means of fault current limitation include system topology modifications, replacement of equipment, adding transformers, and the use of fault current limiters. Fault current limiters are used to reduce the fault current levels to an acceptable level rather than to suppress the fault current completely. They are efficient solution for short-circuit current problems to both newly installed and existing power grids [82].

Using high temperature superconductors (HTS) for fault current limiters has been intensively investigated [83–86]. Superconducting fault current limiters (SFCL) have a negligible impedance during normal operation and are able to develop a considerably higher resistance within a very short time (less than a quarter of an AC cycle) after a fault occurs, thereby limiting the short-circuit current to a reasonable value [87–89]. Apart from fault current limitation, SFCLs have proved to be useful in improving the transient stability of generators and consequently the stability of networks [90]. Due to its superior characteristics, SFCLs have attracted attention worldwide.

In the event of a short-circuit in an electrical network, a voltage sag in a certain bus bar may appear. It is a temporary and short voltage reduction which affects the operation of equipment such as electronics elements in the grid. A transient recovery voltage (TRV) may also occur in a short-circuit event. TRV is the high frequency voltage that appears across

a circuit breaker after a switching action and is an important consideration for selection of circuit breakers with appropriate ratings.

By inserting a resistive SFCL (R-SFCL) device in series in the system one may protect the system not only against high fault currents, but issues as voltage sag and TRV may be also avoided. Since the resistance of the R-SFCL instantly rises in the event of a fault, an equivalent resistance appears between the voltage at the bus bar and the fault point, thus inhibiting voltage sag at the bus bar. Another important feature of the R-SFCL is its capability to reduce the X/R ratio of a system (where R and X are respectively the resistance and reactance of the system). In an event of short-circuit, the resistance of the R-SFCL resistance rapidly increases, reducing the X/R ratio. The symmetrical waveform of the limited current may avoid damaging circuit breakers. The resistive properties of such devices are also desirable in order to prevent damages to the CB caused by transient recovery voltage.

5.2 Considered distribution grid

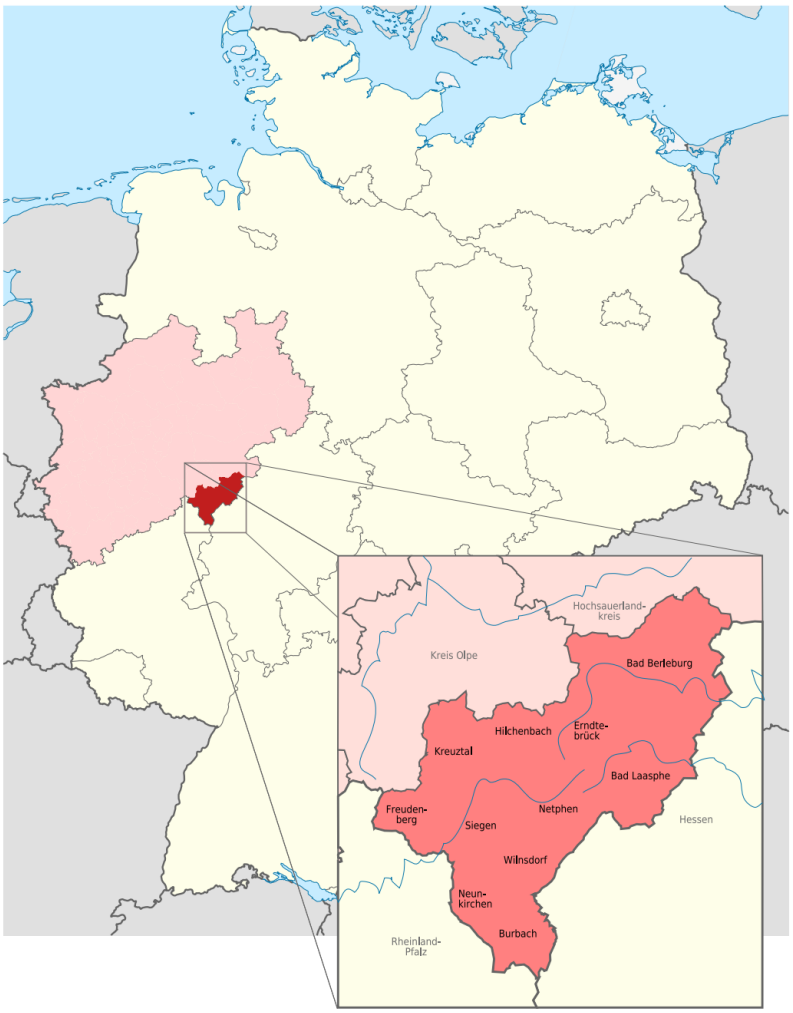

Fig. 5.1 District of Siegen-Wittgenstein.

The studied network is located in the district of Siegen-Wittgenstein. Fig. 5.1 is the geographical map for the distribution system. As shown in Fig. 5.2-5.3, the power flows from the high voltage to the low voltage. There are six power substations: Amprion, Bad Berleburg, Berghausen, Erndtebrück, Feudingen, and Bad Laasphe, which supply the power for the load located in the district of Siegen-Wittgenstein. The following section presents the detailed equipment and topology in each power substation.

The power source to the distribution network is 380 kV Amprion substation. At the 380 kV Amprion substation, there are two 380 kV/110 kV transformers to supply the power to 110 kV bus. One transformer capacity is 150 MVA and the other 300 MVA. From the

110 kV bus, two 110 kV lines of length 20.7 km each are radiated to the 110 kV bus in the Berghausen substation.

At the 110 kV Berghausen substation, there are three voltage levels: 110 kV, 30 kV and 10 kV. From the 110 kV bus in the Berghausen substation, two lines are connected to two different substations and two 110 kV/30 kV transformers. One line is to the Bad Berleburg substation with length of 6.4 km. The other line is 19.3 km long and leads to the Bad Laasphe substation. Two 110 kV/30 kV transformers have a capacity of 31.5 MVA each to supply the power to the 30 kV bus. From the 30 kV bus, two feeders and two 30 kV/10 kV transformers are supplied. One 30 kV line is connected to 30 kV Erndtebrück substation of length 8.2 km. The other line is to a 35 kV bus 5.9 kM away from the Berghausen substation. Two 30 kV/10 kV transformers with the capacity of 16 MVA each supply the power to 17.5 MVA load located at the 10 kV side.

In the 110 kV Bad Berleburg substation, two 110 kV/10 kV transformers are installed to supply the power to a 17.4 MVA load at the 10 kV side. One transformer has a capacity of 40 MVA, and the other 31.5 MVA.

At the 110 kV Bad Laasphe substation, there are the same three voltage levels as at the Berghausen substation: 110 kV, 30 kV and 10 kV. The 110 kV bus is supplied by the 110 kV line from the Berghausen substation. The 30 kV bus is supplied by the 30 kV line of length 12.8 km from the bus 5.9 km away from Berghausen substation and is connected to the 30 kV bus at the Feudingen substation by an 8.5 km line. The 10 kV bus is supplied by one 110 kV/10 kV transformer with capacity 40 MVA, and two 30 kV/10 kV transformers with the capacity 16 MVA and 6.3 MVA respectively. An 18.5 MVA load is connected to the 10 kV bus.

At the 30 kV Erndtebrück substation, the 30 kV bus is linked to three lines. The first line is from the Berghausen substation of length 8.2 km. The second line is from the bus 5.9 km away from the Berghausen substation of length 1.7 km. The third line is from the Feudingen substation with the length of 8.3 km. The 30 kV bus supplies four 30 kV/10 kV transformers, of which two transformers have the capacity of 16 MVA each and two transformers have the capacity of 6.3 MVA each. The four transformers supply the power to the 10 kV bus with 17.8 MVA load.

At the 30 kV Feudingen substation, the 30 kV bus is supplied by two lines. One line is from the Bad Laasphe substation of length 8.5 km. The other line is from the Erndtebrück substation of length 8.3 km. Two 30 kV/10 kV transformers of capacity of 10 MVA each are installed to supply the power to a 10 kV bus with 4.5 MVA load.

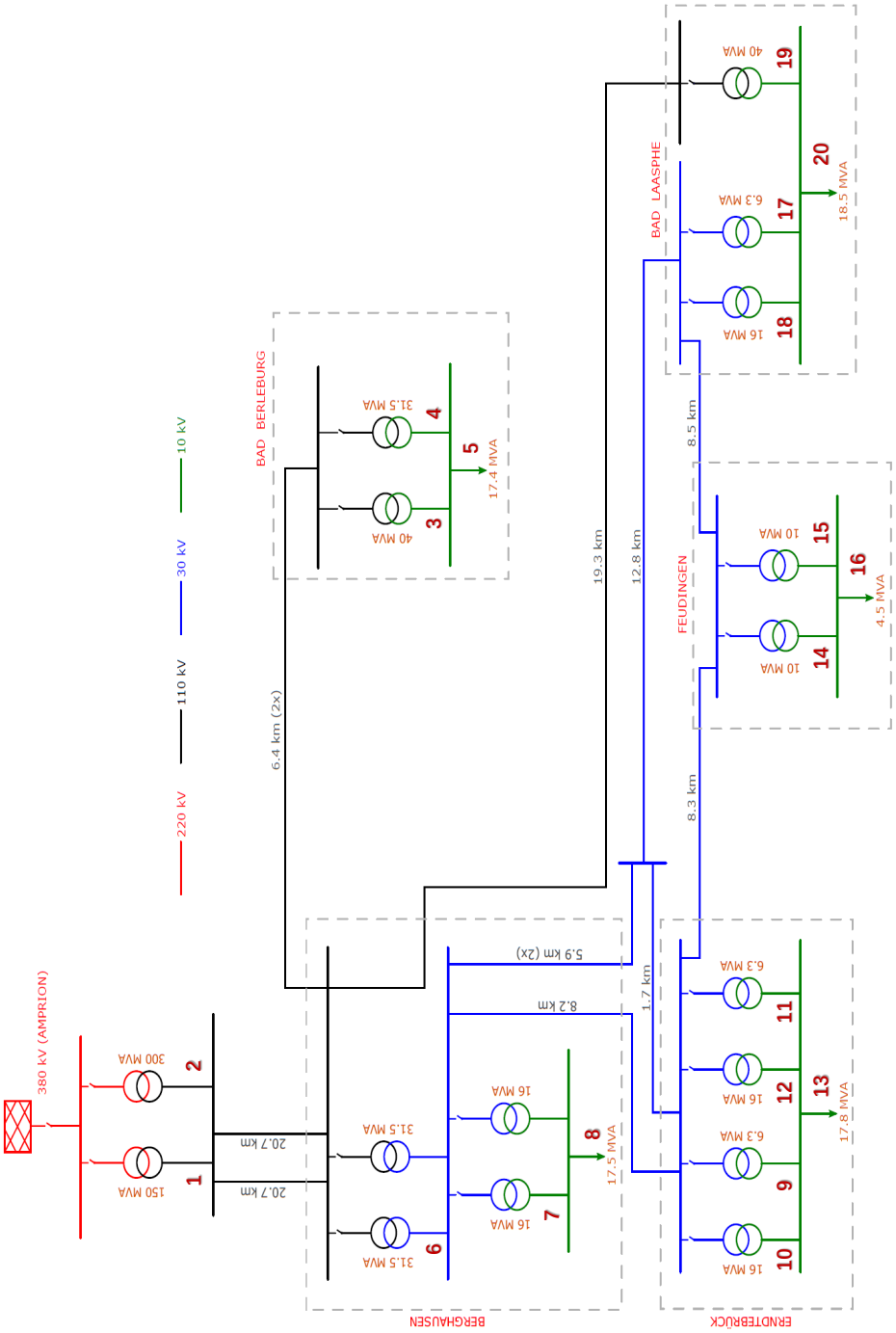

Fig. 5.2 Distribution network of Siegen-Wittgenstein District with 20 location number denoted.

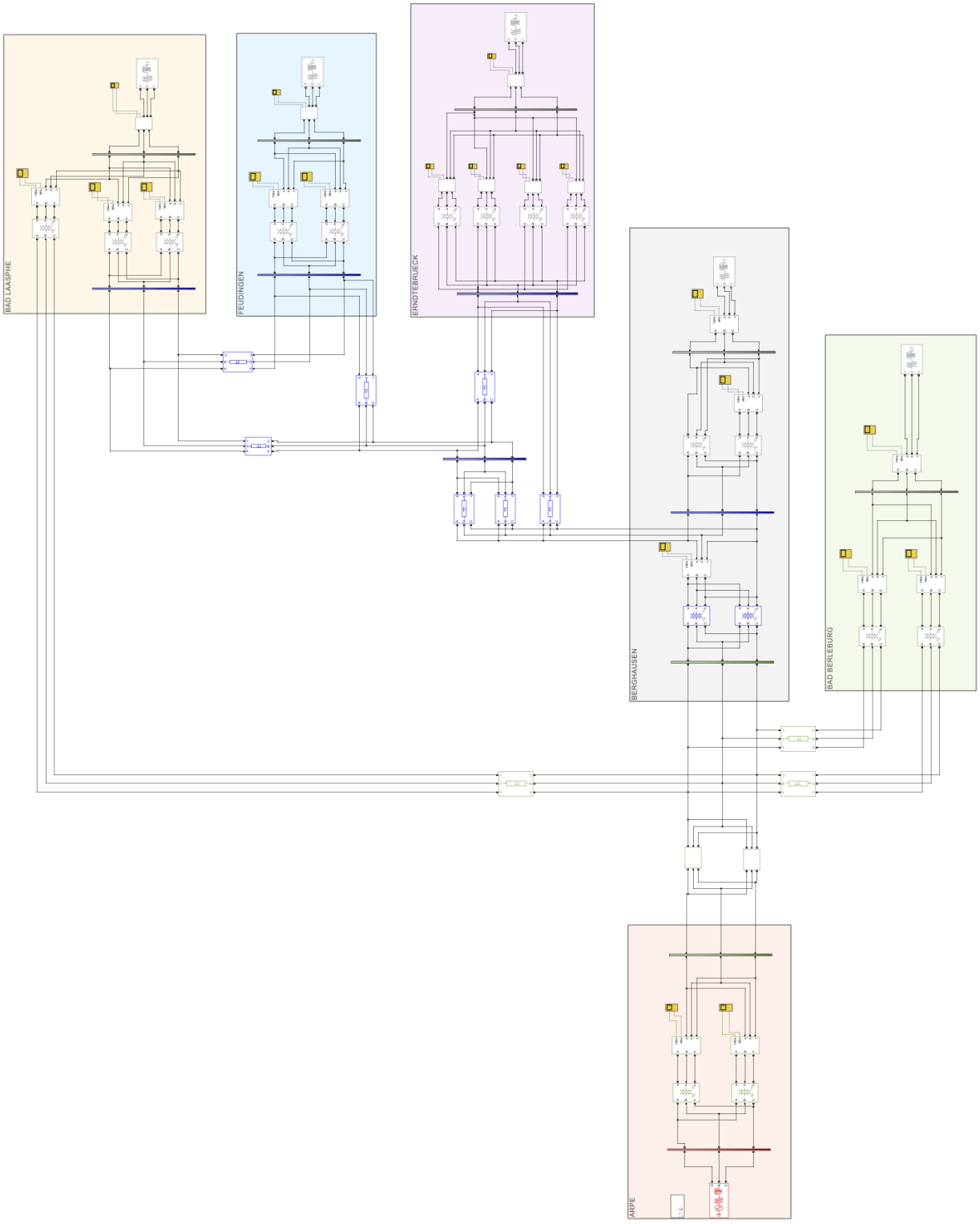

Fig. 5.3 Matlab simulink model of Siegen-Wittgenstein District distribution network.

In the following section, the author aims to investigate cases of different types of short-circuited faults occurring at 5 different locations of the network, thus trying to find out the most severe fault situations and the best place for installing superconducting fault current limiters.

5.2.1 Study on the faulted grid

Analysis of fault current level of different fault locations

This section aims to locate the place where a short-circuit fault will incur the highest fault current. Because a single-phase-to-ground fault is the most common fault type, in the simulation it is assumed that all the faults are single-phase-to-ground faults, and only a phase A to ground (AG) fault is investigated. Each time, a fault is staged at the load side of one of the above mentioned five communities. During each fault, the peak fault current values at twenty different positions in the grid are monitored (the position numbers are denoted in Fig. 5.2). The corresponding results are illustrated in Fig. 5.4-5.8.

Case 1. Fault occurs at Bad Berleburg

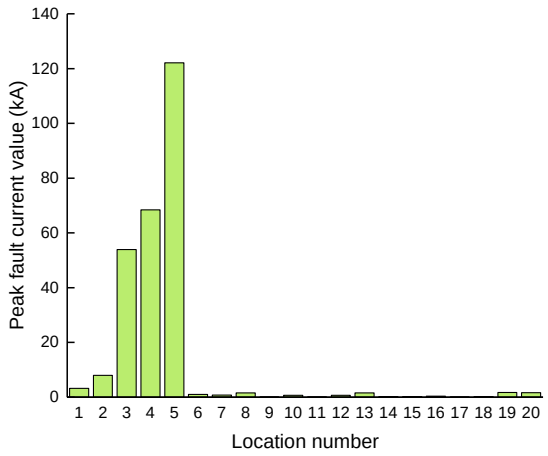

Fig. 5.4 Peak fault current values at different locations on the network.

According to Fig. 5.4, when a single-phase-to-ground fault occurs at the load side of Bad Berleburg (location No.5), the fault current can reach 122.1 kA at the same location. Meanwhile at locations No.4 and No.3 the fault currents are 68.4 kA and 54.9 kA, respectively. These extremely high fault currents are severe threats to the safety and reliabilty of the grid and must be reduced by fault limitation apparatus.

Case 2. Fault occurs at Berghausen

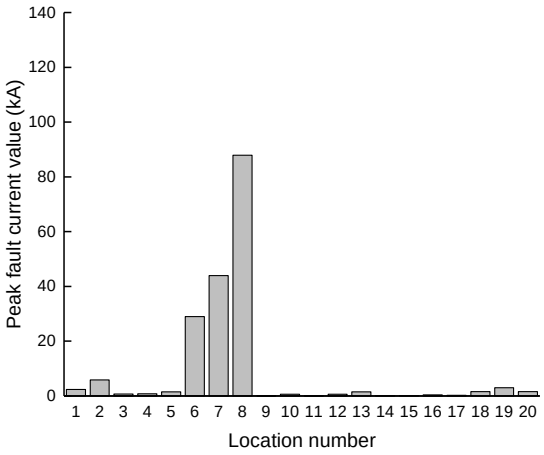

Fig. 5.5 Peak fault current values at different locations on the network.

When a single phase to ground fault occurs at the load side of Berghausen (location No.8), the fault currents occurring at locations No.8, No.7 and No.6 are noticeably larger than that at other places (with fault current values of 87.9 kA, 43.9 kA, and 29.0 kA respectively).

Case 3. Fault occurs at Erndtebrück

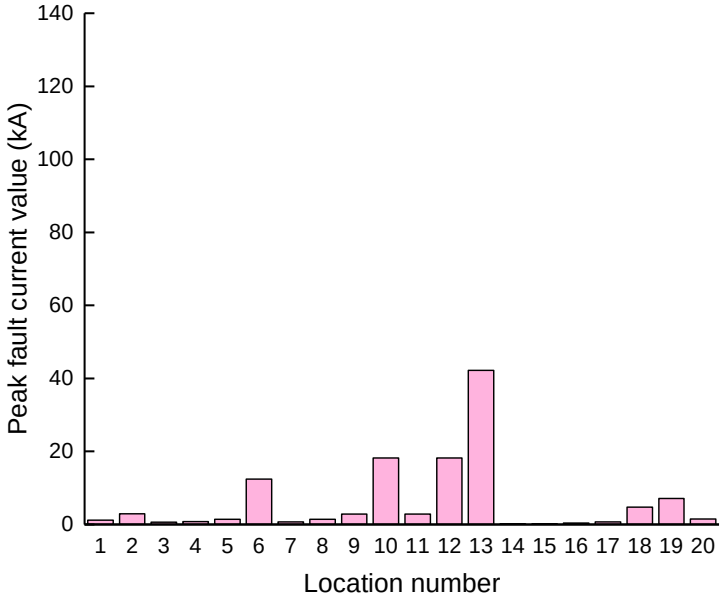

Fig. 5.6 Peak fault current values at different locations on the network.

When a single phase to ground fault occurs at the load side of Erndtebrück (location No.13), the largest fault current occurs at location No.13 with the value of 42.2 kA. At this current level, the faulted line can be easily isolated by circuit breakers.

Case 4. Fault occurs at Feudingen

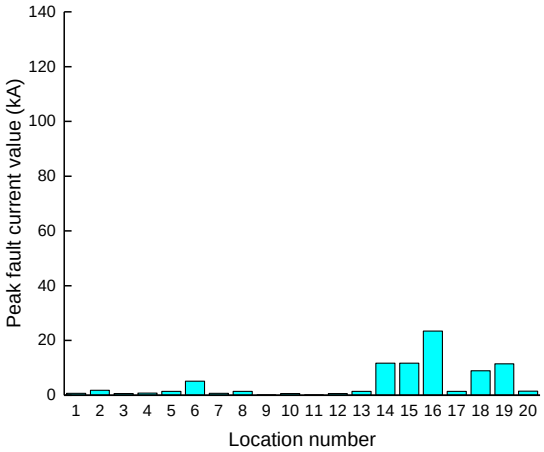

Fig. 5.7 Peak fault current values at different locations on the network.

It can be seen from Fig. 5.7, the occurence of a single phase to ground fault has the least impact on the grid if it happens at the load side of Feudingen (location No.16) as the largest fault current is only 23.5 kA.

Case 5. Fault occurs at Bad Laasphe

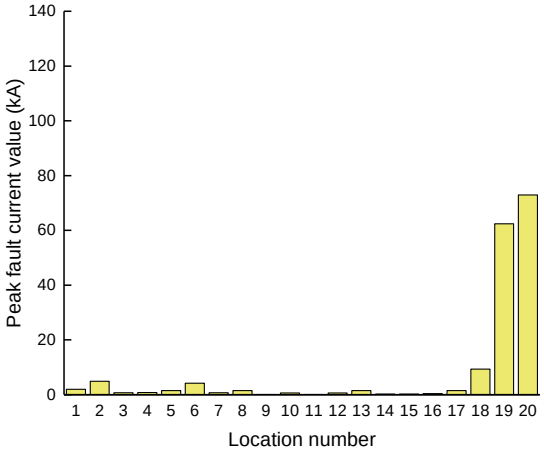

Fig. 5.8 Peak fault current values at different locations on the network.

When a single-phase-to-ground fault occurs at load side of Erndtebrück (location No.13), the fault currents occurring at locations No.8, No.20 and No.19 are noticeably larger than that at other places (with fault current values of 72.9 kA and 62.4 kA, respectively).

From the above results, it is clear to see when a single phase to ground fault occurs at the load at Bad Laasphe (location No.5), the fault current level is the highest (122.18 kA), and far exceeds the switch capacity of the equipment circuit breaker in the electrical network. Such tremendous fault current may result in permanent damages or destruction of the circuit breakers, transmission lines, or even the transformers. It may also threaten the stability of the 30 kV and 110 kV power systems.

There are several ways to reduce the fault current level. One is to operate the transformers at the Bad Laasphe load side separately, but in this case the reliability is affected for the consumers. Another is to install air core reactors in the 30 kV, 100 kV or the 10 kV system. However, such a solution would result in power loss as well as an increase in voltage drop during normal operation. In this work, the author proposes the use of a SFCL device to limit the fault current. In order to reduce the fault current level of the system, to improve the voltage quality at the load, and to improve the TRV over the circuit breaker terminals,

an R-SFCL device is designed for installation at location 5. The circuit breaker CB was simulated as an ideal switch.

5.3 Design and modeling of the superconducting fault current limiter for the studied grid

5.3.1 Working principle of resistive SFCL

As illustrated in chapter two, superconducting fault current limiters are usually categorized according to their designs and working principles into several types: resistive, bridge type, shielded core, and saturated core SFCL [88, 12]. The resistive type SFCL is the simplest one in design and structure [91]. Its working principle is based on superconductors' quench process, which is a rapid increase in resistance when current levels are above the critical current values I_c of the material [92]. References [93, 87] show the projects of commercial resistive SFCLs installed in the grid.

The R-SFCL is connected in series with the electrical circuit to be protected, as shown in Fig. 5.9a. Fig. 5.9b is a schematic of a resistive type SFCL which consists of 25 coils connected in series. Each coil is composed of superconducting YBCO tapes (critical temperature $T_c = 92$ K), as shown in Fig. 5.9c , and a shunt resistor R_{shunt} in parallel that made of stainless steel. During normal operation, the resistance of the superconducting layer is zero. The superconducting layer carries the entire operating current and voltage drop is zero. When a fault occurs, the superconductor transitions automatically to normal state in a fraction of a cycle.

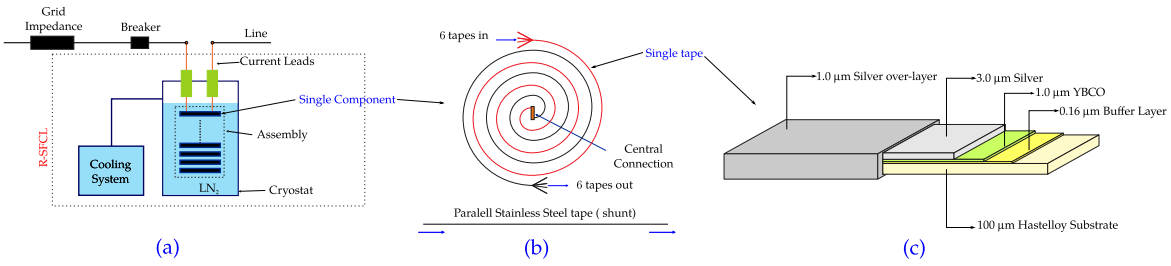

Fig. 5.9 A schematic of a resistive type SFCL.

To minimize inductance, each coil consists of six YBCO tapes in an anti-parallel arrangement (non-inductive bifilar winding) (Fig. 5.9b). The I_c of each tape is about 300 A, so the critical current I_c of the device is 1.8 kA. In each module, all tapes are connected in a common center contact so that these tapes can better protect each other in the case of hot spots. The 25 modules are supposed to be cooled in liquid nitrogen (LN_2) at 77 K.

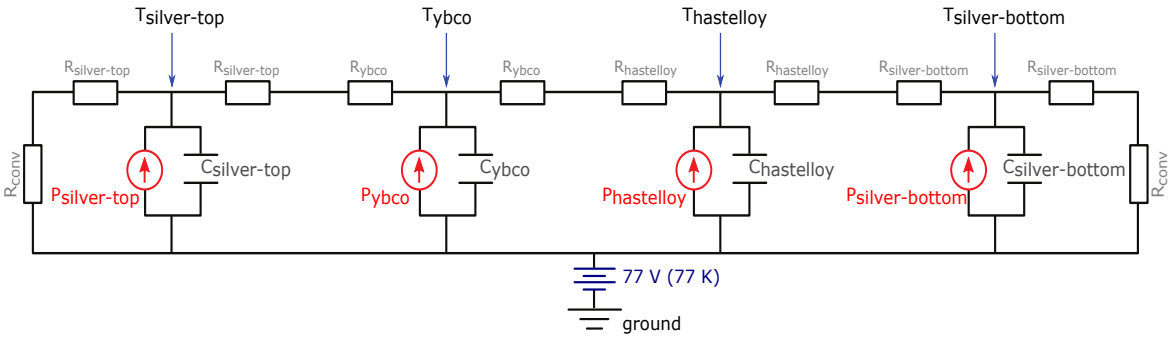

Fig. 5.10 Thermal-electric analogy used to simulate the HTS tapes. The electrical circuit reproduces the heat exchanges in the HTS tape illustrated in Fig. 5.9c.

As described in chapter 2, the transition from a superconducting state to a normal state can be described as a power law divided into three stages: flux creep, flux flow, and normal state [92, 94]. In the simulation, the n value for the first stage (“flux-creep”) is approximately 30; for the second stage (“flux-flow”), $n = 4$; and in the last stage ("normal state"), $n = 1$ [94].

Table 5.1 shows the parameters of the r-SFCL in the simulation.

Table 5.1 SFCL Parameters

Parameters	Value
Tape length	8.6 m (each)
Critical current I_c @ 77 K	1.8 kA
Contact resistance	3 $\mu\Omega$

5.3.2 Simulation model

To accurately simulate the transient electrical and thermal behaviors of HTS tapes, it is necessary to calculate the heat exchanges between different layers of the tapes. Basically the SFCL devices are modeled as variable nonlinear resistances, whose magnitude depends on the temperature of the superconducting layer [95]. A thermal electrical analogy [96–99] is used to solve the heat conduction differential equations inside the HTS layers of SFCLs. According to [100, 101], a network composed of T sections can be used to represent the thermal model. Fig. 5.10 shows an equivalent network that describes the thermal behavior of the R-SFCL component.

The thermal resistances $R_{material}$ are related to the heat conduction of the material, and the capacitors $C_{material}$ are related to the thermal capacity of the material. Equations (5.3.1),

(5.3.2), (5.3.3), and (5.3.4) show the conversion from thermal to electrical quantities. The index i refers to the respective indexed layer. The thermal resistance R_{conv} is calculated as presented in (5.3.4), considering h_c as 0.2 W/cm^{2}K.

$$R_i = \frac{l_i}{\lambda S} \tag{5.3.1}$$

$$C_i = d_i c_i l_i S \tag{5.3.2}$$

$$P_i = I_i^2 R_{e,i} \tag{5.3.3}$$

$$R_{conv} = \frac{1}{(h_c S)} \tag{5.3.4}$$

The physical parameters l_i, c_i, d_i, λ, S, and h_c are, respectively, layer depth, specific heat, specific mass, thermal conductivity, contact surface between layers, and convective heat transfer. The quantity P_i is the heat dissipated in each layer, which is a function of the current in each layer, I_i, and the resistance of each layer, $R_{e,i}$. A comprehensive description about this method can be found in [12, 95]. The resistance of the YBCO layer is a strong function of temperature and current and it is obtained by E-J curve of the material. It is assumed that all tapes to be homogeneous, i.e., all tapes present the same critical current ($I_c = 300$ A) along the whole tape length. The resistivity of normal conductors (further layers) is linearly dependent on the temperature [102]. A detailed flowchart of the simulation algorithm is available in [12, 98].

5.3.3 Comparison of current and voltage behaviour in the faulted grid with and without SFCL for four types of faults

Despite the fact that the single-phase-to-ground fault is the most common failure in the grid, the other three types (phase-to-phase fault, double-phase-to-ground fault, three-phases fault) of short circuits also constitute 25%-30% of the total fault types and can lead to more severe consequences than the AG fault. Each fault type has a unique current and voltage characteristic and will be fully elaborated in this section.

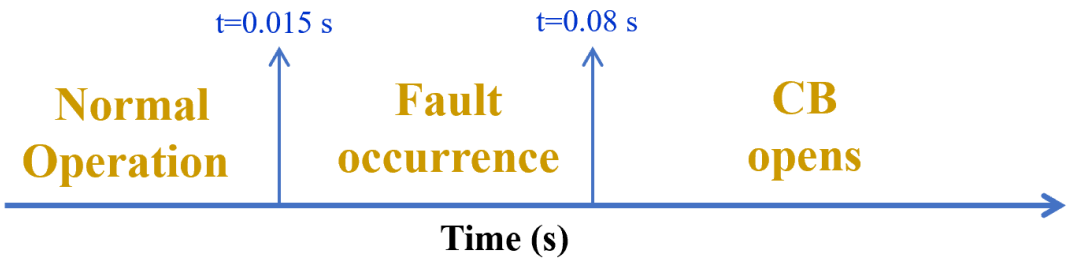

Fig. 5.11 Sequence of events occurring to the grid.

In the following simulation, the sequence of the events is staged as illustrated in Fig. 5.11. The time t=0 is chosen as the moment when the phase angle of phase A voltage is zero. At time t=0.015 s, the fault is initialed, when the phase A voltage reaches the negative peak. The fault lasts for 0.065 s before it is cleared by tripping the circuit breaker.

A single-phase-to-ground fault (AG), double-phase fault (BC), double-phase-to-ground fault (BCG), and three-phase fault (ABC) at location No.5 were simulated. All the faults were assumed to be metallic, which means that the resistance at the fault point was zero.

The designed SFCL device was installed in the grid and its influence on the aforementioned AC transmission grid was observed.

Case 1: Grid with SFCL installed for single-phase-to-ground faults

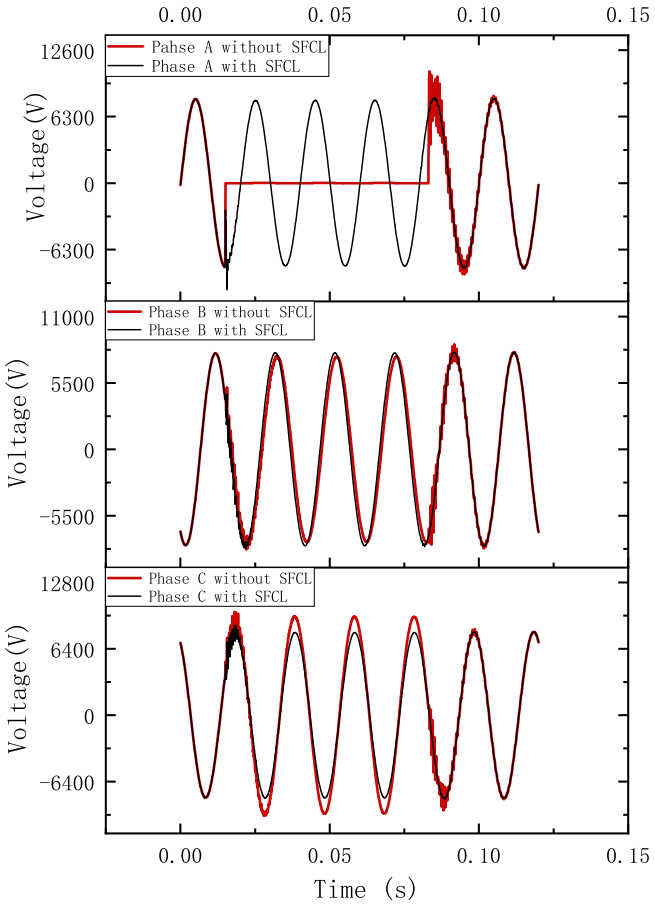

Fig. 5.12 Comparison of voltage waveforms in the faulted grid with and without SFCL.

The black line in Fig. 5.12 shows the voltage behaviour at location No.5 during the sequence of events without SFCL. Under normal operation, the voltage amplititude of all three phases is around 8 kV. When a AG fault occurs, the voltage amplitude of phase A plummets to 1.1 kV, with the other two phases remaining relatively unchanged. When the circuit breaker opens at t=0.08 s, a high oscillation of the voltage is observed, which characterizes the TRV behaviour (detailed in Fig. 5.13)

The red line in Fig. 5.12 shows the voltage waveform at location 5 with the SFCL installed. It is clear from the comparison that the voltage quality at this bar has been improved dramatically by connecting the R-SFCL to the system: the voltage of phase A does not sink to small values during the fault period as in the case of no SFCL in the system. Because of the fast increase of the equivalent resistance of R-SFCL, the voltage level is maintained to its rated value even during the fault, thus avoiding undesirable effects in the

system. Additionally, since the R-SFCLs installed at the other two phases does not activate, they hardly have any influences on these two healthy phases.

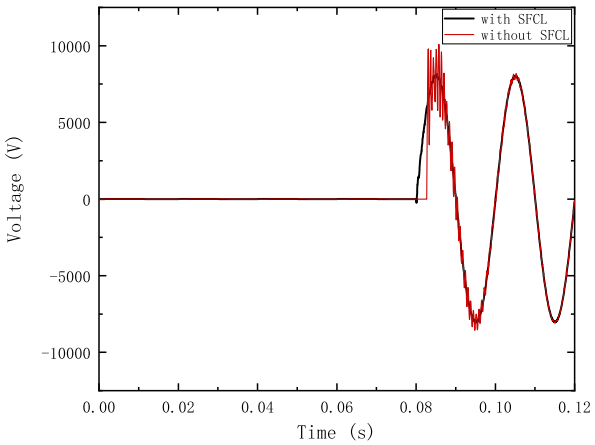

Fig. 5.13 Comparison of voltage waveforms on the circuit breaker in the faulted grid with and without SFCL.

The red line in Fig. 5.13 illustrates the voltage that appears across the circuit breaker after it interrupts current. The transient recovery voltage is of high frequency. Its characteristics, such as rate of rise and amplitude determine if the circuit breaker can successfully interrupt currents. As can be seen, a TRV is imposed across the breaker contacts from t=0.08s.

The smooth black line in Fig. 5.13 indicates the introduction of SFCL can eliminate the high oscillation voltage effectively, compared to the red line.

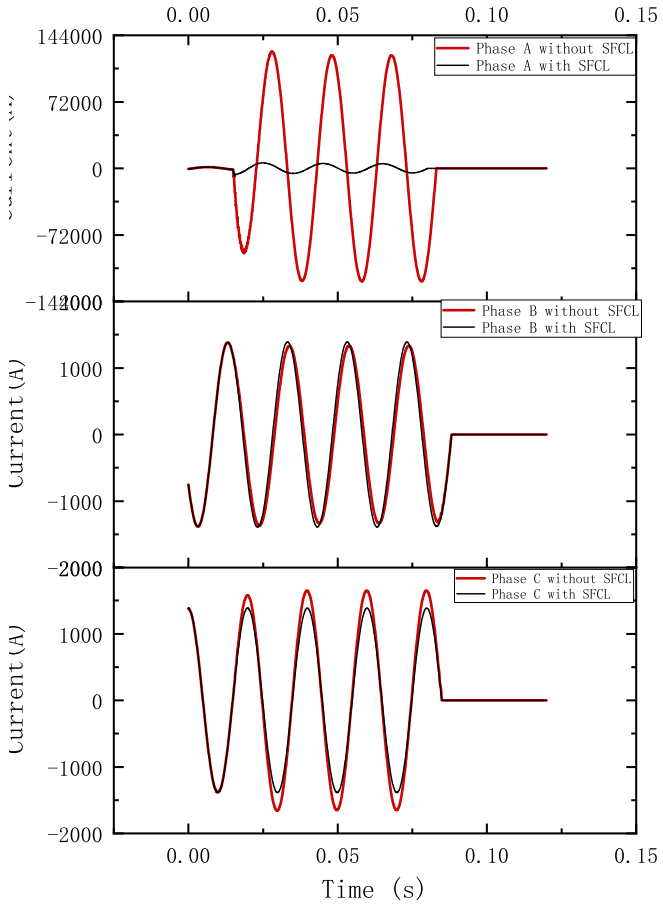

Fig. 5.14 Comparison of current waveforms in the faulted grid with and without SFCL.

The red lines in Fig. 5.14 show the current waveform of a single-phase-to-ground fault (AG) at Location 5. During normal operation, the current aplititudes of all three phases are just 1.4 kA. When a AG fault occurs, however, the current of phase A rockets to 123.5 kA, with the current waveform of the other two phases remaining roughly the same. After the interruption of the CB, the current of phase A goes back to its original value.

The black lines in Fig. 5.14 show the current at location NO.5 in the event of a short-circuit with the R-SFCL inserted in the system, which clearly illustrates an effective limitation from the first half cycle of current. The first current peak of 123.5 kA is limited to 7.56 kA. The subsequent peaks are reduced from 68.3 kA to 5.38 kA. Furthermore, the limited fault current at position No.4 and position No.3 decrease to 4.07 kA and 3.65 kA, respectively from 68.4kA and 53.9kA, respectively.

By further analyzing Fig. 5.12 and 5.14, it can be seen that the R-SFCL has an impact on the system only during the fault period, i.e., before the fault period there is no difference in the current or voltage characteristics despite the existence of the R-SFCL. This can be attributed to the fact that the R-SFCL has no resistance under normal conditions as the YBCO tapes are in the superconducting state.

Fig. 5.15- 5.16 present the behaviour of the equivalent resistance of the R-SFCL, the resistance of the HTS tapes as well as the resistance of the shunt in parallel during the simulated time (indicated in Fig. 5.11). When single-phase-to-ground faults (AG) occur in the system, only phase A is faulted and thus only the SFCL installed at phase A will work. As mentioned, the equivalent resistance of the R-SFCL is negligible before the fault period. During the fault period (between 0.015 s and 0.08 s) the equivalent resistance of the R-SFCL develops to an effective value and thus limits the fault current to an acceptable level.

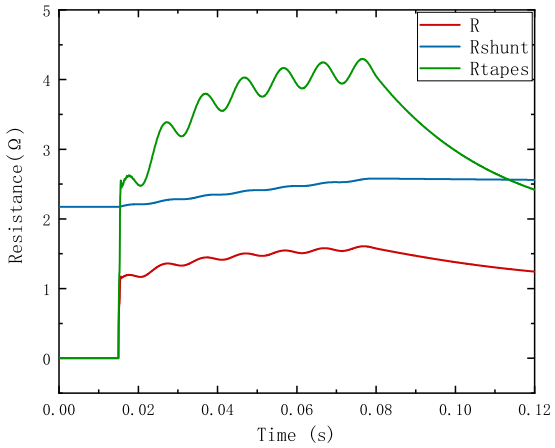

Fig. 5.15 Dynamic behaviour of the equivalent resistance of the R-SFCL, as well as the resistance of the HTS tapes and shunt for the SFCL installed in phase A.

The dynamic behaviour presented by the equivalent resistance R-SFCL can be better understood by analyzing the variation of temperature of the HTS tapes. Fig. 5.17 shows the temperatures of each layer composing the HTS tapes as well as the temperature of the shunt in parallel. A very fast increase of the temperature of the HTS layer can be seen. In a few milliseconds the temperature of the YBCO layer becomes higher than the critical temperature of this superconductor (Tc = 92 K). As already shown, it leads to an increase in the resistance of the HTS tapes during the fault period. Furthermore, the temperature values reached by the HTS tapes and shunt during the fault period indicate that the R-SFCL operates

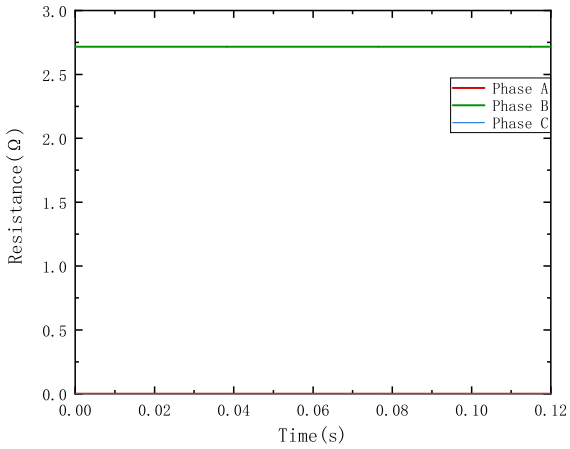

Fig. 5.16 Dynamic behaviour of the equivalent resistance of the R-SFCL, as well as resistance of the HTS tapes and shunt for SFCL installed in phase B or C.

in a safe condition, since the reached values would not be enough to cause damages in such components.

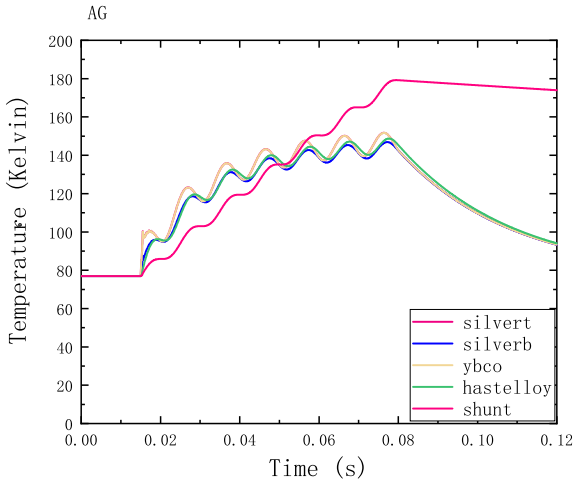

Fig. 5.17 Dynamic behaviour of the temperature of the layers of the HTS tape as well as the temperature of the shunt during the simulated time for the SFCL installed in phase A.

Case 2: Grid with SFCL installed for double-phase faults

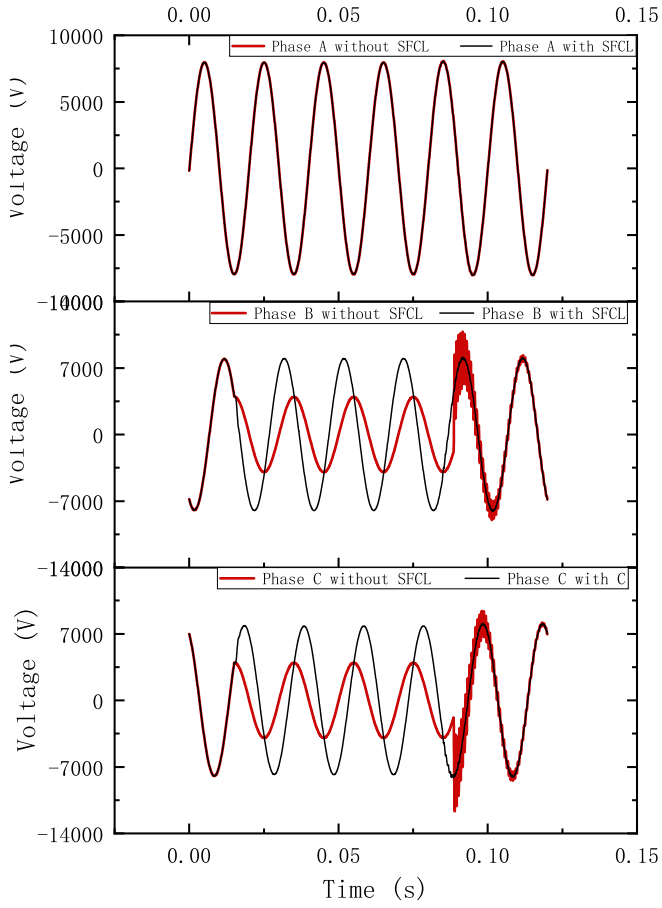

Fig. 5.18 Comparison of voltage waveforms in the faulted grid with and without SFCL.

The red lines in Fig. 5.18 show the voltage waveform at location No.5 during the sequence of events without an SFCL. Under normal operation, the voltage amplitude of all three phases are around 8 kV. When a double-phase fault (BC) occurs, the voltage amplitudes of phases B and C decline to half of their original value, with phase A remaining relatively unchanged. When the circuit breaker opens at t=0.08s, a high oscillation in the voltage is observed.

After the installation of an R-SFCL, the voltage of phases B and C, however, no longer decreases but remains unchanged despite the fault occurring at 0.015 s, as indicated by the black lines.

The transient recovery voltage appearing for phases B and C has also been improved when an SFCL is installed.

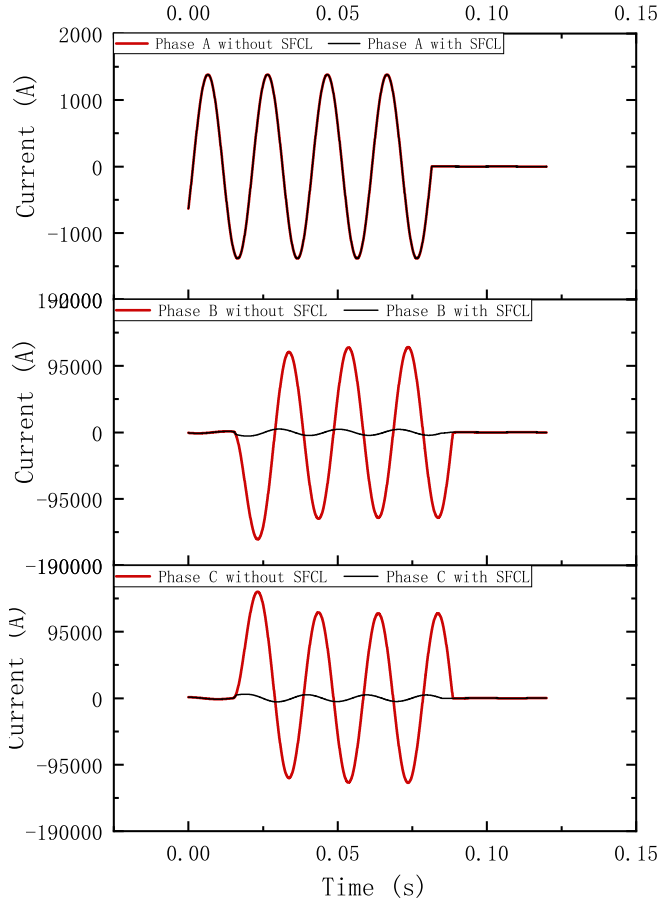

Fig. 5.19 Comparison of current waveforms in the faulted grid with and without SFCL.

The red lines in Fig. 5.19 shows the current waveform of a double-phase fault (BC) at Location 5 without SFCL. During normal operation, the current amplitude of all three phases is just 5.6 kA. When a double-phase fault occurs, however, the currents of phase B and C rocket to 119.8 kA, with the current of phase A remaining roughly the same.

After the installation of an R-SFCL, the currents of phases B and C are limited to 6.4 kA, as indicated by the black lines.

The R-SFCL installed at phase A does not work, so it does not affect this healthy phase at all. The R-SFCLs at phase B and phase C present zero resistance during normal operation and become resistive only during the fault period, which makes the whole device extremely power-efficient.

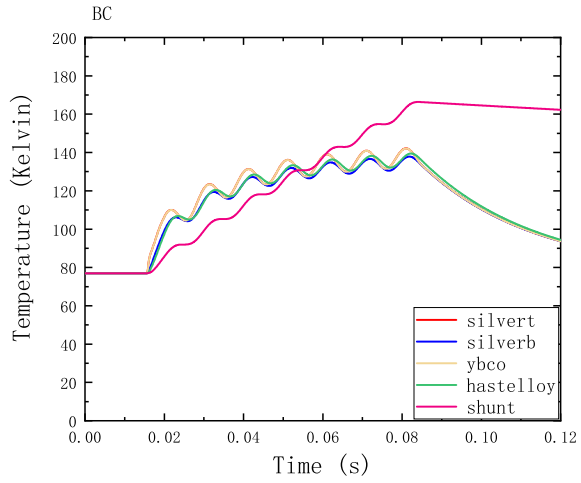

Fig. 5.20 Dynamic behaviour of the temperature of the layers of the HTS tape as well as the temperature of the shunt during the simulated time for an SFCL installed in phases C and B.

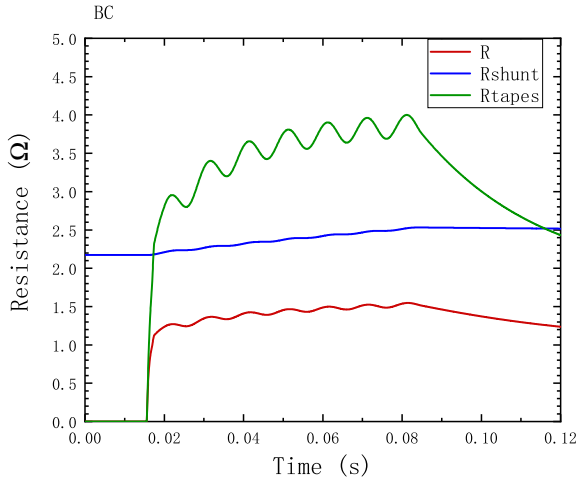

Fig. 5.21 Dynamic behaviour of the equivalent resistance of the R-SFCL, as well as the resistance of the HTS tapes and shunt for an SFCL installed in phases C and B.

Case 3: Grid with SFCL installed for double-phase-to-ground faults

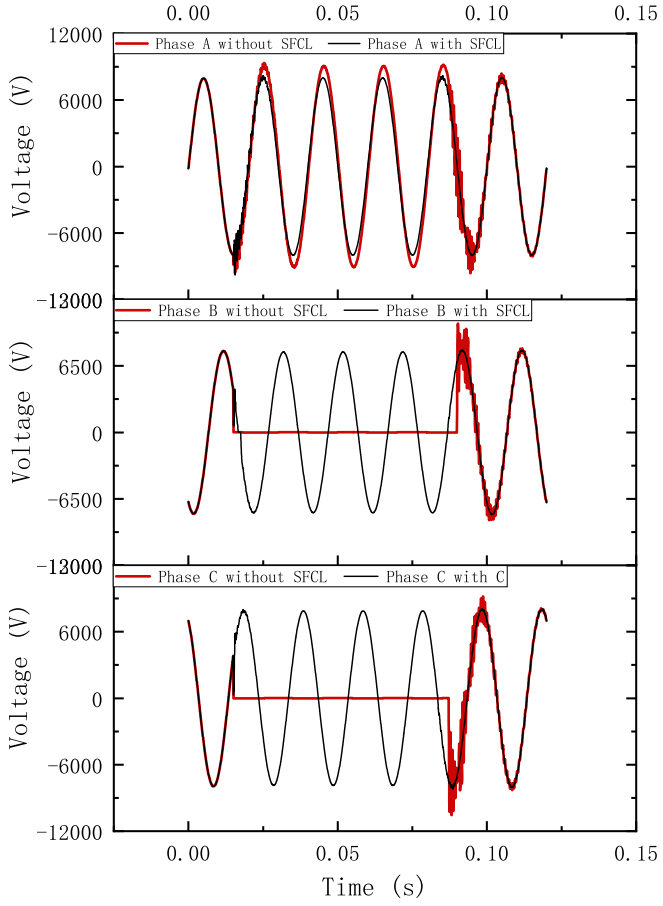

Fig. 5.22 Comparison of voltage waveforms in the faulted grid with and without SFCL.

The red line in Fig. 5.22 shows the voltage behaviour at location No.5 during the sequence of events without SFCL. Under normal operation, the voltage amplitudes of all three phases are around 8 kV. When a double-phase-to-ground fault occurs, the voltage amplitudes of phases B and C decline to an extremely small value, with phase A remaining relatively unchanged. When the circuit breaker opens at t=0.08 s, a high oscillation of voltage across the terminal is observed.

The black line in Fig. 5.22 shows the voltage waveform at location 5 with the SFCL installed. It is clear from the comparison that, when a fault occurs in the system with SFCL, the voltage waveform of the two phases B and C are almost the same before or after a fault. This proves that a SFCL is effective in improving the voltage quality of a short circuit system.

Additionally, since the R-SFCLs installed at phase A does not activate, it hardly affects this healthy phase.

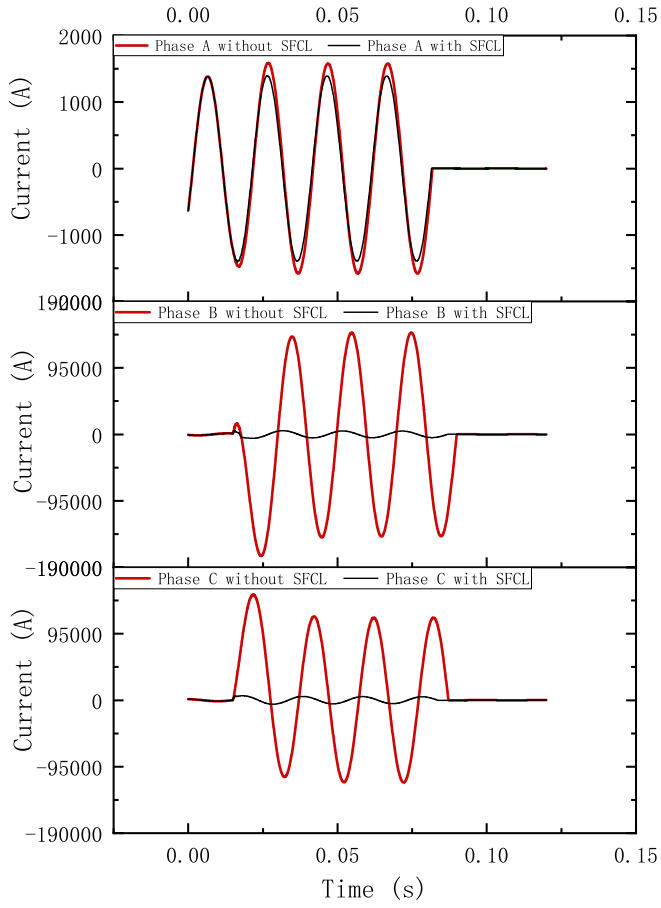

Fig. 5.23 Comparison of current waveforms in the faulted grid with and without SFCL.

Fig. 5.23 shows the current waveform of double-phase-to-ground faults (BCG) at Location 5. During normal operation, the current amplitude of all three phases is just 5.6 kA. When a BCG fault occurs, however, the currents of phases B and C increase to 145.8 kA and 109.8 kA respectively, with the current of phase A remaining roughly the same. The installation of an SFCL has marginal effects on phase A but has dramatically reduced the fault current at phase B and phase C.

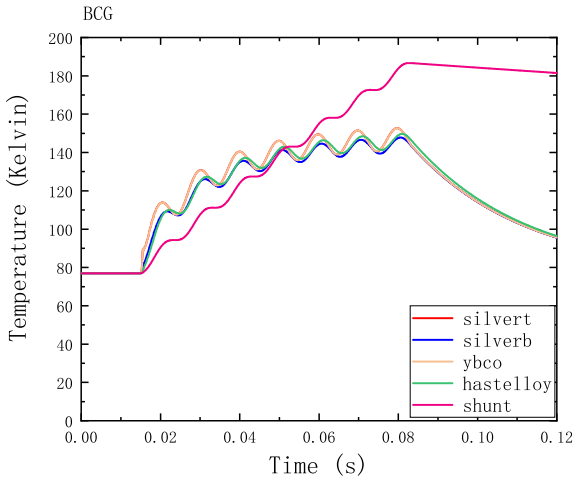

Fig. 5.24 Dynamic behaviour of the temperature of the layers of the HTS tape as well as the temperature of the shunt during the simulated time for an SFCL installed in phases B and C.

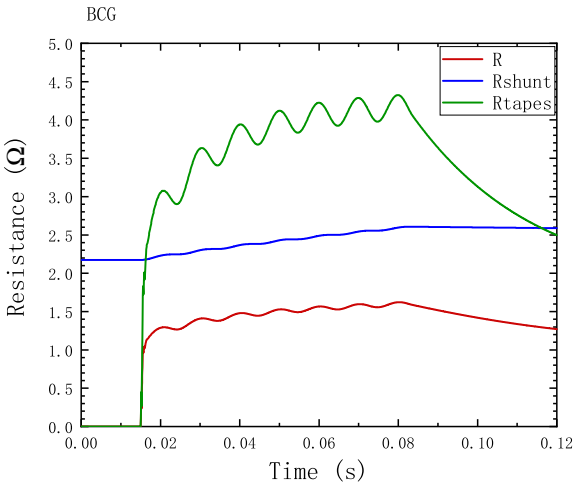

Fig. 5.25 Dynamic behaviour of the equivalent resistance of the R-SFCL, as well as resistance of the HTS tapes and shunt for an SFCL installed in phases C and B.

Fig. 5.24 and 5.25 shows the temperature and resistance of the YBCO model. For a double-phases-to-ground fault, the fault currents in B and C exceed the critical current of the SFCL and thus the SFCLs at these two phases are in operation.

Case 4: Grid with SFCL installed for three-phase faults

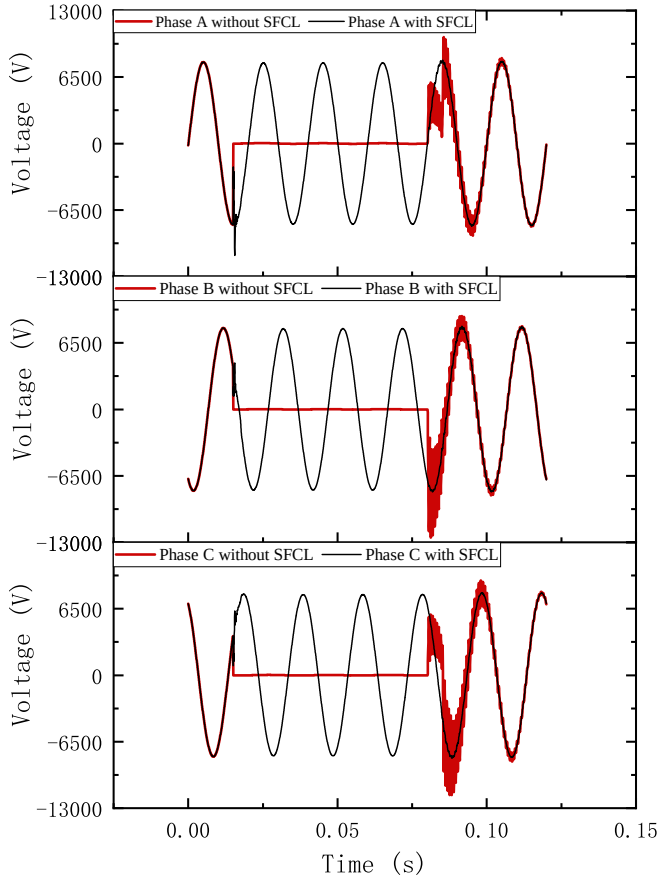

Fig. 5.26 Comparison of voltage waveforms in the faulted grid with and without SFCL.

Fig. 5.26 shows the voltage waveforms at location No.5 during the sequence of events. Under normal operation, the voltage amplitude of all three phases are around 8 kV and they all plummet to an extremely small value. The installation of an SFCL dramatically improves the voltage quality at the three faulted phases. When an ABC fault occurs and the circuit breaker opens at t=0.08 s, a high oscillation of voltage across the terminal is observed. The SFCLs also eliminate these transient recovery voltages successfully.

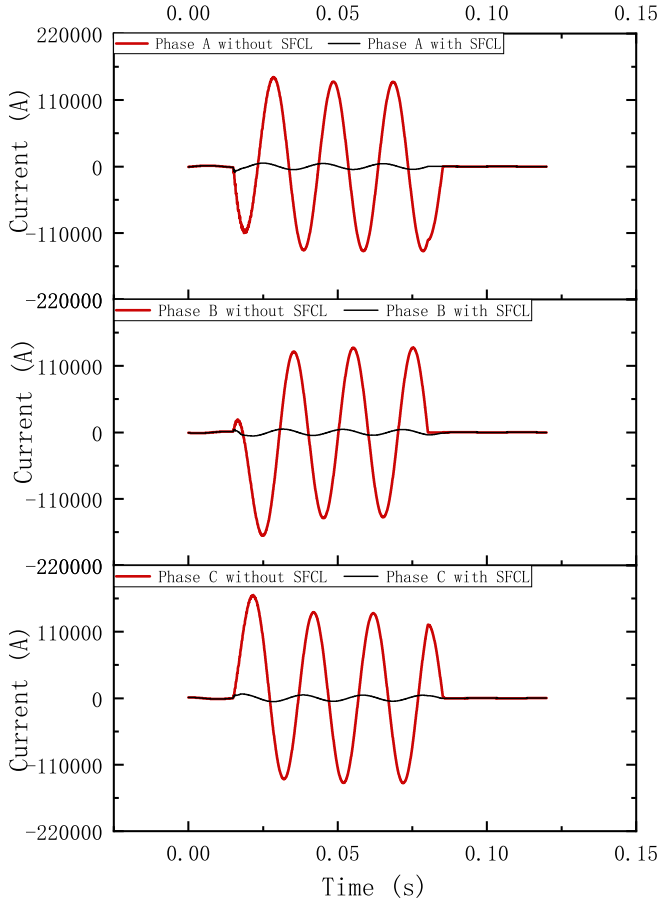

Fig. 5.27 Comparison of current waveforms in the faulted grid with and without SFCL.

Fig. 5.27 shows the current waveform of three-phase faults (ABC) at Location 5. During normal operation, the current amplitudes of all three phases are just 5.6 kA. When an three-phase fault occurs, however, the currents of three phases increase to 140.2 kA (when the fault is stable). The highest peak is as high as 176.06 kA, far beyond any of the other three fault types. When an SFCL is installed, as indicated by the black line, the currents at all three phases are limited to extremely small values.

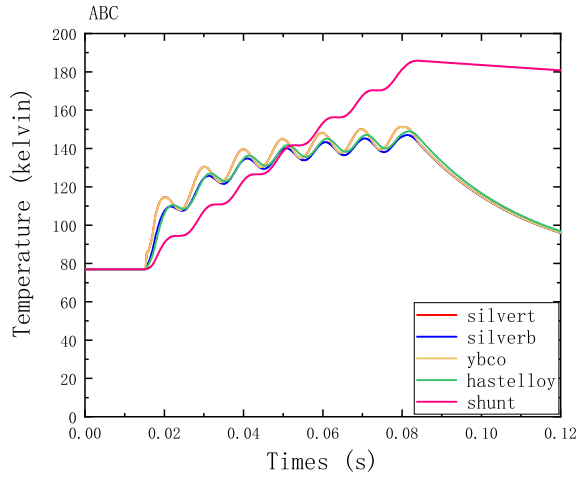

Fig. 5.28 Dynamic behaviour of the temperature of the layers of the HTS tape as well as the temperature of the shunt during the simulated time for an SFCL installed in phases A, B and C.

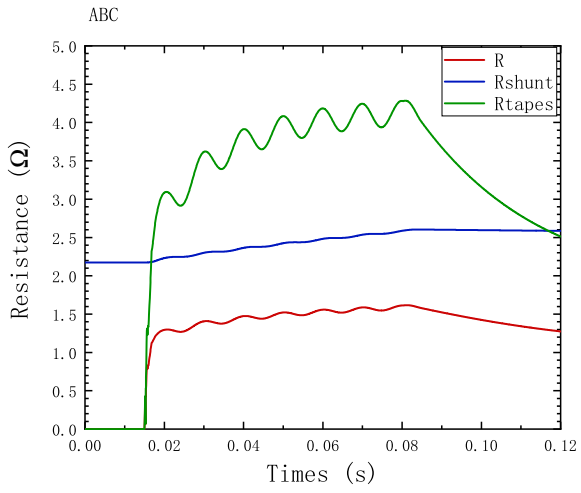

Fig. 5.29 Dynamic behaviour of the equivalent resistance of the R-SFCL, as well as the resistance of the HTS tapes and shunt for an SFCL installed in phases A, B and C.

Fig. 5.28 and 5.29 shows the temperature and resistance of the YBCO model. For a three-phases fault, the fault current in each phase exceeds the critical current of the SFCL and thus the SFCLs at all three phases are in operation.

5.3.4 Conclusions

To sum up, it is clear that an R-SFCL device may be useful not only to protect the system against high levels of fault current, but also to eliminate TRV effects and to improve voltage quality at a certain point in the system. As shown throughout this work, the proposed design of the R-SFCL is enough to provide a suitable reduction in the fault current level of the system. In the example given the temperature of the R-SFCL and its shunt does not rise above 160 K, which is far below the point at which damage to the R-SFCL would occur. The R-SFCL will therefore be able to operate repeatably and reliably and by limiting the fault current and eliminating TRVs protect the rest of the network from damage. Nevertheless, the work done in this chapter can be considered as further development of previous works regarding SFCL devices [103, 104], since we have investigated a real network with a more realistic simulation model.

Because of the fast increase of the equivalent resistance of the R-SFCL, the voltage sag at location No. 5 was contained as well as the TRV at the same bar when the CB opened. Such a feature increases the protection of the considered system, avoiding permanent damage. In addition to that, the TRV over the CB at the moment of opening was also extinguished because of the increase in the equivalent resistance.

Regarding the employed simulation method, the thermo-electrical analogy has proved to be a suitable approach to simulate an R-SFCL in the power grid, providing detailed information about the R-SFCL behaviour, which cannot be accessed by simple models.

Chapter 6

Influences of SFCL on DC grid

6.1 Introduction to HVDC systems

The high voltage direct current (HVDC) electric power transmission technology is for bulk transmission of electricity in the form of direct current, in contrast to alternating current.

HVDC systems are generally categorized into two-terminal HVDC system and multi-terminal HVDC system, the previous type is employed in the majority of real projects. HVDC system can also be classified by its voltage level as high voltage electric power system ($\pm$ 660kV and below) and ultra-high voltage ($\pm$ 800kV and above) electric power system. ABB has successfully developed and tested a 1100 kV UHVDC converter transformer which is expected to transmit 12 GW of electric power over 3000 km distance in China, breaking the record for the highest DC voltage level, largest transmission capacity and longest distance ever achieved [105]. From the view of system topology structure, there are monopole, bipolar, and back to back systems.

Nowadays, despite high voltage three phase alternating-current being the predominant means of power transmission because of its flexible operation and technology maturity, HVDC system is expanding rapidly.

(1) Lower overall cost of power lines

For overhead power lines, the normal three-phase transmission lines need three wires. In contrast, two wires are used in the monopole direct current transmission system and only one wire is needed when the ground or sea is the return circuit. Besides, there is no skin effect for direct current, which enables the maximum utilization of the cross-sectional area of conductors and less power loss. Additionally, the tower structure is simple for HVDC system, and the cable with same insulation level can be used for higher voltage level. Meanwhile the operation expense for direct current lines is lower.

(2) Suitable for long distance power transmission

There are no technical limits to the potential length of a HVDC cable. In a long AC cable transmission, the reactive power flow due to the large cable capacitance will limit the maximum possible transmission distance. Therefore, for very long cable links, HVDC is the only viable technical transmission alternative.

Also, the cost of construction and maintenance of HVDC system is lower than the HVAC system, although the AC substation is much more expensive than the DC conversion station. Therefore for the same power transmission capacity, the longer of transmission distance, the more cost effective HVDC is.

(3) Allow interconnections among unsynchronized networks

Despite of the numerous merits, the AC network interconnections have certain disadvantages such as decreased stability and reliability, large area blackout after a fault, increased fault current level, etc. On the contrast, interconnection via DC grid can avoid these problems and improve the operation performance. Firstly, it allows power transmission between unsynchronized AC distribution systems, which means the connected networks can maintain its own characteristics (frequency and voltage) without being affected by interconnections. Secondly, the power flow through the DC link can be easily controlled and changed. Thirdly, an HVDC transmission does not cause the short circuit current of the interconnected AC system increase, so there is no need to replace existing circuit breaker or other equipment even though their rating is not high.

One main component of the HVDC system is the power converter which converts AC to DC, and DC to AC. Two types of converters are most used in HVDC transmission systems: Line Commutated-Converter (LCC) and Voltage Source Converter (VSC).

Most HVDC systems in operation today employ LCC with thyristor valves, which was first used in 1970's. Half century's developments make this technology mature and robust, it also generates low conversion losses. However, the operation of LCC-HVDC systems consumes reactive power, requires large filters, and may cause commutation failure.

VSC systems, firstly used in 1997 in Sweden by ABB, has been rapidly expending. Voltage Source Converters are based on controllable switches, mainly Insulated Gate Bipolar Transistors (IGBTs). Unlike LCCs, which are mostly used for high power transmission, VSCs are for medium power transmission. Advantages of VSC systems include: (1) They helps the AC grid. (2) No commutation failure. (3) They provide and regulate reactive power.

6.2 Line-commutated converter operation

6.2.1 LCC operating principles

Thyristor switch is the core component of an LCC, as shown in Fig. 6.1. It is a robust, low losses switch, with large voltage blocking capability and current conduction capability, which make it ideal for LCC-HVDC systems. In operation, only when a thyristor is positively biased (anode voltage is larger than cathode voltage) and a small signal is supplied to the gate terminal can the current conduct.

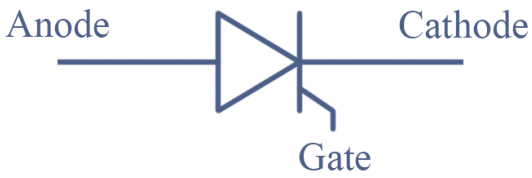

Fig. 6.1 Thyristor switch.

The firing angle, α, is the phase angle of the sinusoidal AC supply voltage when the a thyristor is positively biased and the gate signal is applied, that is to say, a thyristor conducts (or fires). This is shown in Fig.6.2.

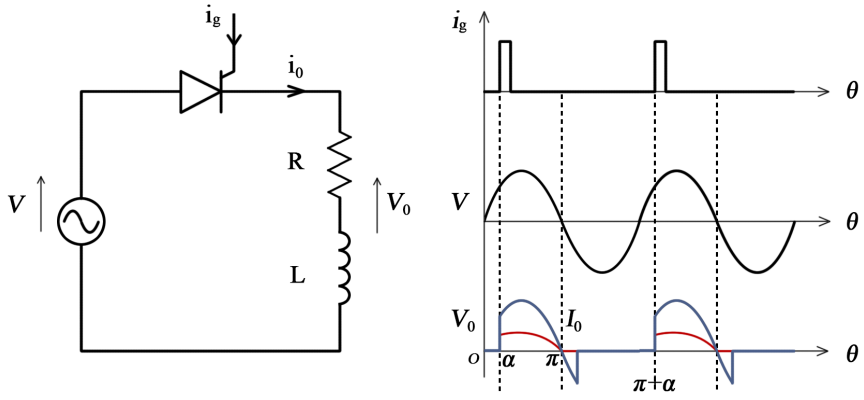

Fig. 6.2 Illustration of firing angle.

The extinction angle, γ, refers to the angle that the internal stored charge produced during its forward conduction time is eliminated. It is also called de-ionization time and is an

important parameter to study commutation failure. A typical value for extinction angle of a valve is 15°.

The basic building block of converters is Graetz bridge, also referred to as six-pulse converter. It consists of six thyristor valves configured as in Fig. 6.3. The numbering of the thyristor valves is also the firing sequence of the thyristors. T_1 is usually fired 60° before T_2; T_2 is fired 60° before T_3, etc.

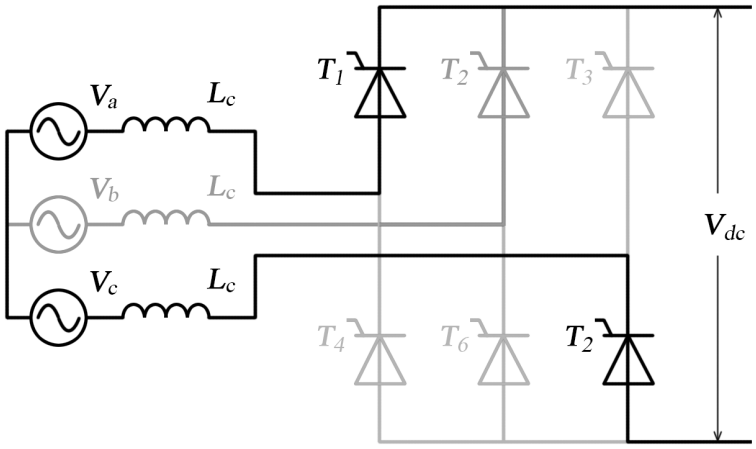

Fig. 6.3 Commutation process in Greatz Bridge.

In proper commutation process, only two thyristor valves conduct simultaneously: one in the top row (T_1, T_3, and T_5) and the other in the bottom row (T_2, T_4, and T_6). These two valves connect two phases of the three-phase AC sources in series with the DC voltage terminals. Therefore, the output of DC voltage momently is the superstition of two phases' voltages of AC source.

As shown in Fig. 6.3, when T_1 and T_2 are conducting, the DC output voltage is:

$$V_{dc} = V_a - V_b \tag{6.2.1}$$

In practice, however, AC sources inevitably contain inductance, the commutation from one thyristor to another do not occur instantaneously. Consequently, there exists a short overlap period when the current transfers from one valves to another in the same row. This duration is called commutation overlap and defined with the overlap angle, μ,

As shown in Fig. 6.4, when T_2 is conducting and T_1 is commutating to T_3, the DC output voltage is:

$$V_{dc} = \frac{V_a + V_b}{2} - V_c \tag{6.2.2}$$

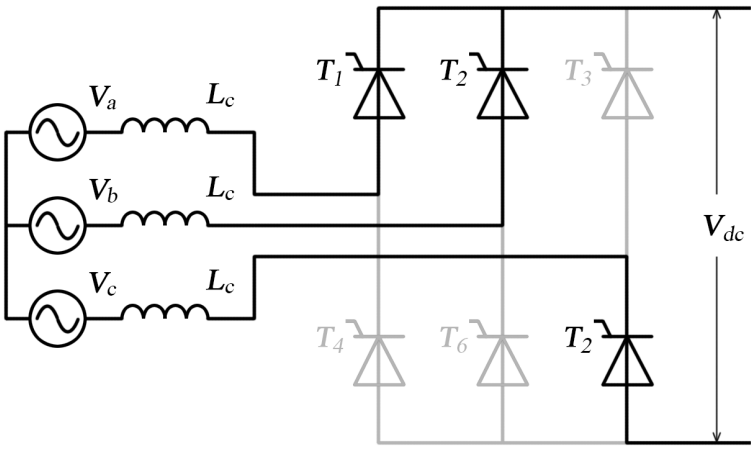

Fig. 6.4 Commutation process in Greatz Bridge.

Equation 6.2.3 shows the average DC voltage value.

$$V_{dc} = \frac{3\sqrt{2}}{\pi} V_{LL} \cos\alpha - \frac{3}{\pi} \omega L_c I_d \tag{6.2.3}$$

where V_{LL} is the line-to-line voltage. α is the firing angle. L_c is the commutation inductance in each phase. I_d is the direct current.

According to the above equation, when the firing angle α increases, the output DC voltage decreases. Therefore it is possible to attain desired DC voltage and transmission power by adjusting the firing angle.

When $\alpha > 90^\circ$, the DC voltage becomes negative and the converter operates in the inverter mode; When $\alpha < 90^\circ$, the DC voltage becomes positive and the converter operates in the rectifier mode, as illustrated in Fig. 6.5.

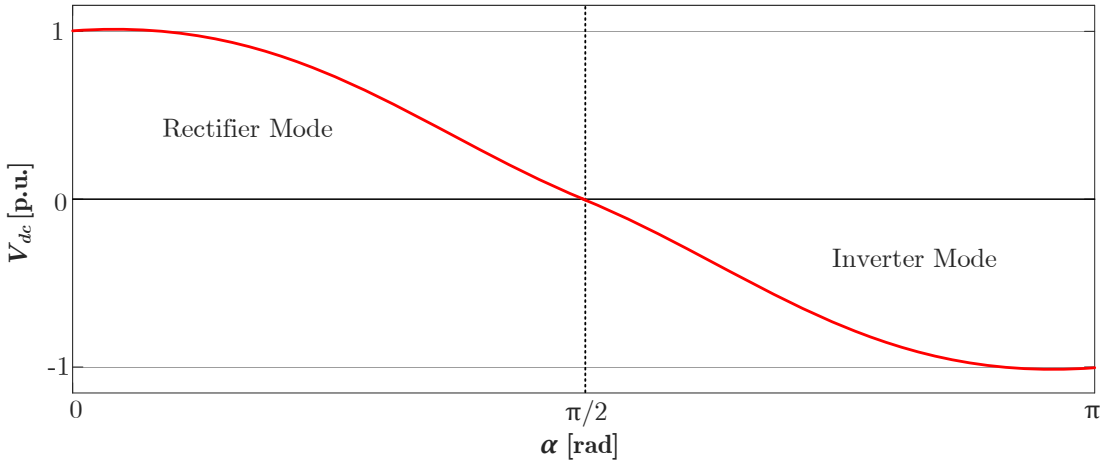

Fig. 6.5 Converter mode as a function of the firing angle α.

The relationship between α, γ and μ is given by (6.2.4).

$$\alpha = 180^{\circ} - (\mu + \gamma) \tag{6.2.4}$$

6.3 Commutation failure in HVDC systems

6.3.1 Commutation failure mechanism

Commutation failure is common fault of inverters in HVDC systems, which are mainly caused by severe voltage dip due to faults at AC side [106]. Consequences of commutation failures include: interruption of transmitted power, thermal and mechanical stress on converter equipment, and malfunction of protective relays [107, 108]. More seriously, repetitive and long-lasting commutation failures can cause shutdown of a link [109].

Commutation failures of inverter's thyristor valves would occur if the extinction angle γ is smaller than the time required for the valve to restore the blocking capability. A thyristor is a semiconductor device having four layers of stacked P and N layers. Power thyristors are required to conduct high current and have high density of free electric charge in P and N layers. When the thyristor is forward conducting and the forward current just reduce to zero, there are still many free electric charge at the junction of P and N. As a result, the thyristor is still able to conduct under the action of the forward voltage between the two poles even without a trigger signal. To prevent this maloperation of thyristor, a reverse voltage should be applied on the valves for a period of time to eliminate the internal stored charge generated by the thyristor during forward conduction and thus to restore the blocking capability of the

forward voltage. This process is called deionization. Therefore, a successful commutation process requires not only time for commutation process (represented by commutation overlap angle μ), but also time for commutation margin (represented by extinction angle γ). The deionization time of each thyristor is fixed, γ_i.

Criterion for successful commutation is:

$$\gamma > \gamma_i \tag{6.3.1}$$

6.3.2 Methods to solve commutation failure

Commutation failures are frequent events and hazardous to power systems, so its prevention methods have been intensively researched accordingly. Those strategies can be roughly categorized into three classifications.

As previously described, enough time for commutation overlap and deionization is necessary to successful commutation. Therefore according to Eq. 6.2.4, in order to increase the sum of μ and γ, a direct solution is to advance the firing angle of inverters once a AC voltage dip is detected by control systems [110]. The drawback of this solution is that most control systems are not quick enough to detect such a disturbance at AC side. For some time instants, this method has no effect at all on commutation failures, i.e. when commutation on a valve has already started before the voltage decreases. Besides, the improvement of using firing angle advancement method is very limited for three-phase faults [111].

The second approach is to modify the controllers of HVDC systems. One widely adopted method is Voltage Dependent Current Order Limit (VDCOL) method [112–116], which protects HVDC systems by controlling current order if AC or DC voltages decrease below a certain value. The disadvantage of this method is that it can only reduce the probability of commutation failures but can not completely prevent its occurrence if the fault is electrically near to the inverter [117, 118].

Another solution is to insert additional components or devices into the systems, among which Capacitor-Commutated Converter HVDC (CCC-HVDC) [119–122] is the most common one. CCC-HVDC insert capacitors between the thyristor valves and the converter transformers so that reactive power consumption can be reduced. By doing so the extinction angle γ can be increased and thus give larger margin for commutation. However, CCC-HVDC places considerable voltage stress on thyristor valves and reduces device lifetime.

The Superconducting Fault Current Limiter (SFCL) can be a promising apparatus to prevent commutation failure but studies on this are rare. Reference [123] describes the effects of resistive SFCL on commutation failure qualitatively. It proves that SFCLs are effective in improving the converter restoration characteristics of HVDC systems. Reference [124]

shows flux-coupling-type SFCLs can reduce successive commutation failure and improve the fault recovery characteristics of HVDC system. However, no research has shown that a SFCL with suitable resistance can prevent commutation failure. The following simulation results demonstrate using SFCL can help mitigate commutation failure whenever a failure is initiated for all types of faults.

6.4 Using SFCL to mitigate commutation failure

6.4.1 Modeling for the studied DC grid

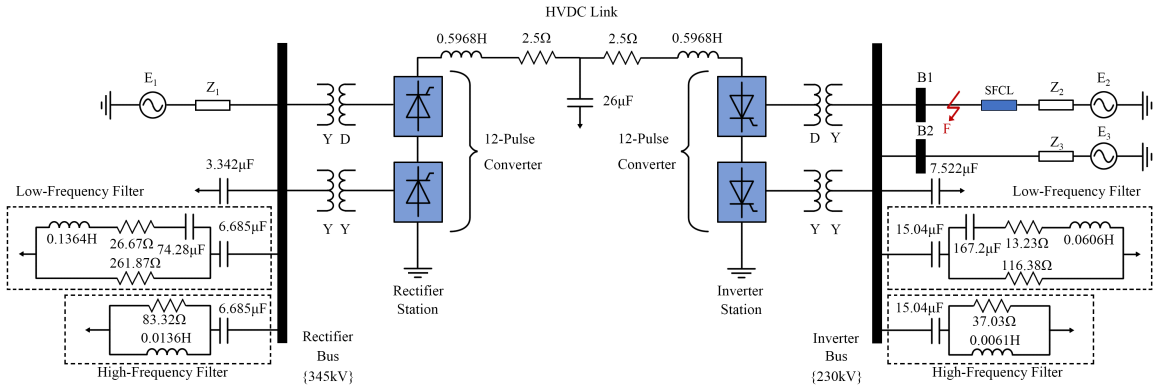

Fig. 6.6 Simulated DC network.

The diagram of the simulated DC network in shown in Fig. 6.6. The test network consists of three AC grids connected via a mono-polar 500 kV HVDC link.

A twelve-pulse converter which is comprised of two six-pulse Graetz bridges is deployed on both rectifier and inverter sides. Two bridges are connected to a Y-Y and a Y-Δ transformer respectively so that the AC voltage supplied to each bridge has a 30 phase shift. Series connection of the bridges reduces the ripple component, which is six times the fundamental frequency. Using twelve-pulse converters can effectively reduce harmonic distortion.

There is an AC system at the rectifier side and two identical AC systems at the inverter side. A voltage source and a resistor in series are used to model the AC networks, which are connected to the transformers through rectifier and inverter buses.

Four types of short-circuit faults will be simulated at the denoted location. R-SFCLs with different resistance values will be installed and tested in one AC network at the inverter side.

Low frequency filters and high frequency filters are on both sides to filter out harmonics.

The parameters of the test network are listed in table 6.1.

Table 6.1 Parameters of the test network

Parameter [Unit]	Rectifier	Inverter
Bus line-to-line voltage [kV]	345	230
AC system frequency [Hz]	50	50
Nominal firing angle [deg]	15	-
Nominal extinction angle [deg]	-	15

6.4.2 Time dependent model for the SFCL

The resistance characteristics of an SFCL device should be modeled as a nonlinear resistance because of the sharp changes of the resistance of superconducting material after the state transition incurred by the large current. One simple method is to simulate the SFCL as a time dependent resistance which starts to increase exponentially on occurrence of a fault, as shown in equation 6.4.1 and Fig. 6.7

$$R = \begin{cases} 0 \quad \Omega, \quad for \quad t < t_1 \\ \alpha[1 - e^{-q(t-t_1)}], \quad for \quad t \geq t_1 \end{cases} \tag{6.4.1}$$

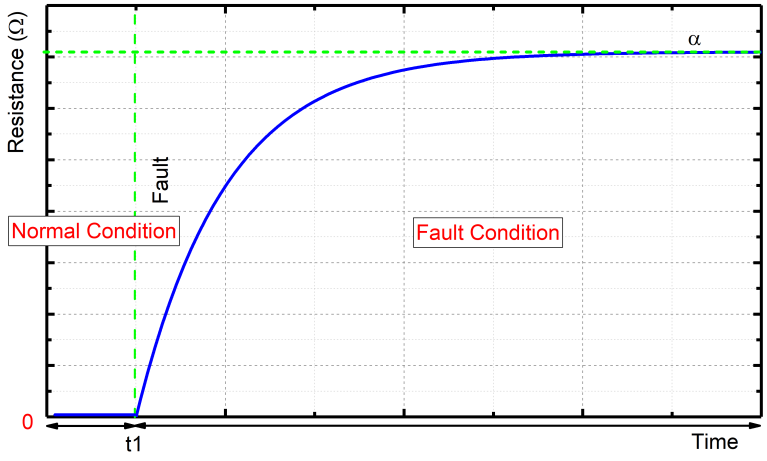

Fig. 6.7 Time dependent SFCL resistance characteristics.

In equation 6.4.1, α and q are constants: q defines how fast the resistance increases to an approximated value α. Normally α is equivalent to the resistance value of an SFCL device at

room temperature. In this simulation, α increase from 0-100 Ω to test its suppression effect for commutation failures.

6.4.3 Simulation results

Study of the resistance value of SFCL for successful commutation

The results obtained from the PSCAD simulation test of the proposed SFCL under different fault types and different fault resistance values are depicted in Fig. 6.8-6.11. In all cases, a fault was applied at t = 2 s for a duration of 0.2 s. With fault resistance increasing from 0Ω to 100Ω, the minimum resistance of SFCL for successful commutation can be obtained. We also tested different fault initiation times from 2.000 s to 2.020 s at intervals of 0.002s to observe the required SFCL resistance value.

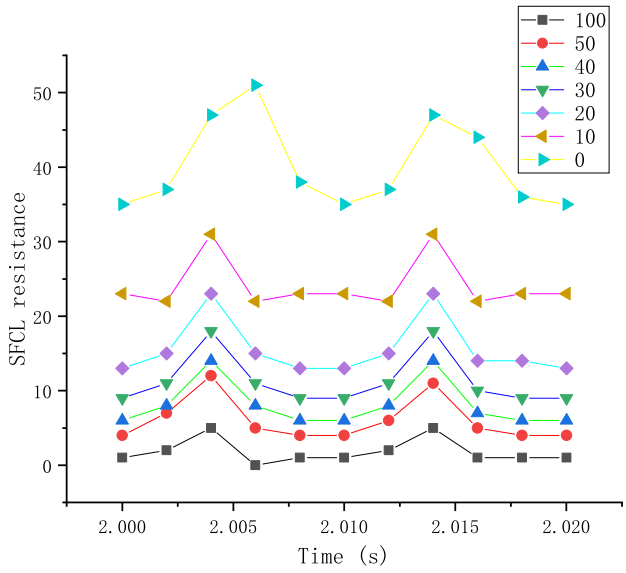

Fig. 6.8 The minimum resistance of an SFCL to suppress commutation failure at different fault initiation times for single-phase-to-ground faults (AG).

Referring to Fig. 6.8, when a single-line-to-ground fault takes place at point F on the test network, the minimum SFCL resistance needed for successful commutation increases with the decrease in the fault resistance. For a system of fault resistance= 0Ω, an SFCL resistance value should be at least 35Ω to ensure a successful commutation. In contrast, for a system of fault resistance= 100Ω, a 1Ω SFCL can meet the requirement. The required SFCL's resistance also varies with different fault initiation times. However, whenever the fault occurs, a SFCL with the corresponding resistance value can always prevent commutation

failure. This is a big advantage of using SFCL to suppress commutation failure compared to advancing the firing angle. Particularly, there is a noticeable resistance peak for a period of ten milliseconds and the mathematical analysis for this is as below.

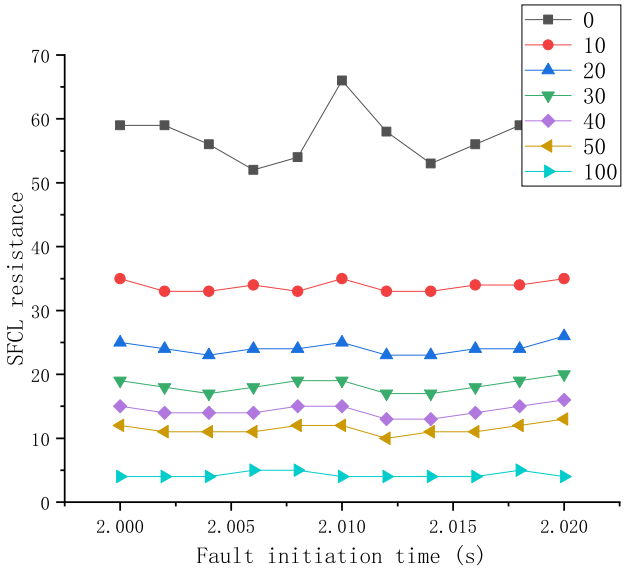

Fig. 6.9 The minimum resistance of SFCL to suppress commutation failure at different fault initiation times for three-phase fault (ABC).

As shown in Fig. 6.9, for a three phases ABC fault, the required SFCL resistance is generally larger than that for a single-line-to-ground fault. Because the fault is symmetrical, the minimum SFCL resistance differs marginally for different fault initiation times, especially when the fault resistance is large.

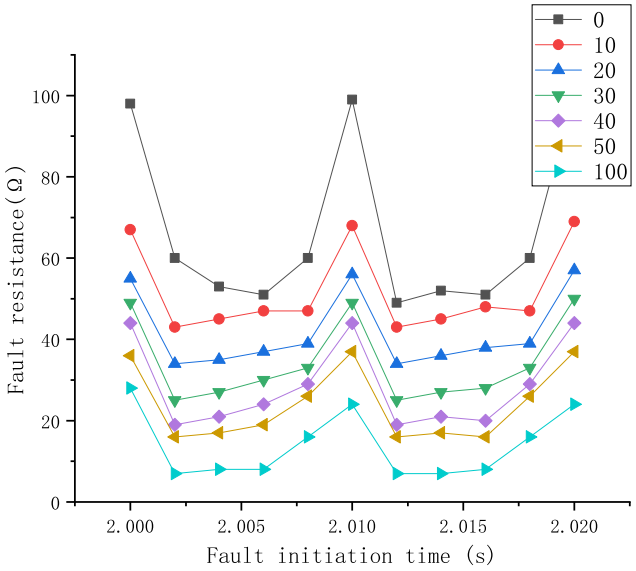

Fig. 6.10 The minimum resistance of an SFCL to suppress commutation failure at different fault initiation times for double-phase faults (BC).

As shown in Fig. 6.10, for double-phase faults, the required SFCL resistance is substantially larger than that for single-line-to-ground faults or for three-phase faults. The minimum SFCL resistance differs greatly for different fault initiation times.

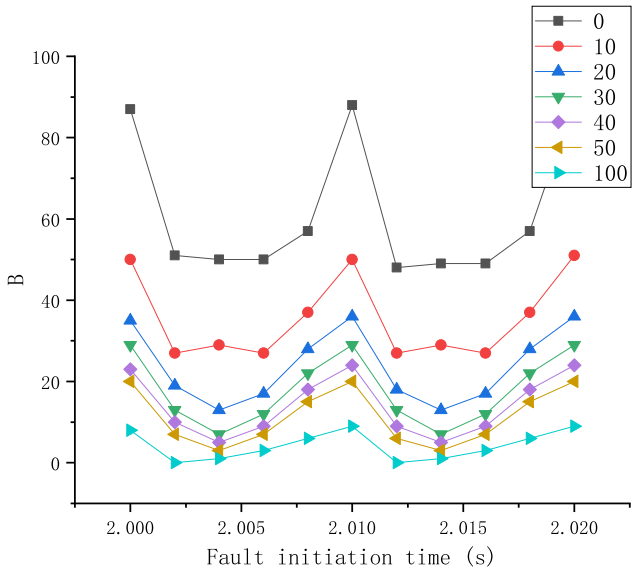

Fig. 6.11 The minimum resistance of an SFCL to suppress commutation failure at different fault initiation times for double-phase-to-ground faults (BCG).

As shown in Fig. 6.11, for double-phase-to-ground faults, the required SFCL resistance is larger than that for single-line-to-ground faults or for three-phase faults but slightly smaller than that for double-phase faults. The minimum SFCL resistance also differs greatly for different fault initiation times.

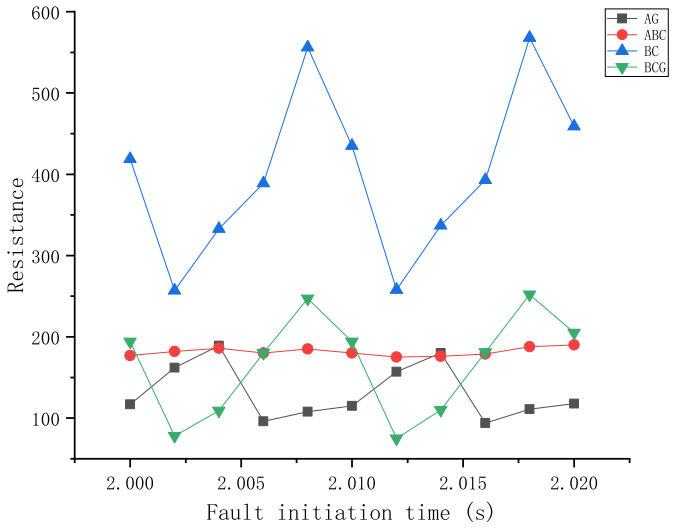

Fig. 6.12 The minimum fault resistance to secure successful commutation at different fault initiation times for four types of faults.

Fig. 6.12 compares the minimum fault resistance to a system to ensure no commutation failure occurs in this system for the four types of short circuits. It is clear that the double-phase faults are the most severe that can easily induce commutation failure. The fault resistance should reach nearly 600Ω so that all commutation would be successful.

Influences of the SFCL on a DC system with commutation failure

The following diagrams show the influences of a resistive SFCL on the HVDC system where a commutation failure exists.

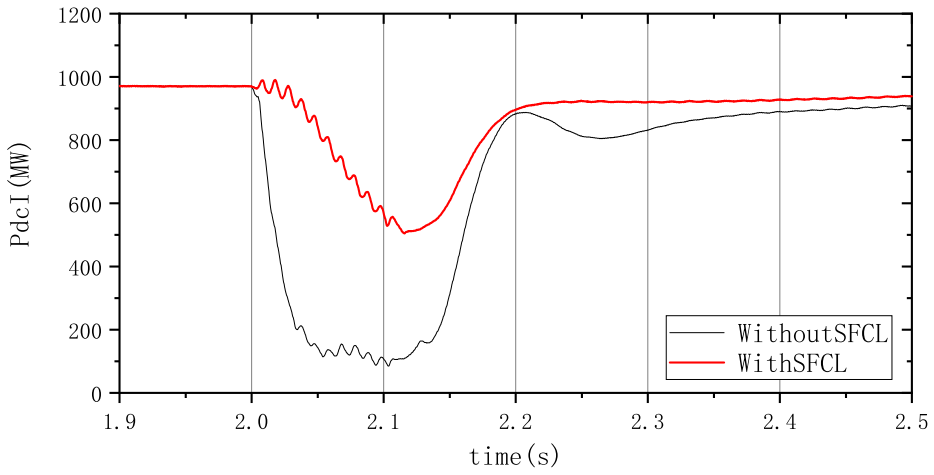

Fig. 6.13 Comparison of the active power waveform with and without SFCL.

When a fault occurs at 2.0 s, the active power dips to nearly 0 MW from 980 MW which means a power transmission interruption caused by commutation failure. When an SFCL is installed, the reduction is only half that of the non-SFCL value.

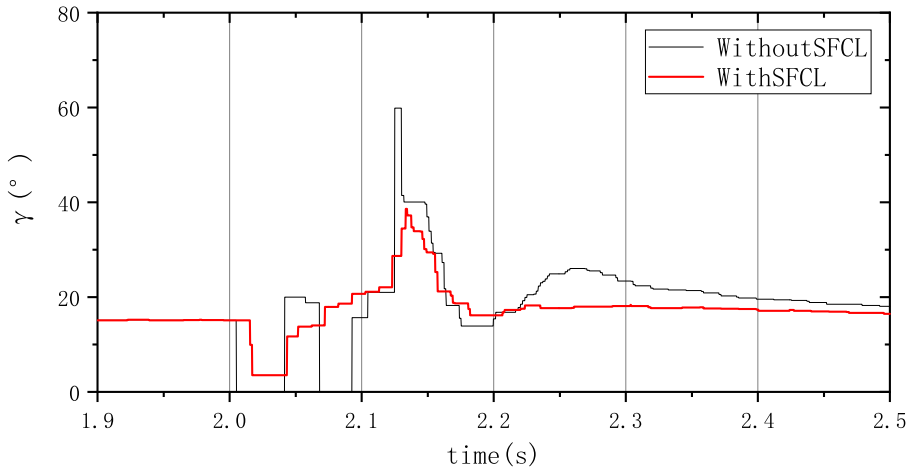

Fig. 6.14 Comparison of the extinction angle with and without SFCL.

When a fault occurs at 2.0 s, the extinction angle decreases to 0 degreesis in the next few milliseconds, which is characterized as a commutation failure. When an SFCL is installed, the extinction angle has been improved to above zero. This means that the commutation is successful.

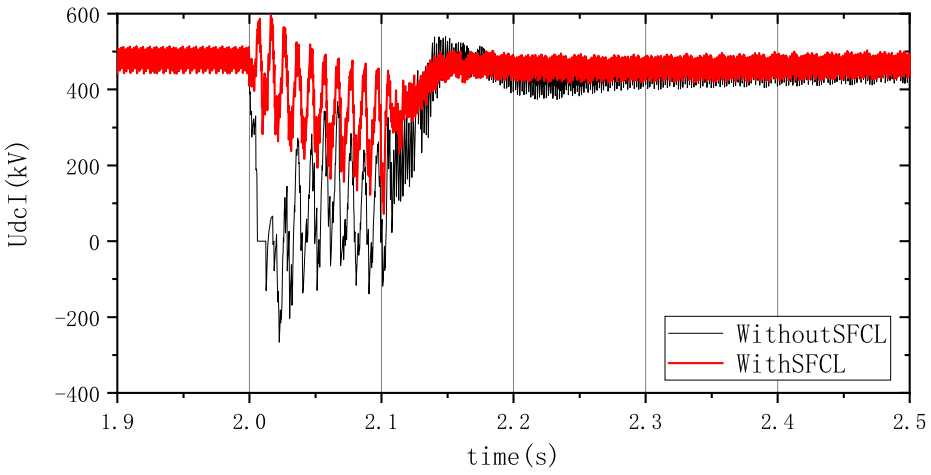

Fig. 6.15 Comparison of the voltage waveform with and without SFCL.

Without SFCL, the DC voltage reaches zero and this is a sign of commutation failure. A significant improvement in DC voltage at the inverter side is observed with the installation of an SFCL.

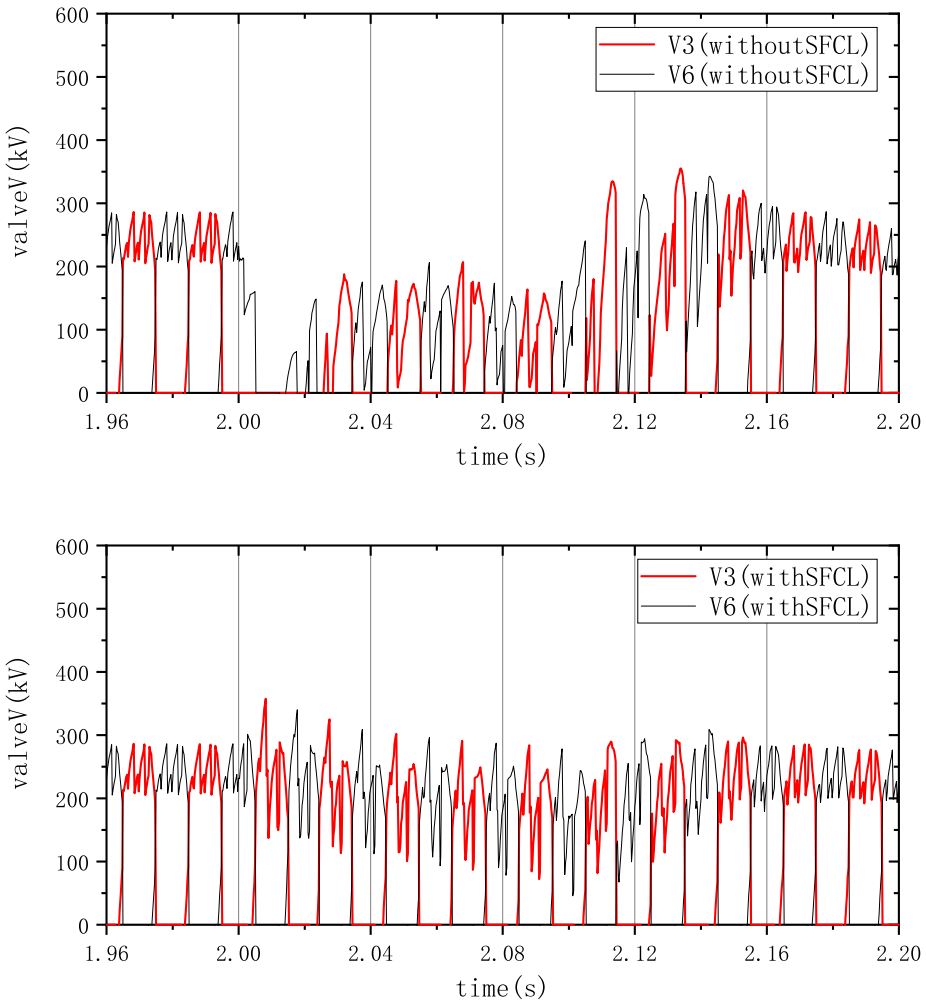

Fig. 6.16 Comparison of the valve T3 and T6 voltage waveform with and without SFCL.

Fig. 6.16 compares the valve voltages of T3 and T6 with and without SFCL. Without SFCL, there are times when voltages of T3 and T6 become zero at the same time. This means T3 and T6 conduct at the same time and represents for commutation failure. It is clear that with an SFCL this problem has been solved.

6.4.4 Quantitative analysis

For a $\Delta - Y$ transformer, commutation voltages are U_{OP}, U_{PQ}, U_{QO}. We assume the transformer's turnsratio is k.

$$U_{OP} = kU_A, \quad U_{PQ} = kU_B, \quad U_{QO} = kU_C \tag{6.4.2}$$

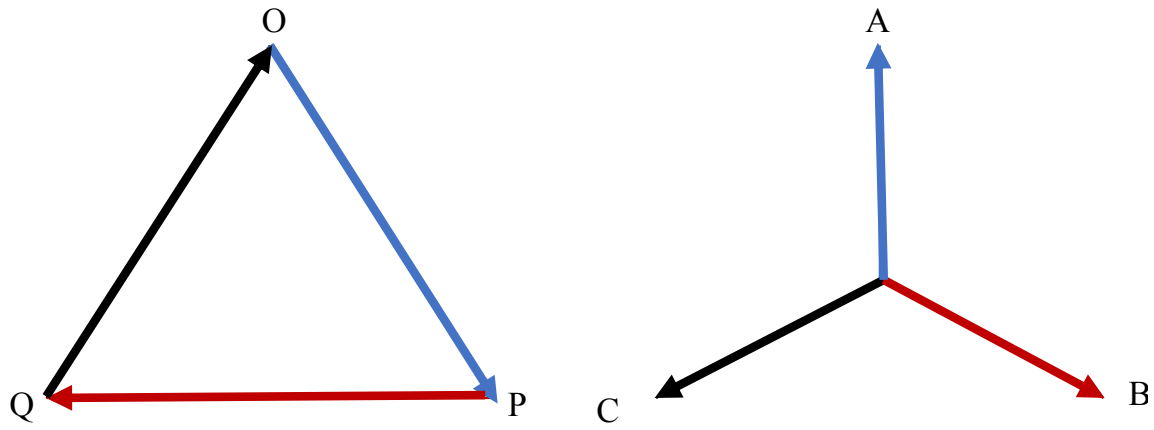

Fig. 6.17 Phasor diagram of commutation voltages and three-phase voltages, $\Delta - Y$

For a $Y - Y$ transformer, commutation voltages are U_{MO}, U_{MP}, U_{MQ}. The transformer's turnsratio is $\frac{k}{\sqrt{3}}$.

$$U_{MO'} = \frac{k}{\sqrt{3}}U_A, \quad U_{MP'} = \frac{k}{\sqrt{3}}U_B, \quad U_{MQ'} = \frac{k}{\sqrt{3}}U_C \tag{6.4.3}$$

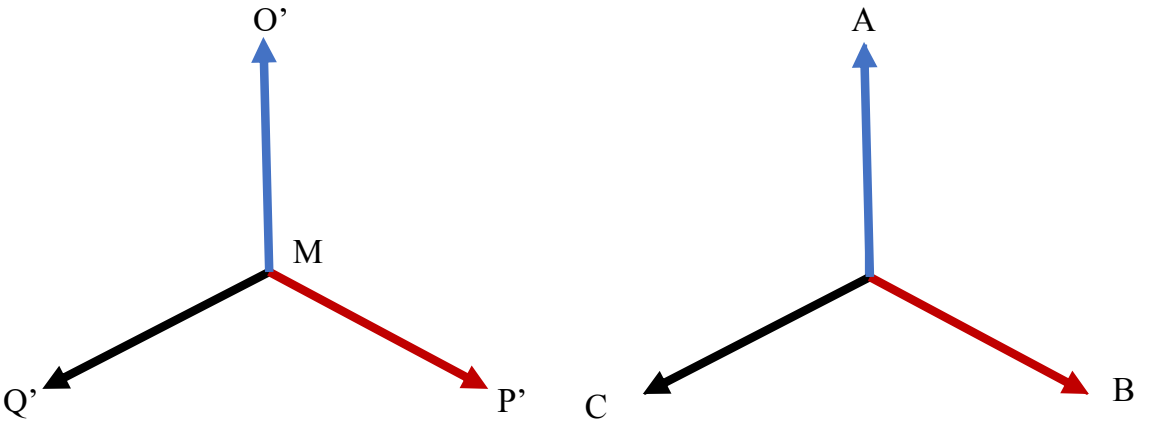

Fig. 6.18 Phasor diagram of commutation voltages and three-phase voltages, $Y - Y$.

When a single-phase-to-ground fault (AG) happens, the voltage of phase A U_A decrease by ΔU.

$$\begin{cases} U_{OP} = k(U_A - \Delta U) \\ U_{PQ} = kU_B \\ U_{QO} = kU_C \\ U_{MO'} = \frac{k}{\sqrt{3}}(U_A - \Delta U) \\ U_{MP'} = \frac{k}{\sqrt{3}}U_B \\ U_{MQ'} = \frac{k}{\sqrt{3}}U_C \end{cases} \tag{6.4.4}$$

As a result, the commutation voltage of Y-Y transformer is

$$\begin{cases} U_{O'P'} = \frac{k}{\sqrt{3}}\sqrt{3U_A^2 - 3\Delta U U_A + \Delta U^2} \\ U_{P'Q'} = kU_B \\ U_{Q'O'} = \frac{k}{\sqrt{3}}\sqrt{3U_C^2 - 3\Delta U U_C + \Delta U^2} \end{cases} \tag{6.4.5}$$

U_{OP}, U_{PQ}, U_{QO}, $U_{O'P'}$, $U_{P'Q'}$ and $U_{Q'O'}$ are six commutation voltages. According to voltage-time-area theory, commutation area is proportional to the voltage amplitude. In the above six voltages, U_{OP} is the substantially smaller than the other five voltages value. Therefore a larger SFCL resistance is required for this situation and thus there is a noticeable peak value in each a half cycle (10ms), as shown in Fig.6.8.

For three-phase faults, the voltages of three phases decrease by ΔU respectively.

$$\begin{cases} U_{OP} = k(U_A - \Delta U) \\ U_{PQ} = k(U_B - \Delta U) \\ U_{QO} = k(U_C - \Delta U) \\ U_{MO'} = \frac{k}{\sqrt{3}}(U_A - \Delta U) \\ U_{MP'} = \frac{k}{\sqrt{3}}(U_B - \Delta U) \\ U_{MQ'} = \frac{k}{\sqrt{3}}(U_C - \Delta U) \end{cases} \tag{6.4.6}$$

As a result, the commutation voltage of Y-Y transformer is

$$\begin{cases} U_{O'P'} = k(U_A - \Delta U) \\ U_{P'Q'} = k(U_B - \Delta U) \\ U_{Q'O'} = k(U_C - \Delta U) \end{cases} \tag{6.4.7}$$

In this case, the six commutation voltages are of similar values so the SFCL resistance values needed for each situation are almost the same, which results in the comparatively stable waveform (illustrated in Fig. 6.9).

For double-phase faults,

$$\begin{cases} U_{OP} = kU_A \\ U_{PQ} = \frac{k}{2}U_B \\ U_{QO} = \frac{k}{2}U_C \\ U_{MO'} = \frac{k}{\sqrt{3}}U_A \\ U_{MP'} = \frac{k}{2\sqrt{3}}U_B \\ U_{MQ'} = \frac{k}{2\sqrt{3}}U_C \end{cases} \tag{6.4.8}$$

the commutation voltages of Y-Y transformer are

$$\begin{cases} U_{O'P'} = \frac{k\sqrt{3}}{2}U_A \\ U_{P'Q'} = 0 \\ U_{Q'O'} = \frac{k\sqrt{3}}{2}U_C \end{cases} \tag{6.4.9}$$

It is obvious that $U_{P'Q'}$ is the smallest compared to other voltage values and this represents for the peak value in Fig. 6.10 and meanwhile in Fig. 6.12. double-phase faults are the most severe type among all fault types.

For double-phase-to-ground faults,

$$\begin{cases} U_{OP} = kU_A \\ U_{PQ} = k(U_B - \Delta U) \\ U_{QO} = k(U_C - \Delta U) \\ U_{MO'} = \frac{k}{\sqrt{3}}U_A \\ U_{MP'} = \frac{k}{2\sqrt{3}}(U_B - \Delta U) \\ U_{MQ'} = \frac{k}{2\sqrt{3}}(U_C - \Delta U) \end{cases} \tag{6.4.10}$$

The commutation voltages of Y-Y transformer are

$$\begin{cases} U_{O'P'} = \frac{k}{\sqrt{3}}\sqrt{3U_A^2 - 3\Delta U U_A + \Delta U^2} \\ U_{P'Q'} = \frac{k}{\sqrt{3}}(U_B - \Delta U) \\ U_{Q'O'} = \frac{k}{\sqrt{3}}\sqrt{3U_C^2 - 3\Delta U U_C + \Delta U^2} \end{cases} \tag{6.4.11}$$

Comparing the results to those for double-phase faults, the commutation voltages are bigger so the required SFCL resistances are smaller, as shown in Fig. 6.12.

Chapter 7

Influences of SFCL on protective relays

Protective relays, defined by IEEE, as "a relay whose function is to detect defective lines or apparatus or other power system conditions of an abnormal or dangerous nature and to initiate appropriate control circuit action." In fact, the function of most protective relays is to initiate circuit-breaker opening. Short circuited faults are the most common seen abnormal conditions that happens to a electric grid, which results primarily from lighting induced transient high voltage, natural disasters like storms, and falling objects like tree limbs. In a power system, most faults are one-phase-to ground faults, the approximate percentages of occurrence of the other three types of fault are as the following [125]:

Single-phase-to-ground faults: 70% - 80%
Dougble-phase-to-ground faults: 17% – 10%
Double-phase faults: 10% – 8%
Three-phase faults: 3% – 2%

7.1 Introduction to protective relays

7.1.1 Categories of protective relays

Protective relays are classified by their protection targets: electric line protective relays and electric element protective relays. Here, we only discuss electric line protective relays, which can be further classified by performance characteristics; for example: over-current, under-voltage, over-voltage, distance, directional pilot, current differential, etc .

7.1.2 Protective relay performance

The performance of a protective relays can be categorized as (1) correct, (2) incorrect, and (3) no conclusion. Correct operation indicates that the trouble area was properly isolated within the time expected. Statistically, nearly 99% of all relay operations are corrected as desired. Incorrect operation can cause either incorrect isolation of a no-trouble area, or a failure to isolate a trouble area. This can be caused by misapplication of relays, incorrect setting, and equipment problems, or failures. Integration of superconducting fault current limiter can also lead to misapplication of relays: the sudden change of state of a superconductor alters the topology of a power grid and may affect normal operation some types of protective relays due to their operating principles. Hence, it is vital to carefully study how SFCLs will affect different kinds of protective relays in order to minimize negative effects of resultant incorrect operation of a protective relay.

7.2 Protective relaying using fault increment

7.2.1 Fault increment

Fault increment is defined as the rising electrical quantity when faults occurs in power system. A simplified power system with double sources S_m and S_n is shown in Fig. 7.1. Z_{sm} and Z_{sn} respectively are the equivalent system impedance of terminal m and terminal n.The length of the transmission line is l. When a short-circuit fault F occurs in the transmission line, it is assumed that the voltage and current of terminal m and n are U_m, I_m and U_n, I_n respectively. At this time, the whole system remains in the fault state.

For a linear system, the fault state could be decomposed by Superposition theorem. As shown in Fig. 7.1 (a), the power system with a fault at point F is equivalent to the system where two voltage sources $U_{f[0]}$ and $-U_{f[0]}$ that are equal in value and opposite in direction are connected in series at point F. $U_{f[0]}$ is the voltage at point F before a fault occurs.

The superposition theorem for electrical circuits states that for a linear system the response (voltage or current) in any branch of a bilateral linear circuit which has more than one independent source is equal to the algebraic sum of the responses caused by each independent source acting alone; where all other independent sources are replaced by their internal impedances.

Therefore, according to the Superposition theorem, the fault state (Fig. 7.1 (a)) could be decomposed into non-fault state (Fig. 7.1 (b)) and fault additional state (Fig. 7.1 (c)). The fault increment can be extracted by the following equations (terminal m is taken as an example):

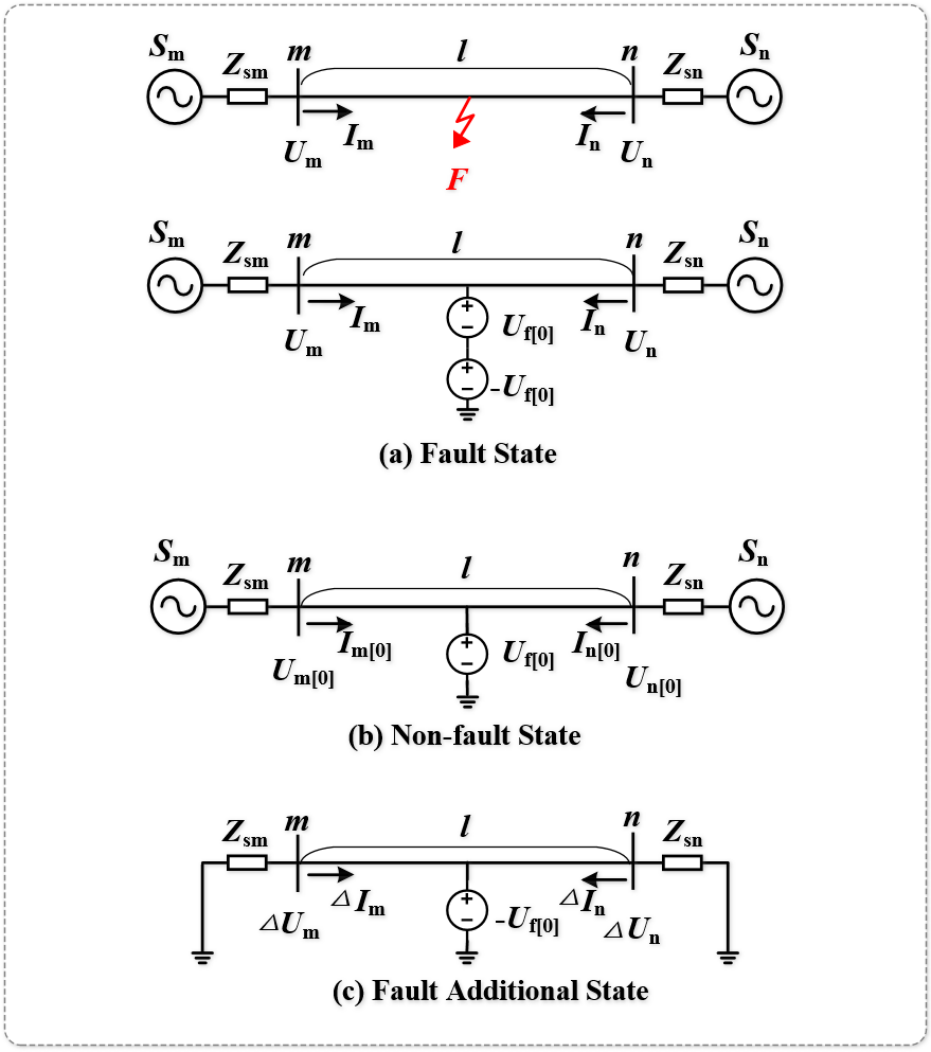

Fig. 7.1 Diagram of power system fault decomposition.

$$\begin{cases} \Delta U_m = U_m - U_{m[0]} \\ \Delta I_m = I_m - I_{m[0]} \end{cases} \tag{7.2.1}$$

U_m, I_m are the voltage and current of terminal M in the fault state, respectively; $U_{m[0]}$, $I_{m[0]}$ are the voltage and current of terminal M in the non-fault state, respectively; ΔU_m, ΔI_m are the voltage and current of terminal M in the fault additional state, respectively;

In Fig. 7.1, fault state is the practical state of a power system when short circuit faults occur in the system, where U_m, I_m are the real voltage and current of terminal M that can be measured. Non-fault state is the practical state of a power system before a fault occurs and normally it refers to the normal operation state of a system. $U_{m[0]}$, $I_{m[0]}$ can also be measured.

In contrast, fault additional state is induced by a fault; thus it only exists after a fault occurs in the system. This means fault additional state only contains fault information. The electrical quantities in fault additional state, such as ΔU_m, ΔI_m, ΔU_n, ΔI_n, representing fault information, are fault increments. Therefore, fault additional state is the base on which we can study and analysis fault information.

7.2.2 Distance protection using fault increments

Fig. 7.2 shows the fault additional state of a double sources power system with a fault at point F. The measured impedance from terminal m to fault point is Z_F. The voltage at point F before a fault occurs is $U_{f[0]}$.

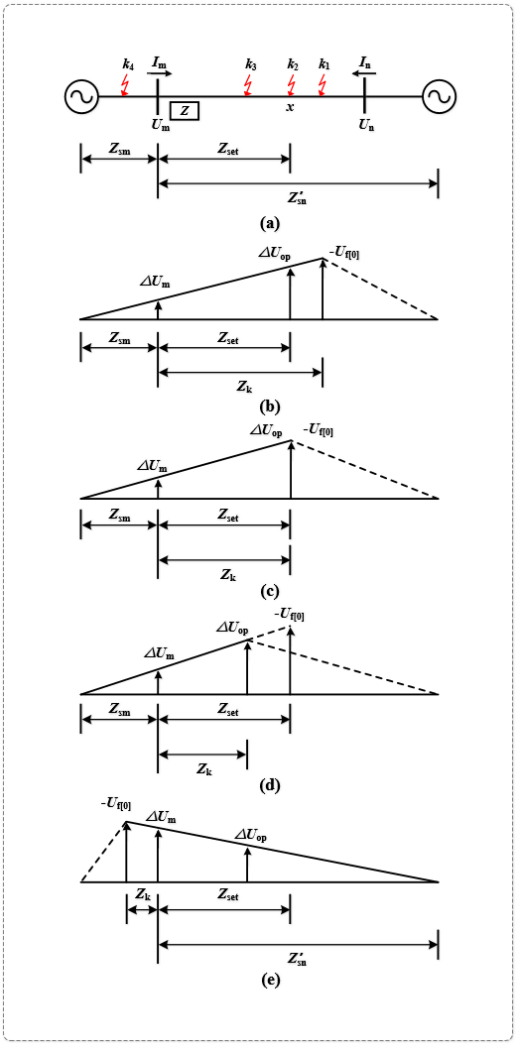

Fig. 7.2 Diagram of power system fault decomposition.

When a fault at point F occurs, the voltage equation is:

$$-\Delta U_m - U_{f[0]} = -\Delta I_m Z_F \tag{7.2.2}$$

Operation criterion

Based on 7.2.4, it is easy to get:

$$-U_{f[0]} = \Delta U_m - \Delta I_m Z_F \tag{7.2.3}$$

The protective relay is installed at terminal m, with its protection range x (setting point),setting impedance Z_{set}.

1) When a positive direction fault for terminal m occurs in the transmission line, the fault increment can be expressed by:

a) When $Z_F = Z_{set}$, the fault point F is at the end of protection range (k_2) and the relay is at the boundary condition to operate.

$$-U_{f[0]} = \Delta U_m - \Delta I_m Z_{set} \tag{7.2.4}$$

if $U_{op} = \Delta U_m - \Delta I_m Z_{set}$ is called compensation voltage, there is

$$|U_{op}| = |-U_{f[0]}| \tag{7.2.5}$$

b) When $Z_F = Z_{set} + \Delta Z$, the fault point F is out of the protection range (k_1) ,i.e. external fault

$$\begin{aligned} -U_{f[0]} &= \Delta U_m - \Delta I_m (Z_{set} + \Delta Z) \\ &= \Delta U_m - \Delta I_m Z_{set} - \Delta I_m Z_{set} \\ &= |U_{op}| - \Delta I_m Z_{set} \end{aligned} \tag{7.2.6}$$

Since $U_{op} = \Delta U_m - \Delta I_m Z_{set} = -\Delta I_m Z_{sm} - \Delta I_m Z_{set}$, so

$$|U_{op}| < |-U_{f[0]}| \tag{7.2.7}$$

c) When $Z_F = Z_{set} - \Delta Z$, the fault point F is inside the protection range (k_3),i.e. internal fault

$$\begin{aligned} -U_{f[0]} &= \Delta U_m - \Delta I_m (Z_{set} - \Delta Z) \\ &= \Delta U_m - \Delta I_m Z_{set} + \Delta I_m Z_{set} \\ &= |U_{op}| + \Delta I_m Z_{set} \end{aligned} \tag{7.2.8}$$

so

$$|U_{op}| > |-U_{f[0]}| \tag{7.2.9}$$

2) When a reverse direction fault (k_4) for terminal m occurs, the voltage fault increment of the transmission line gradually decreases from the fault point to the neutral point at the opposite side, and the current fault increment flows from the bus to the line (as shown in Fig. 4e), then

$$-U_{f[0]} = \Delta U_m + \Delta I_m Z_b \tag{7.2.10}$$

so

$$|U_{op}| < |-U_{f[0]}| \tag{7.2.11}$$

Obviously, the operation voltage $|U_{op}|$ is greater than fault voltage $|U_{f[0]}|$ for an internal fault; Conversely, $|U_{op}|$ is always smaller than $|U_{f[0]}|$ for an external fault or a reverse direction fault. Therefore, the operation criterion should be

$$|U_{op}| \geq |-U_{f[0]}| \tag{7.2.12}$$

Above analysis has proven this criterion guarantees the relay operates when a fault occurs within the protection range (internal fault) and does not operate when a fault occurs out of the protection range (external fault or inverse direction fault).

In practical application, protective relays first save the voltage and current value of normal operation. When a fault occurs, the fault increment voltage and fault increment current can be calculated by subtracting the voltage and current in fault state from their normal counterparts, thus determining the operating voltage. Meanwhile it is assumed the fault point voltage $|U_{f[0]}|$ equals the voltage at the same point before a fault occurrence.

Inter-phase fault distance component Inter-phase fault distance component works for all inter-phase faults (including double-phase-to-ground fault). The working principle of distance component is based on the fault increment of phase voltage difference and the fault increment of phase current difference, its operation criterion:

$$|U_{op\phi\phi}| > |-U_{f[0]}| \tag{7.2.13}$$

In the equation 7.2.13, $\phi\phi$ represents the difference between phase A and phase B, phase B and phase C, phase C and phase A. $U_{op\phi\phi} = U_{\phi\phi} - I_{\phi\phi} Z_{set}$ From equation 7.2.13, to make

the relay work, the fault phase must be selected first, or computing U_{opAB}, U_{opBC}, U_{opCA} in turn.

Ground fault distance component Equation 7.2.13 does not consider single phase-to-ground fault, so a ground fault distance component must be added. The working principle of ground fault distance component is based on the fault increment of phase voltage difference and the fault increment of phase current difference, its operation criterion:

$$|U_{op\phi}| > |-U_{f[0]}| \tag{7.2.14}$$

In the equation 7.2.14, ϕ represents phase A, phase B, phase B or phase C. $U_{op\phi} = U_{\phi} - (I_{\phi} + K * 3I_0)Z_{set}$
From equation 7.2.14, to make the relay work, the fault phase must be selected firstly, or computing U_{opA}, U_{opB}, U_{opC} in turn.

7.2.3 Effects of the SFCLs on the IPFR

One of the biggest challengs that prevent the industrialization of SFCLs is the coordination between the SFCLs and protective relays. Because the integration of SFCLs to power grids change the fault transient characteristics, the reliability and sensitivity of the protection relays will be challenged. Therefore, it is important to study the effects of the SFCLs on protection relays to ensure the safe operations of the power system.

To date, significant research has been conducted on coordination of different types of SFCL with different types of protective relays. The authors in [126] and [127] investigated the performance of distance relay in the presence of saturated iron core SFCL and diode bridge type SFCL for different types of faults. Reference [128] further considered the impact of a bridge-type SFCL and SMES integration on the distance relay. In [129], the coordination of four types of overcurrent protection relays with a SFCL is compared and evaluated. [130] and [131] also focus on the overcurrent protection but they specified the SFCL as a flux lock type and an active saturated iron-core type SFCL (SISFCL) respectively. Reference [132] studied the influence of an SISFCL on the zero-sequence current protection. However, no research has been done on the coordination of the resistive SFCL and incremental power frequency relay. This should be studied carefully.

Here we mainly study the influences of resistive SFCLs on IPFRs under circumstances of four types of short-circuited fault, including both symmetrical and asymmetrical fault. First, power transmission systems without and with SFCLs are respectively simulated; this way the influences brought by SFCLs can be analyzed. To eliminate negative effects of SFCLs,

three different coordination schemes between SFCLs and IPFRs are proposed. Finally, correctness of the theoretical analyses and the validity of the coordination scheme are verified by simulation results.

SFCLs do not present any impedance in normal operation and thus will not affect operation of the power system. When a short-circuit fault happens, SFCLs rapidly transition to high impedance state, in order to limit the fault current. This indicates that integration of SFCLs will affect the extraction of the fault increment.

In fact, the correct extraction of the fault increment with the integration of SFCLs should be presented by the schematic diagram. However, SFCLs are negligible for power systems in the non-fault state, which directly leads to the deviation of the extraction of the fault increment. This should be considered carefully

$$\begin{aligned}\Delta U_m'' &= U_m - U_{m[0]} = U_m - U_{m[0]}' + U_{m[0]}' - U_{m[0]} \\ &= \Delta U_m + \left(U_{m[0]}' - U_{m[0]}\right) = \Delta U_m + U_A \end{aligned} \tag{7.2.15}$$

$$\begin{aligned}\Delta I_m'' &= I_m - I_{m[0]} = I_m - I_{m[0]}' + I_{m[0]}' - I_{m[0]} \\ &= \Delta I_m + \left(I_{m[0]}' - I_{m[0]}\right) = \Delta I_m + I_A \end{aligned} \tag{7.2.16}$$

1) When a positive direction fault for terminal M occurs in the transmission line, the relationship between ΔU_{OP} and $-U_{f[0]}$ is expressed by:

$$\begin{aligned}\Delta U_{OP} &= \Delta U_m'' + \left(-I_m''\right) Z_{set} \\ &= \Delta U_m - \Delta I_m \times Z_{set} + (U_A - I_A Z_{set}) \\ &= -\frac{Z_{sm} + Z_{\text{set}}}{Z_{sm} + Z_k + Z_{SFCL}} U_{f[0]} + U_B \end{aligned} \tag{7.2.17}$$

2) When a reverse direction fault for terminal M occurs in the transmission line, the relationship between ΔU_{OP} and $-U_{f[0]}$ is expressed by:

$$\begin{aligned}\Delta U_{OP} &= \Delta U_m'' + \left(-I_m''\right) Z_{set} \\ &= \Delta U_m - \Delta I_m \times Z_{set} + (U_A - I_A Z_{set}) \\ &= -\frac{Z_{sn}' + Z_{SFCL} - Z_{set}}{Z_{sn}' + Z_k + Z_{SFCL}} U_{f[0]} + U_B \end{aligned} \tag{7.2.18}$$

where $U_B = U_A - I_A Z_{set}$

Usually, the setting of Z_{set} should take the impedance of SFCL Z_{SFCL} into consideration. Therefore, it can be seen that existence of U_B significantly affects the relationship between ΔU_{OP} and $-U_{f[0]}$ while U_B is influenced by the differences $U'_{m[0]}$ -$U_{m[0]}$ and $I_{m[0]}$ - $I_{m[0]}$. And $U'_{m[0]}$, $I'm[0]$ can be calculated when the Z_{SFCL} is presented in the normal operation. Then, the larger the Z_{SFCL} is, the bigger the differences $U'_{m[0]}$ - $U_{m[0]}$ and $I'_{m[0]}$ - $I_{m[0]}$ are. As a result, the IPFR might malfunction when it is asked not to operate and mis-operation when it is required to operate.

Based on the analysis above, integration of SFCLs into the power system disrupts the relationship between the operation voltage $|\Delta U_{OP}|$ and fault voltage $|U_{f[0]}|$. When a positive direction inner fault occurs, IPFR may misfunction; when a positive direction external fault or a reverse direction fault occurs, IPFR may malfunction,as shown in Fig. 7.3

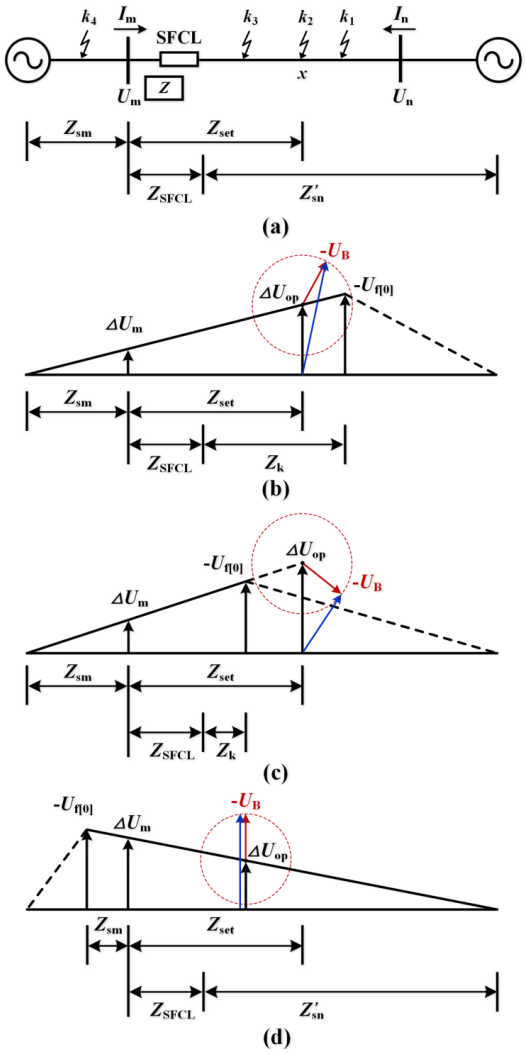

Fig. 7.3 Voltage fault increment distribution diagram with SFCLs.

7.3 Simulation analysis

The following simulation results demonstrate the correctness and validity of theoretical analyses in the previous sections.

7.3.1 Configuration of the power system

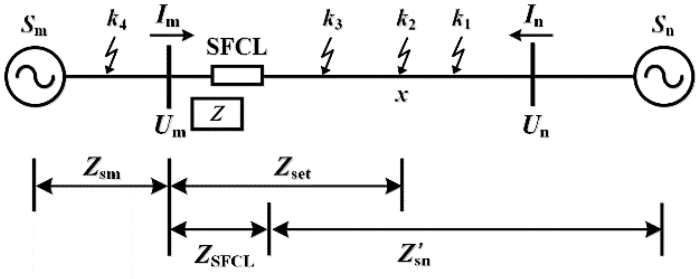

Fig. 7.4 Diagram of power system model.

A double sources three-phase power system is simulated in MATLAB SIMULINK and the schematic is shown in Fig. 7.4. An IPFR device is installed near source S_m to protect line L_{MN}. Meanwhile a resistive SFCL is deployed at terminal M to limit the short-circuited current. Parameters of the power system are listed in table 7.1.

Table 7.1 Power system parameters

Parameters	Value
Transmission line length	100 km
Expected protection distance	85 km
Phase-to-phase voltage of S_M and S_N	230 kV
Phase-to-phase voltage of S_M and S_N	0° and 20°

7.3.2 Simulation results

The simulation results reveal that when a positive direction inner fault occurs, IPFR misfunction. The studied fault types include both symmetrical faults: three-phase faults; and unsymmetrical faults: single-phase-to-ground faults, double-phase faults and double-phase-to-ground faults. The resistance of R-SFCL ranges from 5Ω to 30Ω.

Table 7.2-7.5 compares the protection distance of IPFR with and without the R-SFCL, and show the protection distance of IPRF decreases with the increase of SFCL's impedance

when four types of short-circuit fault occur (three-phase faults, single-phase-to-ground faults, double-phase faults, double-phase-to-ground faults) occur in the power system.

Three methods of compensation are proposed to eliminate the negative effect of SFCL. Method I changes the setting impedance Z_{set} of IPFR. It adds the impedance of SFCL directly to Z_{set}. The corresponding result is listed in the fourth column in Table 7.2-7.5. Method II alters both the setting impedance Z_{set} and K factor of IPFR. In Method III, a compensation factor σ is introduced to change the setting impedance Z_{set}. Numerous attempts prove that when $\sigma = 0.85$, the protection distance can be improved to a very desirable level.

It can be seen from Table 7.2 that when symmetrical three-phase faults occur in the power system, the protection distance of IPRF decrease from 80 km to 21 km with SFCL impedance rising from 5Ω to 30Ω.

Table 7.2 Influences of R-SFCL on IPFR under three-phase faults

SFCL impedance value (Ω)	Protection distance(km)				
	without SFCL	with SFCL	adjustment Method I	Method II	Method III
5	83	80	84	84	83
10	83	75	86	86	84
15	83	67	88	88	84
20	83	56	90	90	84
25	83	41	94	94	84
30	83	21	/	/	84

Table 7.3 demonstrates that for unsymmetrical single-phase-to-ground faults, when the resistance of SFCL is 5Ω, it hardly affects the operation of IPFR. However, when the resistance of SFCL increases to 30Ω, the protection distance shrinks to 68/85 km.

Table 7.3 Influences of R-SFCL on IPFR under single-phase-to-ground faults fault

SFCL impedance value (Ω)	Protection distance(km)				
	without SFCL	with SFCL	adjustment Method I	adjustment Method II	adjustment Method III
5	83	83	87	84	84
10	83	82	92	86	83
15	83	79	96	87	83
20	83	77	/	89	83
25	83	73	/	91	82
30	83	68	/	94	83

Table 7.4 shows the relation of IPFR protection distance with SFCL impedance value under unsymmetrical double-phase faults. It is clear that the protection distance decreases dramatically from 80 km to 21 km with SFCL impedance rising.

Table 7.4 Influences of R-SFCL on IPFR under double-phase faults fault

SFCL impedance value (Ω)	Protection distance(km)				
	without SFCL	with SFCL	adjustment Method I	adjustment Method II	adjustment Method III
5	83	80	84	84	83
10	83	75	86	86	84
15	83	67	88	88	84
20	83	56	90	90	83
25	83	41	94	94	84
30	83	21	/	/	84

Table 7.5 shows the relation of IPFR protection distance with SFCL impedance value under unsymmetrical double-phase-to-ground faults. The protection distance decreases slightly from 83 km to 71 km with SFCL impedance rising to 30Ω.

Table 7.5 Influences of R-SFCL on IPFR under double-phase-to-ground faults

SFCL impedance value (Ω)	Protection distance(km)				
	without SFCL	with SFCL	adjustment Method I	Method II	Method III
5	83	83	88	85	84
10	83	83	95	87	85
15	83	83	/	88	84
20	83	80	/	91	84
25	83	76	/	94	84
30	83	71	/	/	84

7.3.3 Simulation results analysis

Comparing the simulation results in the above four tables, it can be seen that: installation of SFCLs affect the protection distance of IPFRs regardless of the type of short- circuit fault. Particularly, SFCL has the largest negative impact on IPFR for double-phase faults and three-phase faults: for both of them the protection distance declined sharply to 20km. SFCLs affect IPFRs to less extent for one-phase-to-ground faults and for two phases to ground faults. In these cases, the protection distance decreases to 68/85km and 71/85km respectively when the impedance of SFCL is 30Ω.

The reason is that, as described in 7.2.2, there are two components of IPFRs (inter-phase fault distance component and ground fault distance component) and each has own operation criterion (Eq.7.2.13 and Eq.7.2.14). For single-phase-to-ground faults, the operation depends on the criteria for ground fault distance component. For double-phase faults, IPFR depends on the criteria for inter-phase fault distance component. For three-phase faults and double-phase-to-ground faults, both criteria may take effect. But for the studied model, it can be deduced that only inter-phase fault distance component's criteria come into effect for three-phase faults because they share the same figure as double-phase faults. The reasons for this are complicated and will be explained in future work.

Method I tends to over-compensate the protection distance. Method II does not improve the operation of IPFR for three-phase faults and double-phase faults compared to Method I, but for the other two types (single-phase-to-ground faults and double-phase-to-ground faults), its compensation effect improves significantly. The explanation is as follows.

Two parameters in operation criteria of IPFRs can be changed: setting impedance of IPFR Z_{set} and Zero-Sequence Current Compensation Factor K. Its definition

$$K = \frac{Z_0 - Z_1}{3Z_1} \tag{7.3.1}$$

where Z_0 and Z_1 are zero-sequence impedance and positive-sequence impedance of transmission lines respectively.

Z_{set} exists in both criteria so its alteration affect all types of faults. K factor only exists in criteria for ground fault distance component, so its alteration affects single-phase-to-ground faults and three-phase faults.

Methods I adds the SFCL's impedance directly to the setting impedance Z_{set}.

$$Z'_{set} = Z_{set} + Z_{SFCL} \tag{7.3.2}$$

When a R-SFCL is introduced to the system, it is like it adds the corresponding impedance to transmission lines. Therefore Z_{set} and K should be changed accordingly. This leads to Methods II. In the system with SFCL, Z_0 represents the lines' zero sequence impedance plus the SFCL's zero sequence impedance. Z_1 represents lines' positive-sequence impedance plus the SFCLs positive-sequence impedance. For a symmetrical three phase SFCL, the zero sequence of SFCL is zero; the positive sequence impedance of SFCL is the impedance value of a single phase SFCL. Hence, the impedance value of SFCL should be added to Z_1 in Eq.7.3.2. It follows that adjusing K factor can compensate the protection distance to some extent for the two types of phase-to-ground fault, namely single-phase-to-ground faults and double-phase-to-ground faults.

$$K' = \frac{Z_0 - (Z_1 + Z_{SFCL})}{Z_1 + Z_{SFCL}} \tag{7.3.3}$$

However, these methods cannot fully adjust the protection distance to the theoretical value 85 km. This is because, from the protective relaying view, the SFCL's impedance characteristics do not match with the lines of the system; so the integration of SFCL destroys the fundamentals of the the power system.

As a result, pure theoretical analysis cannot be used to solve the problem of the decreasing protection distance of IPFR with the installation of SFCL. In order to improve the operation of IPFR and adjust the protection distance to an acceptable value, we can only use tremendous simulation testing to find such a method- Method III. One working method is to add the impedance of SFCL, multiplying a compensation factor $\sigma = 0.85$; and concurrently revising the K factor as in method II. By changing both setting impedance and K factor, the results

can be very desirable: the protection distance of IPFR reach nearly 85 km for all four types of short-circuit faults.

7.4 Conclusion

This chapter examined the influences of resistive SFCLs on the operation of Incremental Power Frequency Relays in transmission lines. The main research findings are as follows:

(1) Installation of resistive SFCLs can limit the short-circuited fault current effectively. The larger the impedance of SFCL is, the less the fault current is. This is the main feature of SFCL;

(2) Theoretical analysis shows that installation of resistive SFCL causes IPFR to operate incorrectly. This include misfunction of IPFR for an inner fault and the malfunction of IPFR for an external fault;

(3) Simulation results show that for four types of short-circuit faults, either symmetric or asymmetric, SFCL affects the protection distance negatively. The effective protection distance of IPFR decreases with the increase of SFCL resistance. This effect is particularly serious for double-phase faults and three-phase faults;

(4) Desirable compensation to eliminate the negative effect of the integration of SFCL can be achieved by adjusting both K factor and setting impedance of IPFR.

Chapter 8

Conclusions and future work

In this thesis, the first three chapters reviewed fundamentals of superconductivity and superconducting fault current limiters. The following four chapters described the main work and contributions of the author in the field of Superconducting Fault Current Limiters. This research included microscopic aspects of SFCLs such as the specific 2G HTS tapes for SFCL and macroscopic aspects such as the influence of SFCLs on AC grids, DC grids, and protective relays. It covered most of research areas on superconducting fault current limiters and laid a good foundation for better future research.

Chapter 4 conducted research on HTS YBCO tapes for SFCLs. Commercially available HTS tapes were different in their hierarchical structures and thus also different in their key parameters: critical current, room temperature resistance and mass. These parameters then determined the characteristics of tapes such as their capabilities to carry current, to limit fault current and to resist large impulsed current. The selection of YBCO tapes for specific engineering applications greatly relied on the above three parameters but the experimental research in this chapter proved that it was more sensible to use resistivity curve of different tapes rather than the three parameters when choosing tapes.

Future research will include simulation of superconducting materials with different hierarchical structures and comparisons between experiments and simulation results. This can be done by using Thermal-Electrical Analog Methods which were described in Chapter 5. We hope to develop a systematic methodology of research on tapes and to be able to fast determine the optimized hierarchical structure of tapes for application purposes.

Chapter 5 researched SFCL integrated with an existing AC distribution network in Germany. Most researches on SFCL were about the SFCL with the AC grid, and the most significant parts of these researches were the modeling of SFCL devices. Disappointingly, although various models were developed in literature to study SFCL, they did not consider heat exchanges between the layers and cooling equipment. The SFCL model used in this

work was one of the most sophisticated models which reflected temperature rise, quenching time, and evolution of the equivalent resistance during the whole period. The modelling involved the use of many physical properties such as specific heat, thermal conductivity and convection heat transfer coefficient. It should be noted that these parameters were also dependent on temperature, but the SFCL model used here did not take this into consideration. Therefore, further improvement of the SFCL model will be an essential part of future work. Additionally, the model was developed on MATLAB SIMULINK, and Thermal-Electrical Analog Methods were used to simplify the differential equations. Traditional software for power system simulation included PSCAD and EMTP, it will be extremely meaningful to adapt this model to other software to better study SFCL in power systems.

In Chapter 6, R-SFCLs were analyzed as a solution to the problem of commutation failure in direct current (DC) systems. R-SFCL performance was studied using PSCAD simulation, with different fault resistance values and fault initiation times for four types of faults in the DC system. The analysis results can be further improved and expanded if the SFCL model is improved in sophistication. Furthermore, it will be worthwhile testing the simulation results in Real Time Digital Simulator.

In Chapter 7, influences of R-SFCLs on transmission line incremental power frequency relays (IPFR) were examined, and corresponding compensation methods proposed. However, the compensation methods were based on numerous simulation tests rather than numerical analysis. This was because the introduction of SFCL to power systems was not merely adding a variable resistor. It changed the topology of the whole grid and most traditionally quantitative methods were no longer effective. The author recently proposed an analysis method which regarded the introduction of an SFCL as an event of complex faults. Further simulation results to justify the theoretical calculations are needed and this will be done soon. Proposed future work also concerns influences of R-SFCLs on other types of protective relays, and comparisons of inductive type SFCLs' influence on IPFRs.

References

[1] H. Kamerlingh-Onnes. *Comm. Leiden, Suppl.* 1913.

[2] "http://en.wikipedia.org/wiki/superconductivity.".

[3] Y. Iwasa. *Cryogenics*. 2003.

[4] W. Buckel and R. Kleiner. *Superconductivity: Fundamentals and applications*. 2004.

[5] H. A. Farach C. P. Poole and R. J. Creswick. *Superconductivity*. 2007.

[6] H. A. Farach C. P. Poole and R. J. Creswick. Superconductivity. *J. Phys. Chem. Solids*, page 346, 2007.

[7] K. Fossheim and A. Sudbo. *Superconductivity: physics and applications*. Johm Wiley Sons, 2015.

[8] R. Dynes J. Valles Jr H. Hess, R. Robinson and J. Waszczak. Scanning-tunneling-microscope observation of the abrikosov flux lattice and the density of states near and inside a fluxoid. *Physical review letters*, 62(2):214, 1989.

[9] S. Foltynet al. Materials science challenges for high-temperature superconducting wire. *Nature materials*, 6(9):631–642, 2007.

[10] Werner Buckel Reinhold Kleiner. *Superconductivity: An Introduction*. John Wiley and Sons, 2015.

[11] I Falorio, EA Young, and Y Yang. Ej characteristic of 2g ybco coated conductor tapes at different temperatures. *Physics Procedia*, 36:1462–1467, 2012.

[12] W. T. B. de Sousa. *Transient Simulations of Superconducting Fault Current Limiters*. PhD thesis, COPPE/UFRJ, March 2015.

[13] Vyacheslav F Solovyov and Qiang Li. Application of active quenching of second generation wire for current limiting. *Physica C: Superconductivity and its applications*, 519:130–136, 2015.

[14] Ying Xin, Weizhi Gong, Xiaoye Niu, Zhengjian Cao, Jingyin Zhang, Bo Tian, Haixia Xi, Yang Wang, Hui Hong, Yong Zhang, et al. Development of saturated iron core hts fault current limiters. *IEEE Transactions on Applied Superconductivity*, 17(2):1760–1763, 2007.

[15] Mathias Noe and Michael Steurer. High-temperature superconductor fault current limiters: concepts, applications, and development status. *Superconductor science and technology*, 20(3):R15, 2007.

[16] A.C.Rose-Innes and E.H.Rhoderick. *Introduction to superconductivity*. Pergamon International Library of Science, Technology, Engineering and Social Studies, 1976.

[17] J. G. Bednorz and K. A. Müller. "possible high tc superconductivity in the balacuo system,". *Zeitschrift für Physik B Condensed Matter*, 64(189):104007, 1986.

[18] https://journals.aps.org/prl/abstract/10.1103/physrevlett.58.908.

[19] http://iopscience.iop.org/article/10.1143/jjap.27.l209/meta.

[20] L. D. Landau and D. t. Haar. *Collected papers of L. D. Landau*. Oxford: Pergamon, 1965.

[21] L. N. Cooper J. Bardeen and J. R. Schrieffer. Theory of superconductivity. *Phys. Rev*, 106(1):162, 1957.

[22] A. A. Abrikosov. The magnetic properties of superconducting alloys. *J. Phys. Chem. Solids*, 2(3):199, 1975.

[23] J. Rice P. Gammel, D. Bishop and D. Ginsberg. Images of the vortex chain state in untwined yba2cu3o7-δ crystals. *Physical review letters*, 68(22):3342, 1992.

[24] et al B. M. Vlcek. Flux pinning in yba2cu3o7δ single crystals: Neutron irradiation and annealing. *Physical review letters*, 46(10):6441, 1992.

[25] E. M. Chudnovsky. Pinning by oxygen vacancies in high-tc superconductors. *Physical review letters*, 65(24):3060, 1990.

[26] E. M. Chudnovsky. Boson localization and pinning by correlated disorder in high-temperature superconductors. *Physical review letters*, 68(15):2398, 1992.

[27] C. P. Bean. Magnetization of high-field superconductors. *Physical review letters*, 36(31), 1964.

[28] C. F. Hempstead Y. B. Kim and A. R. Strnad. Critical persistent currents in hard superconductors. *Physical review letters*, 9(306), 1962.

[29] C. F. Hempstead Y. B. Kim and A. R. Strnad. Magnetization and critical supercurrents. *Physical review letters*, 129(528), 1963.

[30] P. W. Anderson and Y. B. Kim. Hard superconductivity: Theory of the motion of abrikosov flux lines. *Physical review letters*, 9(309), 1962.

[31] P. W. Anderson. Theory of flux creep in hard superconductors. *Physical review letters*, 9(309), 1962.

[32] R. Labusch M. R. Beasley and W. W. Webb. Flux creep in type-ii superconductors. *Physical review letters*, 181(682), 1969.

[33] A. P. Malozemoff. Flux creep in high temperature superconductors. *hysica C: Superconductivity*, 185-189(264), 1991.

[34] M. Uesaka Y. Yoshida and K. Miya. Magnetic field and force analysis of high tc superconductor with flux flow and creep. *IEEE Trans. Magn*, 30(3503), 1994.

[35] K. Fischer D. Busch R. Eujen A. Gladun, G. Fuchs and J. Huedepohl. Critical current densities and activation energy of bipbsrcacuo tapes. *IEEE Trans. Appl. Supercond*, 3(1390), 1993.

[36] LI Li, AM Li, KC Wu, et al. Analysis of short-circuit current exceeding standard of guangdong power grid and research on limitation measures. *Southern Power System Technology*, 3(S1):20–24, 2009.

[37] W. Bo. *Applied Study on the Magnetic Flux Constraint Fault Current Limiter*. PhD thesis, Huazhong University of Science and Technology, January 2012.

[38] Achim Hobl, S Elschner, J Bock, S Kramer, C Janke, and Judith Schramm. Superconducting fault current limiters: a new tool for the "grid of the future". 2012.

[39] Hun-Chul Seo, Chul-Hwan Kim, Sang-Bong Rhee, Jae-Chul Kim, and Ok-Bae Hyun. Superconducting fault current limiter application for reduction of the transformer inrush current: a decision scheme of the optimal insertion resistance. *IEEE Transactions on Applied Superconductivity*, 20(4):2255–2264, 2010.

[40] Mariam E Elshiekh, Diaa-Eldin A Mansour, and Ahmed M Azmy. Improving fault ride-through capability of dfig-based wind turbine using superconducting fault current limiter. *IEEE Transactions on Applied Superconductivity*, 23(3):5601204–5601204, 2013.

[41] Caihong Zhao, Zikai Wang, Dong Zhang, Jingye Zhang, Xiaoji Du, Wengyong Guo, Liye Xiao, and Liangzhen Lin. Development and test of a superconducting fault current limiter-magnetic energy storage (sfcl-mes) system. *IEEE Transactions on Applied Superconductivity*, 17(2):2014–2017, 2007.

[42] Naderi Seyed Behzad and Michael Negnevitsky. Soft and fast starting induction motors using controllable resistive type fault current limiter. In *Power & Energy Society General Meeting, 2015 IEEE*, pages 1–5. IEEE, 2015.

[43] H Shimizu, Y Yokomizu, T Matsumura, and N Murayama. Proposal of flux flow resistance type fault current limiter using bi2223 high t/sub c/superconducting bulk. *IEEE transactions on applied superconductivity*, 12(1):876–879, 2002.

[44] Z Zhong, Harold Steven Ruiz, L Lai, Z Huang, W Wang, and T Coombs. Experimental study of the normal zone propagation velocity in double-layer 2g-hts wires by thermal and electrical methods. *IEEE Transactions on Applied Superconductivity*, 25(3):1–5, 2015.

[45] Carlos A Baldan, Carlos Y Shigue, Jerika S Lamas, and Ernesto Ruppert Filho. Test results of a superconducting fault current limiter using ybco coated conductor. *IEEE Transactions on Applied Superconductivity*, 17(2):1903–1906, 2007.

[46] Xiuchang Zhang, J Geng, Boyang Shen, C Li, JDD Gawith, Z Zhong, J Ma, H Zhang, Q Dong, and Timothy Arthur Coombs. Active quenching technique for ybco tapes: Quench acceleration and protection. *Journal of Superconductivity and Novel Magnetism*, pages 1–10, 2018.

[47] T Hara, T Okuma, T Yamamoto, D Ito, K Tasaki, and K Tsurunaga. Development of a new 6.6 kv/1500 a class superconducting fault current limiter for electric power systems. *IEEE transactions on Power Delivery*, 8(1):182–192, 1993.

[48] Xiaoze Pei, Alexander C Smith, Mark Husband, and Matthew Rindfleisch. Experimental tests on a superconducting fault current limiter using three-strand wire. *IEEE Transactions on Applied Superconductivity*, 22(3):5600405–5600405, 2012.

[49] Joseph Duron, Bertrand Dutoit, Francesco Grilli, Michel Decroux, Louis Antognazza, and O Fischer. Computer modeling of ybco fault current limiter strips lines in overcritical regime with temperature dependent parameters. *IEEE Transactions on Applied Superconductivity*, 17(2):1839–1842, 2007.

[50] Mathias Noe, Achim Hobl, Pascal Tixador, Luciano Martini, and Bertrand Dutoit. Conceptual design of a 24 kv, 1 ka resistive superconducting fault current limiter. *IEEE Transactions on Applied Superconductivity*, 22(3):5600304–5600304, 2012.

[51] Fei Liang, Weijia Yuan, Jiahui Zhu, Min Zhang, Sriharsha Venuturumilli, Jianwei Li, Jay Patel, Guoming Zhang, and Zhenyu Zhang. Experimental test of two types of non-inductive solenoidal coils for superconducting fault current limiters use. *IEEE Transactions on Applied Superconductivity*, 27(4):1–5, 2017.

[52] B Gromoll, G Ries, W Schmidt, H-P Kraemer, B Seebacher, B Utz, R Nies, H-W Neumueller, E Baltzer, S Fischer, et al. Resistive fault current limiters with ybco films 100 kva functional model. *IEEE transactions on applied superconductivity*, 9(2):656–659, 1999.

[53] Alexander Usoskin, Herbert C Freyhardt, Alexander Issaev, Juergen Knoke, Juergen Dzick, Michel Collet, Peter Kirchesch, and Jorma Lehtonen. Superpoli fault-current limiters based on ybco-coated stainless steel tapes. *IEEE transactions on applied superconductivity*, 13(2):1972–1975, 2003.

[54] Claus Neumann. Superconducting fault current limiter (sfcl) in the medium and high voltage grid. In *Power Engineering Society General Meeting, 2006. IEEE*, pages 6–pp. IEEE, 2006.

[55] Kenji Shimohata, Syoichi Yokoyama, Itsuo Kodera, and Kenji Yasuda. Development of ka class fault current limiting unit with ybco thin films. *IEEJ Transactions on Power and Energy*, 125:1007–1014, 2005.

[56] Xing Yuan, Kasegn Tekletsadik, Leonard Kovalsky, Joachim Bock, Frank Breuer, and Steffen Elschner. Proof-of-concept prototype test results of a superconducting fault current limiter for transmission-level applications. *IEEE Transactions on Applied superconductivity*, 15(2):1982–1985, 2005.

[57] Luciano Martini, Marco Bocchi, Mario Levati, and Valerio Rossi. Simulations and electrical testing of superconducting fault current limiter prototypes. *IEEE transactions on applied superconductivity*, 15(2):2067–2070, 2005.

[58] Robert Dommerque, S Krämer, A Hobl, R Böhm, M Bludau, J Bock, D Klaus, H Piereder, A Wilson, T Krüger, et al. First commercial medium voltage superconducting fault-current limiters: production, test and installation. *Superconductor Science and Technology*, 23(3):034020, 2010.

[59] T Yazawa, K Koyanagi, M Takahashi, K Toba, H Takigami, M Urata, Y Iijima, T Saitoh, N Amemiya, Y Shiohara, et al. Development of 6.6 kv/600 a superconducting fault current limiter using coated conductors. *Physica C: Superconductivity*, 469(15-20):1740–1744, 2009.

[60] Heinz-Werner Neumueller, Wolfgang Schmidt, Hans-Peter Kraemer, Alex Otto, Jim Maguire, Jie Yuan, Doug Folts, Walter Romanosky, Bruce Gamble, David Madura, et al. Development of resistive fault current limiters based on ybco coated conductors. *IEEE Transactions on Applied Superconductivity*, 19(3):1950–1955, 2009.

[61] David Klaus, Chris Waller, Darren Jones, Jamie McWilliam, Jonathan Berry, Joachim Bock, Joseph Helm, Mostafa Jafarnia, and Achim Hobl. Superconducting fault current limiters-uk network trials live and limiting. 2013.

[62] Hye-Rim Kim, Seong-Eun Yang, Seung-Duck Yu, Heesun Kim, Woo-Seok Kim, Kijun Park, Ok-Bae Hyun, Byeong-Mo Yang, Jungwook Sim, and Young-Geun Kim. Installation and testing of sfcls. *IEEE Transactions on Applied Superconductivity*, 22(3):5602704–5602704, 2012.

[63] Z Hong, J Sheng, J Zhang, B Lin, L Ying, Y Li, and Z Jin. The development and performance test of a 10 kv resistive type superconducting fault current limiter. *IEEE Transactions on Applied Superconductivity*, 22(3):5600504–5600504, 2012.

[64] S Elschner, A Kudymow, J Brand, S Fink, W Goldacker, F Grilli, M Noe, M Vojenciak, A Hobl, M Bludau, et al. Ensystrob–design, manufacturing and test of a 3-phase resistive fault current limiter based on coated conductors for medium voltage application. *Physica C: Superconductivity and its applications*, 482:98–104, 2012.

[65] A Hobl, Wilfried Goldacker, B Dutoit, L Martini, A Petermann, and Pascal Tixador. Design and production of the eccoflow resistive fault current limiter. *IEEE transactions on applied superconductivity*, 23(3):5601804–5601804, 2013.

[66] BP Raju, KC Parton, and TC Bartram. A current limiting device using superconducting dc bias applications and prospects. *IEEE Transactions on Power Apparatus and Systems*, (9):3173–3177, 1982.

[67] Alexander Abramovitz, Keyue Ma Smedley, Francisco De La Rosa, and Franco Moriconi. Prototyping and testing of a 15 kv/1.2 ka saturable core hts fault current limiter. *IEEE Transactions on Power Delivery*, 28(3):1271–1279, 2013.

[68] Y Xin, WZ Gong, YW Sun, JB Cui, H Hong, XY Niu, HZ Wang, LZ Wang, Q Li, JY Zhang, et al. Factory and field tests of a 220 kv/300 mva statured iron-core superconducting fault current limiter. *IEEE Trans. Appl. Supercond.*, 23(3):5602305, 2013.

[69] Chen Liang, Chao Li, Pingxiang Zhang, Meng Song, Tao Ma, Tao Zhou, and Zhengfu Ge. Winding technology and experimental study on 500 kv superconductive fault current limiter. *IEEE Transactions on Applied Superconductivity*, 28(3):1–5, 2018.

[70] H Dersch. Inductive current limitation device for an alternating current using the superconductivity superconductor. *European Patent Specification*, 353449, 1990.

[71] W Paul, M Lakner, J Rhyner, P Unternährer, Th Baumann, M Chen, L Widenhorn, and A Guerig. Test of 1.2 mva high-superconducting fault current limiter. *Superconductor Science and Technology*, 10(12):914, 1997.

[72] H Kado and M Ickikawa. Performance of a high-tc superconducting fault current limiter-design of a 6.6 kv magnetic shielding type superconducting fault current limiter. *IEEE transactions on applied superconductivity*, 7(2):993–996, 1997.

[73] HJ Boenig and DA Paice. Fault-current limiter using a superconductingcijil. 1983.

[74] D Hui, ZK Wang, JY Zhang, D Zhang, ST Dai, CH Zhao, ZQ Zhu, HD Li, ZF Zhang, Y Guan, et al. Development and test of 10.5 kv/1.5 ka hts fault current limiter. *IEEE Transactions on Applied Superconductivity*, 16(2):687–690, 2006.

[75] Takashi Yazawa, Eriko Yoneda, Jun Matsuzaki, Mamoru Shimada, Toru Kuriyama, Shunji Nomura, Takeshi Ohkuma, Yoshibumi Sato, and Yoshihisa Takahashi. Design and test results of 6.6 kv high-tc superconducting fault current limiter. *IEEE transactions on applied superconductivity*, 11(1):2511–2514, 2001.

[76] Hyoungku Kang, Min Cheol Ahn, Yong Ku Kim, Duck Kweon Bae, Yong Soo Yoon, Tae Kuk Ko, Jung Ho Kim, and Jinho Joo. Design, fabrication and testing of superconducting dc reactor for 1.2 kv/80 a inductive fault current limiter. *IEEE transactions on applied superconductivity*, 13(2):2008–2011, 2003.

[77] T Matsumura, T Uchii, and Y Yokomizu. Development of flux-lock-type fault current limiter with high-t/sub c/superconducting element. *IEEE Transactions on Applied Superconductivity*, 7(2):1001–1004, 1997.

[78] Lei Chen, Yuejin Tang, Zhi Li, Li Ren, Jing Shi, and Shijie Cheng. Current limiting characteristics of a novel flux-coupling type superconducting fault current limiter. *IEEE Transactions on Applied Superconductivity*, 20(3):1143–1146, 2010.

[79] S Shimizu, H Kado, Y Uriu, and T Ishigohka. Single-line-to-ground fault test of a 3-phase superconducting fault current limiting reactor. *IEEE transactions on magnetics*, 28(1):442–445, 1992.

[80] M Steurer, H Brechna, and K Frohlich. A nitrogen gas cooled, hybrid, high temperature superconducting fault current limiter. *IEEE Transactions on Applied Superconductivity*, 10(1):840–844, 2000.

[81] Ziad Melhem. *High Temperature superconductors for energy applications*. Woodhead Publishing Limited, 2012.

[82] A Wolsky. Hts from precommercial to commercial: A roadmap to future use of hts by the power sector. *Int. Energy Agency*, 2013.

[83] Intae Hwang, Seung Ryul Lee, Sangsoo Seo, Jaeyoung Yoon, and Chul-Hwan Kim. Improvement of the Transient Stability Using SFCL in Korean Power Systems. *Phys. C Supercond.*, 494:335–338, 2013.

[84] Jing Shi, Lihui Zhang, Xiao Zhou, Yuanyuan Li, Rongyu Su, Li Ren, Jingdong Li, and Yuejin Tang. Application of a Voltage Compensation Type Active Superconducting Current Controller to Current Limiting Capability of Power Grid. *International Journal of Electrical Power & Energy Systems*, 101:385 – 393, 2018.

[85] T Yazawa, K Koyanagi, M Takahashi, K Toba, H Takigami, M Urata, Y Iijima, T Saitoh, N Amemiya, Y Shiohara, et al. Development of 6.6 kV/600A Superconducting Fault Current Limiter Using Coated Conductors. *Phys. C Supercond.*, 469(15):1740–1744, 2009.

[86] Xiuchang Zhang, H.S. Ruiz, Jianzhao Geng, and T.A. Coombs. Optimal Location and Minimum Number of Superconducting Fault Current Limiters for the Protection of Power Grids. *International Journal of Electrical Power & Energy Systems*, 87:136 – 143, 2017.

[87] Achim Hobl, S Elschner, J Bock, S Kramer, C Janke, and Judith Schramm. Superconducting Fault Current Limiters: A New Tool for the "Grid of the Future". In *CIRED Workshop*, page 0296, Lisbon, 2012. IET.

[88] Mathias Noe and Michael Steurer. High-Temperature Superconductor Fault Current Limiters: Concepts, Applications, and Development Status. *Supercond. Sci. Technol.*, 20(3):15–29, January 2007.

[89] Swarn S Kalsi and Alex Malozemoff. HTS Fault Current Limiter Concept. In *Power Engineering Society General Meeting*, pages 1426–1430. IEEE, 2004.

[90] Gaëtan Didier, Jean Leveque, and Abderrezak Rezzoug. A Novel Approach to Determine the Optimal Location of SFCL in Electric Power Grid to Improve Power System Stability. *IEEE Transactions on Power Systems*, 28(2):978–984, 2013.

[91] SR Khuntia and SR Samantaray. Analysis of resistive sfcl in a test-bed microgrid. *Ain Shams Engineering Journal*, 6(3):883–892, 2015.

[92] W. T. B. de Sousa, A. Polasek, F. A. Silva, R. Dias, A. R. Jurelo, and R. de Andrade. Simulations and Tests of MCP-BSCCO-2212 Superconducting Fault Current Limiters. *IEEE Transactions on Applied Superconductivity*, 22(2):5600106, April 2012.

[93] S. Elschner, F. Breuer, M. Noe, T. Rettelbach, H. Walter, and J. Bock. Manufacturing and testing of MCP 2212 Bifilar Coils for a 10 MVA Fault Current Limiter. *IEEE Transactions on Applied Superconductivity*, 13(2):1980–1983, June 2003.

[94] W Paul, M Chen, M Lakner, J Rhyner, D Braun, and W Lanz. Fault Current Limiter Based on High Temperature Superconductors - Different Concepts, Test Results, Simulations, Applications. *Physica C: Superconductivity*, 354(1-4):27–33, 2001.

[95] W. T. B. de Sousa, A. Polasek, R. Dias, C.F.T. Matt, and R. de Andrade Jr. Thermal–electrical Analogy for Simulations of Superconducting Fault Current Limiters. *Cryogenics*, 62:97 – 109, 2014.

[96] W. T. B. de Sousa, Tatiana Mariano Lessa Assis, Alexander Polasek, Andreia Maia Monteiro, and Rubens de Andrade. Simulation of a Superconducting Fault Current Limiter: A Case Study in the Brazilian Power System With Possible Recovery Under Load. *IEEE Transactions on Applied Superconductivity*, 26(2):1–8, 2016.

[97] H.J. Schettino, R. de Andrade Jr, A. Polasek, D. Kottonau, and W. T. B. de Sousa. A Strategy for Protection of High Voltage Systems Using Resistive Superconducting Fault Current Limiters. *Physica C: Superconductivity and its Applications*, 544:40 – 45, 2018.

[98] W. T. B. de Sousa, A Polasek, TML Assis, R de Andrade, and M Noe. Simulations of Resistive and Air Coil SFCLs in Power Grid. *IEEE Transactions on Applied Superconductivity*, 25(3):1–5, 2015.

[99] GRFQ Mafra, G. G. Sotelo, M. Z. Fortes, and W. T. B. de Sousa. Application of Resistive Superconducting Fault Current Limiters in Offshore Oil Production Platforms. *Electric Power Systems Research*, 144:107–114, 2017.

[100] DI Lawson and JH McGuire. The Solution of Transient Heat-Flow Problems by Analogous Electrical Networks. *Proceedings of the Institution of Mechanical Engineers*, 167(1):275–290, 1953.

[101] AF Robertson and Daniel Gross. An Electrical-Analog Method for Transient Heat-Flow Analysis. *Journal of Research of the National Bureau of Standards*, 61(2):105–115, 1958.

[102] Olaf Maeder. *Simulationen und Experimente zum Stabilitätsverhalten von HTSL-Bandleitern*, volume 6. KIT Scientific Publishing, 2014.

[103] Lin Ye, M Majoros, T Coombs, and AM Campbell. System Studies of the Superconducting Fault Current Limiter in Electrical Distribution Grids. *IEEE Trans. Appl. Supercond.*, 17(2):2339–2342, 2007.

[104] B. Li and Y. Z. Ou. Studies on the Influences of SFCL on the Transient Recovery Voltage of Circuit Breaker. In *2015 IEEE International Conference on Applied Superconductivity and Electromagnetic Devices (ASEMD)*, pages 541–542, Nov 2015.

[105] AKE CARLSSON THOMAS FREYHULT, MATS BERGLUND. Grid optimization uhvdc =.

[106] J. Zhu H. Xiao, Y. Li and X. Duan. Ecient approach to quantify commutation failure immunity levels in multi-infeed HVDC systems. *IET Generation, Transmission Distribution*, 10(4):1032–1038, 2016.

[107] C. Zhao X. Ni K. Zha C. Guo, C. Li and W. Xu. An evolutional line-commutated converter integrated with thyristor-based full-bridge module to mitigate the commutation failure. *IEEE Transactions on Power Electronics*, 32(2):967–976, Feb 2017.

[108] J. B. Davies I. T. Fernando E. Rahimi, A. M. Gole and K. L. Kent. Commutation failure analysis in multi-infeed HVDC systems. *IEEE Transactions on Power Delivery*, 26(1):378–384, Jan 2011.

[109] C. Guo H. Liu X. Ni, C. Zhao and Y. Liu. Enhanced line commutated converter with embedded fully controlled sub-modules to mitigate commutation failures in high voltage direct current systems. *IET Power Electronics*, 9(2):198–206, 2016.

[110] D. Tzelepis D. M. Said A. Dysko S. Mirsaeidi, X. Dong and C. Booth. A predictive control strategy for mitigation of commutation failure in LCC-based HVDC systems. *IEEE Transactions on Power Electronics*, page 1–1, 2018.

[111] L. Zhang and L. Dofnas. A novel method to mitigate commutation failures in HVDC systems. *Proceedings. International Conference on Power System Technology*, 1:51–56, Oct 2002.

[112] R. Bunch and D. Kosterev. Design and implementation of AC voltage dependent current order limiter at pacic HVDC intertie. *IEEE Transactions on Power Delivery*, 15(1):293–299, Jan 2000.

[113] C. W. Taylor and S. Lefebvre. HVDC controls for system dynamic performance," IEEE Transactions on Power Systems. *IEEE Transactions on Power Delivery*, 6(2):743–752, May 1991.

[114] F. Karlecik-Maier. A new closed loop control method for HVDC transmission," IEEE Transactions on Power Delivery. *IEEE Transactions on Power Delivery*, 11(4):1955–1960, Oct 1996.

[115] M. Jafar and M. Molinas. Eects and mitigation of post-fault commutation failures in line-commutated HVDC transmission system. *2009 IEEE International Symposium on Industrial Electronics*, page 81–85, July 2009.

[116] Y. Zhang M. O. Faruque and V. Dinavahi. Detailed modeling of CIGRE HVDC benchmark system using PSCAD/EMTDC and PSB/SIMULINK. *IEEE Transactions on Power Delivery*, 21(1):378–387, Jan 2006.

[117] J. B. Davies C. V. Thio and K. L. Kent. Commutation failures in HVDC transmission systems. *IEEE Transactions on Power Delivery*, 11(2):946–957, Apr 1996.

[118] F. Ishiguro M. Sato K. Yamaji S. Tamai, H. Naitoh and N. Honjo. Fast and predictive HVDC extinction angle control. *IEEE Transactions on Power Systems*, 12(3):1268–1275, Aug 1997.

[119] X. P. Zhang Y. Xue and C. Yang. Elimination of commutation failures of LCC HVDC system with controllable capacitors. *IEEE Transactions on Power Systems*, 31(4):3289–3299, July 2016.

[120] T. Jonsson D. Menzies S. Gomes, N. Martins and R. Ljungqvist. Modeling capacitor comnmutated converters in power system stability studies. *IEEE Power Engineering Review*, 22(4):76–76, April 2002.

[121] D. P. Brandt A. M. Gole K. Sadek, M. Pereira and A. Daneshpooy. Capacitor commutated converter circuit congurations for DC transmission. *IEEE Power Engineering Review*, 13(4):1257–1264, Oct 1998.

[122] C. Wenjia L. Sizhuo Z. Siyu, W. Jun and Y. Wei-yang. Study on transient characteristics of CCC-HVDC transmission systems. *International Conference on Sustainable Power Generation and Supply (SUPERGEN 2012)*, pages 1–5, Sept 2012.

[123] J. I. Yoo H. J. Lee, G. T. Son and J. W. Park. Eect of a SFCL on commutation failure in a HVDC system. *IEEE Transactions on Applied Superconductivity*, 23(3):5600104–5600104, June 2013.

[124] C. Deng F. Zheng Z. Li L. Chen, H. Pan and F. Guo. Study on the application of a ux-coupling-type superconducting fault current limiter for decreasing HVDC commutation failure. *Canadian Journal of Electrical and Computer Engineering*, 38(1):10–19, winter 2015.

[125] Thomas J. Domin J. Lewis Blackburn. *Protective Relaying Principles and Applications Third Edition*. CRC press, 2006.

[126] Foroud A.A. Barzegar-Bafrooei, M.R. Investigation of the performance of distance relay in the presence of saturated iron core SFCL and diode bridge type SFCL. *International Transactions on Electrical Energy Systems*, 2018.

[127] Gharehpetian G.B. Mozafari B. Firouzi, M. Bridge-type superconducting fault current limiter effect on distance relay characteristics. *International Journal of Electrical Power and Energy Systems*, 68:115–122, 2015.

[128] The impact of SFCL and SMES integration on the distance relay" *Physica C: Superconductivity and its Applications*, author= Yang, J., Zhang, L., Wang, X., Chen, L., Chen, Y., journal= International Journal of Electrical Power and Energy Systems, year= 2016, volume=530, pages= 151-159,.

[129] Heresh S. Shahram P.D. Saeed, A. Optimal coordination of overcurrent protection in the presence of SFCL and distributed generation. *Turkish Journal of Electrical Engineering and Computer Sciences*, 26(4):2056–2065, 2018.

[130] J. S. Kim, S. H. Lim, and J. C. Kim. Study on Protection Coordination of a Flux-Lock Type SFCL With Over-Current Relay. *IEEE Transactions on Applied Superconductivity*, 20:1159–1163, June 2010.

[131] F. Guo B. Li, C. Li and Y. Xin. Overcurrent Protection Coordination in a Power Distribution Network With the Active Superconductive Fault Current Limiter. *IEEE Transactions on Applied Superconductivity*, 24, 2014.

[132] F. Guo Y. Xin C. Wang B. Li, C. Li and X. Pang. Coordination of Superconductive Fault Current Limiters With Zero-Sequence Current Protection of Transmission Lines. *IEEE Transactions on Applied Superconductivity*, 24, 2014.